Lawrence Berkeley National Laboratory
LBL Publications

Title

DECOVALEX-2023 Task B Final Report

Permalink

https://escholarship.org/uc/item/8166c45g

Authors

Faybishenko, Boris

Tamayo-Mas, E

Harrington, JF

Publication Date

2024-11-29

Copyright Information

DECOVALEX-2023
Task B Final Report

E. Tamayo-Mas and J.F. Harrington

With contributions from:

E. Radeisen, J.T. Kim, J. Rutqvist, I.P. Damians, Y. Wang, R.J. Cuss

July 2023

Disclaimer

Copyright

DECOVALEX-2023

Task B Final Report

Main Authors :

E. Tamayo-Mas and J.F. Harrington
British Geological Survey, Keyworth, Nottingham, United Kingdom

Contributing Authors (alphabetical by organisation) :

E. Radeisen
Federal Institute for Geosciences and Natural Resources, Hanover, Germany

J.T. Kim.
Korea Atomic Energy Research Institute, Daejeon, Korea

J. Rutqvist
Lawrence Berkeley National Laboratory, Berkeley, California, U.S.A.

Y. Wang
Sandia National Laboratories, Albuquerque, New Mexico, U.S.A.

I.P. Damians
Universitat Politècnica de Catalunya, Barcelona, Spain

R.J. Cuss
British Geological Survey, Keyworth, Nottingham, United Kingdom

Preface

The DECOVALEX Project is an ongoing international research collaboration established in 1992 to advance the understanding and modeling of coupled Thermal (T), Hydrological (H), Mechanical (M), and Chemical (C) processes in geological systems. DECOVALEX was initially motivated by recognising that predicting these coupled effects is essential to the performance and safety assessment of geologic disposal systems for radioactive waste and spent nuclear fuel. Later, it was realized that these processes also play a critical role in other subsurface engineering activities, such as subsurface CO_2 storage, enhanced geothermal systems, and unconventional oil and gas production through hydraulic fracturing. Research teams from many countries (e.g., Canada, China, Czech Republic, Finland, France, Germany, Japan, Netherlands, Republic of Korea, Spain, Sweden, Switzerland, Taiwan, United Kingdom, and the United States) various institutions have participated in the DECOVALEX Project over the years, providing a wide range of perspectives and solutions to these complex problems. These institutions represent radioactive waste management organizations, national research institutes, regulatory agencies, universities, and industry and consulting groups.

At the core of the collaborative work within DECOVALEX is the collaborative analysis and comparative modeling of state-of-the-art field and laboratory experiments. DECOVALEX engages model comparison in a broad and comprehensive sense, including the modelers' interpretation of experimental data, selection of boundary conditions, rock and fluid properties, etc., and their choice of coupling schemes and simulators. This recent phase of DECOVALEX has expanded the work scope to include the modelers being challenged to gain an understanding of the representation coupled processes in generic 'whole system' or 'performance assessment' models. In-depth and detailed discussions among the teams yield insight into the coupled THMC processes and stimulate the development of modeling capabilities and measurement methods. This would have been impossible if only one or two groups had studied the data.

Since the project initiation, DECOVALEX has been organized in several four-year phases, each featuring several modeling tasks of importance to radioactive waste disposal and other geoscience applications. Seven project phases were successfully concluded between 1992 and 2019, the results of which have been summarized in several overview publications (e.g., Tsang et al., 2009; Birkholzer et al., 2018; Birkholzer et al., 2019, Birkholzer et al., 2024). The most recent phase, DECOVALEX-2023, started in 2020 and ended in 2023. Seven tasks were conducted in DECOVALEX-2023, as follows:

- **Task A: HGFrac** – Thermal- and gas- induced fracturing of the Callovo-Oxfordian Clay, France
- **Task B: MAGIC** – Migration of gas in compacted clay
- **Task C: FE Experiment** – Thermal-hydro-mechanical (THM) modelling of the FE experiment at Mont Terri, Switzerland
- **Task D: Horonobe EBS Experiment** - THM modelling of the Horonobe EBS experiment at the Horonobe URL, Japan
- **Task E: BATS** – THM modeling for the Brine Availability Test in Salt (BATS) at the WIPP, New Mexico, USA

- **Task F: Performance Assessment** – Comparative generic performance assessment models in crystalline and salt formations
- **Task G: SAFENET** – Laboratory-scale TH and THM analyses of single fractures

The DECOVALEX Project would not have been possible without the support and engagement of the participating organizations who jointly support the coordination of the project within a given project phase, propose and coordinate modeling tasks, including the necessary experimental data, and deploy their research team (or teams) working on a selection of the tasks conducted in the project. The partner organizations in DECOVALEX-2023 were:

- Andra, National Radioactive Waste Management Agency, *France*
- BASE, Federal Office for the Safety of Nuclear Waste Management*, Germany*
- BGE, Federal Company for Radioactive Waste Disposal, *Germany*
- BGR, Federal Institute for Geosciences and Natural Resources, *Germany*
- CAS, Chinese Academy of Sciences, *China*
- CNSC, Canadian Nuclear Safety Commission, *Canada*
- COVRA, Central Organisation for Radioactive Waste, *Netherlands*
- DOE, Department of Energy, *USA*
- Enresa, National Radioactive Waste Management Agency, *Spain*
- ENSI, Swiss Federal Nuclear Safety Inspectorate, *Switzerland*
- JAEA, Japan Atomic Energy Agency, *Japan*
- KAERI, Korea Atomic Energy Research Institute, Republic of Korea
- NWMO, Nuclear Waste Management Organization, *Canada*
- NWS, Nuclear Waste Services, *United Kingdom*
- SSM, Swedish Radiation Safety Authority, *Sweden*
- SÚRAO, Radioactive Waste Repository Authority, *Czech Republic*
- Taipower, Taiwan Power Company, *Taiwan*

We are extremely grateful to these organizations for their financial and technical support of DECOVALEX-2019.

Jens Birkholzer (Chairman of the DECOVALEX project) and Alex Bond (Technical Coordinator of the DECOVALEX Project).

Berkeley, California, USA, October 2024

References:
Birkholzer, J.T., Bond, A.E., Hudson, J.A., Jing, L., Tsang, C.-F., Shao, H., Kolditz, O. (2018): DECOVALEX-2015 - An International Collaboration for Advancing the Understanding and Modeling of Coupled Thermo-Hydro-Mechanical-Chemical (THMC) Processes in Geological Systems, Environmental Earth Sciences, 77(14). https://doi.org/10.1016/j.ijrmms.2022.105097

Birkholzer, J.T., Tsang, C.-F., Bond, A.E., Hudson, J.A., Jing, L., and Stephansson, O. (2019): 25 Years of DECOVALEX - Scientific Advances and Lessons Learned from an International Research Collaboration in Coupled Subsurface Processes, Invited Review, International Journal and Rock Mechanics and Mining Sciences, 122. https://doi.org/10.1016/j.ijrmms.2019.03.015

Birkholzer, J.T., Bond, A.E. and Tsang, C.-F. (2024). The DECOVALEX international collaboration on modeling of coupled subsurface processes and its contribution to confidence building in radioactive waste disposal. Hydrogeology Journal, https://doi.org/10.1007/s10040-024-02799-7

Tsang, C.-F., Stephansson, O., Jing, L., and Kautsky, F. (2009): DECOVALEX Project: from 1992 to 2007. Environmental Geology, 57(6). https://doi.org/10.1007/s00254-008-1625-1

Summary

In all repository concepts for the geological disposal of radioactive waste, an engineered barrier system (EBS) is used to encapsulate the waste canister, or, to act as borehole or gallery seals. These systems are often based on bentonite clays due to their low permeability and high swelling capacity enabling the closure of engineering voids. However, in all repository concepts gases will be generated through the corrosion of metallic materials (under anoxic conditions), the radioactive decay of waste and the radiolysis of water. Thus, understanding the processes and mechanisms controlling the advective movement of gas (as a discrete phase) in clay-based materials is a key aspect when assessing the impact of gas flow in a repository safety case.

Task objectives and scientific interest

In order to better understand the processes governing the advective movement of gas in both low-permeability argillaceous repository host rocks and clay-based engineered barriers, multiple researchers have recently developed new numerical algorithms within the framework of Biot's consolidation theory, where features such as damage, plasticity, embedded fractures, etc., have been considered to include or explicitly represent dilatant gas flow in clay-based materials. All these models are capable of capturing some of the main response features observed in laboratory studies, but they unable to effectively reproduce all of the main experimental observations that characterise dilatancy-controlled flow. Indeed, the improvement of parameter calibration procedures, the further development of spatially- and temporally-dependent processes and the inclusion of pathways that behave in a highly dynamic and unstable manner, create uncertainties and thus, development of new and novel numerical representations for the quantitative treatment of gas in clay-based repository systems are still required. This was the primary focus of Task A in the DECOVALEX-2019 (D-2019) project, in which 8 international teams attempted to model advective gas flow in 1D and 3D experiments performed on compacted bentonite samples under controlled laboratory conditions. In Task A D-2019, four types of modelling approaches were developed: (i) two-phase flow models incorporating a range of different mechanical deformation behaviours, (ii) enhanced two-phase flow models in which fractures were embedded within a plastic material (continuous techniques) or incorporated into the model using a rigid-body-spring network (discrete approaches), (iii) a single-phase model incorporating a creep damage function in which only gas flow was considered, and (iv) a conceptual approach used to examine the chaotic nature of gas flow. The D-2019 models featured robust

hydro-mechanical couplings based on pre-defined physical quantities. However, some of the important underlying physics (e.g., creation of dilatant pathways) associated with advective gas flow were poorly described and therefore the models were unable to represent the full complexity of the processes in these low-permeability materials.

Several concerns were raised in Task A D-2019 (e.g., parameter calibration and model constraints, heterogeneity, stochasticity and upscaling) and with these concerns in mind, it was concluded that enhanced numerical representations for the quantitative treatment of gas in clay-based repository systems were still required. This was the primary focus of Task B in DECOVALEX-2023 (D-2023).

Experimental data

Task B was split into three stages each building on the previous, representing an incremental increase in complexity. In the first place, a conceptual model development phase (stage 1) was undertaken. This was followed by a stage 2, in which a blind prediction test was modelled. A new and hitherto unseen dataset was used to facilitate the blind prediction exercise (test FPR-21-004). In contrast to previous stages of DECOVALEX-2019, a gas-injection test carried out by the British Geological Survey (BGS) on a compacted bentonite sample with a 1:1 ratio was considered. As before, experiments were performed in a constant volume cell with material subject to rehydration and then gas flow. The task then moved to a third stage (a full-scale in situ test), where teams were required to model a large-scale gas injection test (Lasgit) conducted at the Äspö Hard Rock Laboratory.

Analysis approaches

Five different approaches have been adopted by the participating teams. A conceptual model that analyses the complexity of the gas migration process by means of nonlinear dynamics and deterministic chaos theory was developed by SNL. Its numerical development is, however, still in a very preliminary phase and it could not be used to reproduce the experiments. Four different numerical approaches were adopted by the other teams (BGR/UFZ, KAERI, LBNL and CIMNE-UPC/Andra). The numerical capabilities of three of these numerical approaches (BGR/UFZ, LBNL and CIMNE-UPC/Andra were assessed by comparing the simulated results against the experimental data obtained from the blind prediction exercise (stage 2) and then, after some modification, were employed to simulate the full-scale experiment (stage 3). Note that the model developed by KAERI was only used to simulate the Lasgit test (stage 3), since the team

joined the task late into the project (November 2021). All these numerical approaches are based on the general theory of multi-phase flow, using continuum models which are combined with additional properties to describe some of the key features observed in laboratory- and field-tests that distinguish clay-rich media from other rock-types (e.g., deformation of the porous media, creation of dilatant pathways, self sealing, etc.).

Key learning points

DECOVALEX-2023 Task B has yielded useful knowledge in the development and understanding of both the techniques and outcomes of gas migration experiments and their associated modelling. This study has shown that these numerical approaches can successfully represent some of the main deterministic experimental features typically observed in dilatancy-controlled gas flow (e.g., initial and peak stress values). However, there are other features that are not correctly captured (e.g., the rapid transition phase seen during breakthrough). This suggests that numerical models still lack a complete description of the full complexity of the physical processes observed in water-saturated experiments. While the models capture some of the key aspects of gas flow, the need for detailed calibration, limits their use in a predictive manner.

This study has identified three key learning points that need to be born in mind when numerically modelling gas flow through water saturated low permeable clay samples:

- **Model calibration**: models need calibration of fitted parameters. Each model needs a specific calibration process and thus, their adjustment requires detailed sensitivity analyses. Since gas flow presents stochastic features by its very nature, these analyses should distinguish between the key reproducible experimental features across all experiments and those that only occur in a limited (or specific) subset/experiment.

- **Heterogeneity**: preferential pathways are not explicitly represented and hence, fracture-specific properties such as the evolving fracture front, number and distribution of pathways, and pathway closure mechanisms are not included in the models. Instead, heterogeneous material distributions can be used to implicitly represent preferential pathways.

- **Model coarsity**: developed models are not fine enough to explicitly include representations of microscopic dilatancy or heterogeneous gas channelling. Although this might represent a limitation, the use of fine meshes is not recommended, as approaches that can potentially be tractable at engineered barrier and repository scales are ultimately needed.

Areas for future work

This phase of DECOVALEX provides a foundation for extension of the codes and models to natural systems which exhibit additional complexity, including diagenesis and material anisotropy. This study illustrates further experiments and analyses are required to improve process understanding and the hydromechanical coupling/constitutive laws with numerical models before they can be used, with confidence, as a predictive tool to assess advective gas movement in a repository setting. Further consideration of the following is required:

- **Parameter calibration and model constraints**: developed models need calibration of fitted parameters. This poses a computational challenge as a large number of simulations are required. In addition, their adjustment is a complex task: indeed, although it is possible to evaluate the main effect of a single parameter on the global response, several parameter correlations exist due to the complex model couplings. This is further complicated by uncertainties in experimental parameters, where distributed functions may be required. A great effort from the modelling teams has been made to tackle the former issue and detailed sensitivity analysis have been carried out to characterise the one-dimensional gas injection test. However, their extrapolation to other tests can be difficult. This was also observed in Task A in D-2019, where different parameter values for the 1D and the 3D tests were sometimes arbitrarily prescribed. Thus, more numerical analyses and a better understanding of the complex couplings within the codes are needed before the models could be used with confidence as a predictive tool to assess gas movement.
- **Heterogeneity**: the role of material heterogeneity needs to be further explored, as it has been shown that it might provide a possible way to represent flow localisation. Indeed, some teams have assumed heterogeneous fields (e.g., permeability, gas entry pressure), as the introduction of heterogeneity at the capillary scale is not practicable. However, the assumed distribution functions are usually arbitrary prescribed and lack a physical justification. In the absence of data (e.g., characterisation of pore morphology (before, during and after gas migration), variation in material properties, coupling between pathway creation/dilation/closure and their interaction with material properties), this issue remains a challenge for all teams.

Contents

1 Introduction

In a repository for radioactive waste hosted in a very low permeability formation, hydrogen and other gases may be generated due to the corrosion of metallic materials under anoxic conditions, the radioactive decay of waste and the radiolysis of water. If the host rock is a plastic clay or uses engineered clay boundary seals, there is the possibility that if the gas production rate exceeds the clay gas diffusion rate, a discrete gas phase will form behind the clay, and accumulate until its pressure becomes large enough to exceed the entry pressure of the surrounding material, at which point dilatant, advective flow of gas is expected to occur. There is now a substantial body of evidence, spanning multiple decades, indicating that in these materials, when initially fully saturated, gas migration occurs through the creation of dilatant pathways rather than by moving within the original porosity of the clay as conceptualised in Darcy's law (see for instance Horseman et al. 1996, Harrington and Horseman 2003, Harrington et al. 2012). These pathways interact with the surrounding clay mass to introduce a complex hydro-mechanical coupling (Harrington et al. 2017, 2019; Senger et al. 2018).

The understanding of the processes and mechanisms involved is therefore a key aspect when assessing the impact of gas flow on the design of any future facility.

To this end, multiple researchers have recently developed new numerical algorithms within the framework of Biot's consolidation theory, where features such as damage, plasticity, embedded fractures, etc., have been considered to include or explicitly represent dilatant gas flow in clay-based materials (Senger et al. 2018, Tamayo-Mas et al. 2021, Guo and Fall 2018, Radeisen et al. 2023, Chittenden et al. 2020, Yang and Fall 2021, Damians et al. 2020). All these models are capable of capturing some of the main response features observed in laboratory studies, but they do not appear to effectively reproduce all of the main experimental observations that characterise dilatancy-controlled flow. Indeed, although most of them can satisfactorily simulate specific experimental features such as breakthrough time, maximum pressure/stress measurements and the dilation of the sample, there remain difficulties when trying to match the whole experimental history. Features such as the evolution of stress during and after breakthrough or the temporal variations in gas outflow are not well reproduced, see Tamayo-Mas et al. (2021). Other features such as the improvement of parameter calibration procedures, the further development of spatially- and temporally-dependent processes and the inclusion of highly dynamic and unstable pathways still remain uncertainties. Thus, development of new and novel numerical representations

for the quantitative treatment of gas in clay-based repository systems are still required. This was the primary focus of Task A in the DECOVALEX-2019 (D-2019) project, see Tamayo-Mas et al. (2021), in which 8 teams attempted to model the movement of gas in plastic clays in 1D and 3D experiments performed under controlled laboratory conditions (Harrington et al. 2017 and Daniels and Harrington 2017). In Task A D-2019, four types of modelling approaches were developed: (i) two-phase flow models incorporating a range of different mechanical deformation behaviours, (ii) enhanced two-phase flow models in which fractures are embedded within a plastic material (continuous techniques) or incorporated into the model using a rigid-body-spring network (discrete approaches), (iii) a single-phase model incorporating a creep damage function in which only gas flow is considered, and (iv) a conceptual approach used to examine the chaotic nature of gas flow. In contrast to previous international gas projects such as EVEGAS (Manai, 1995, 1997a, 1997b) or GAMBIT (Nash et al. 1998, Swift et al. 2001, Hoch et al. 2004), where some model parameters were heuristically adjusted to overcome the poorly characterised couplings between the stress field and gas and water pressures, the D-2019 models featured more robust hydro-mechanical couplings based on pre-defined physical quantities. Nevertheless, some of the important underlying physics (e.g., creation of dilatant pathways) associated with advective gas flow were poorly understood, which means it is not possible to describe the full complexity of this process in these low-permeability materials and therefore unable to represent the full complexity of the processes in these low-permeability materials. However, it may be possible to simplify these processes depending on the requirements of the model and its application within safety assessment.

Several concerns were raised in Task A D-2019 as some key features in the modelling of advective gas were still unclear:

- **Parameter calibration and model constraints**: model complexity was significantly different among the proposed strategies and some models were clearly over-parameterised. Marked differences were also found in the calibration outcomes. Indeed, both the number of the calibrated parameters and the experimental outputs used to calibrate them were significantly different between teams. While, some of these parameters (e.g., tensile strength, swelling pressure etc.) had a clear physical meaning, and can generally be measured directly or indirectly, others (e.g., damage smoothing coefficients, capillary spacing etc.) were numerical constructs which had an indirect physical meaning and were often unmeasurable and used for fitting purposes within the model. Hence, their definition is complex and their extrapolation to other tests can be difficult. This was already observed in Task

A D-2019, where different parameter values for the 1D and the 3D tests were sometimes assumed. More analysis and a better understanding are needed before using the models as a predictive tool to assess gas movement.

- **Heterogeneity**: two models included explicit representations of material heterogeneity. This needs to be further explored and analysed since it might provide one possible route to represent localisation of flow in continuum models.

- **Stochasticity**: the experimental data from the 1D and the 3D gas injection tests exhibited a combination of stochastic and deterministic behaviours. Gas breakthrough occurred after a period of increasing gas pressure, when bulk gas flow was observed through the development of an emergent pathway. The instability and pathway switching observed in the 3D experiment before a main flow path was established, suggested that the precise timing of the gas breakthrough and associated gas flows could be stochastic by nature. It is therefore important in a deterministic analysis to distinguish between the key experimental features reproducible across all experiments and those that only appear to have a random or chaotic component. Therefore, being able to analyse and model similar high-quality experimental datasets is required to help give confidence in the process of understanding.

- **Upscaling**: although in Task A D-2019 only experiments under controlled laboratory conditions were modelled, models that are tractable at engineered barrier and repository scales are needed. This poses a major challenge, since accurately and efficiently including small scale features (which might have a significant impact on repository performance) in a field test is a complex process.

With these concerns in mind, development of updated numerical representations for the quantitative treatment of gas in clay-based repository systems are therefore required, and are the primary focus of Task B in DECOVALEX-2023 (D-2023).

This Task is split into three stages each building on the previous, representing an incremental increase in complexity:

1. **Stage 1 (code development)**: the task runs for four years and starts with a conceptual model development phase. The main objective of this first stage is to assess team's modelling capabilities (those already developed within Task A D-2019 or elsewhere). Participating teams should pay special attention on how their models describe:
   - The development of dilatant pathways.

- The permeability associated with this pathway development.
- The coupling between permeability and stress.

2. **Stage 2 (blind prediction test)**: stage 1 is then followed by a second stage, where a blind prediction test was modelled. The main objective of this second stage is to assess those models and to analyse their capabilities. Special emphasis is placed on the fact that the purpose of this test is not to calibrate the models via fitting routines but to analyse whether the key features of the experiments are well-captured or not.

3. **Stage 3 (Lasgit modelling)**: the task moves then to a third stage (a full-scale in situ test), where teams are required to model a large-scale gas injection test (Lasgit) experiment conducted at the Äspö Hard Rock Laboratory.

This report summarises the outcomes of stages 1, 2 and 3 conducted from May 2020 to May 2023 by the five participating modelling teams:

1. **BGR/UFZ (Germany)**: Federal Institute for Geosciences and Natural Resources and the Helmholtz Centre for Environmental Research.
2. **KAERI (Korea)**: Korea Atomic Energy Research Institute[1].
3. **LBNL (United States of America)**: Lawrence Berkeley National Laboratory.
4. **SNL (United States of America)**: Sandia National Laboratories.
5. **CIMNE-UPC/Andra (Spain/France)**: Universitat Politècnica de Catalunya (International Centre for Numerical Methods in Engineering), funded by l'Agence nationale pour la gestion des des déchets radioactifs (Andra).

It is not the intention of this report to provide an exhaustive description of the individual contributions from each team, but rather give a technical overview and synthesis of key conclusions and results. Further details can be found in the following synthesis publications:

- Tamayo-Mas E., Harrington J.F., Damians I.P., Olivella S., Radeisen E., Rutqvist J., Wang Y. DECOVALEX 2023: Comparative modelling of advective gas flow in Energy Geoscience Conference – EGC1 (Aberdeen 16th to 18th May 2023).

- Tamayo-Mas E., Harrington J.F., Damians I.P., Olivella S., Radeisen E., Rutqvist J., Wang Y. 2024. A comparative study of theoretical and numerical approaches for the description of advective gas flow in clay-based repository systems. Geomechanics for Energy and the Environment, 37, 100528

---

[1] KAERI joined D-2023 Task B in September 2021 and thus, they did not participate in the blind prediction exercise (Stage 2).

At the time of writing, peer-reviewed journal articles were in preparation from many of the teams; further details are given in Section 6.

2   Experimental data

2.1 Laboratory-scale gas injection test

As part of Task B, a new and hitherto unseen dataset was required to facilitate the blind prediction exercise. In previous stages of DECOVALEX-2019, teams had been given data at the outset with which to develop and calibrate their models. These experiments were based on data derived from tests performed on samples with a nominal length of 120 mm and nominal diameter of 60 mm. However, for the purposes of this blind prediction exercise (test FPR-21-004), the sample geometry was changed from a 2:1 ratio to a 1:1 ratio: indeed, in this instance, a sample of 60 mm in length and 60 mm in diameter was considered. As before, experiments were performed in a constant volume cell with material subject to rehydration first and then gas flow. In the following sections a detailed description of the apparatus, the test history undertaken and the results obtained, are presented.

2.1.1 Experimental set-up

In this test geometry, the specimen is volumetrically constrained, preventing dilation of the clay in any direction. This BGS custom-designed apparatus, Figure 1, has six main components: (1) a thick-walled, dual-closure Invar[2] pressure vessel; (2) an injection pressure system; (3) a backpressure system; (4) 24 total stress gauges to measure radial and axial total stresses; (5) two porewater pressure monitoring filters; and (6) a microcomputer-based data acquisition system based around a National Instruments Compact Rio set-up.

The pressure vessel comprised of a dual-closure tubular vessel manufactured from Invar and was pressure-tested at 70 MPa. Each end-closure was secured by eight high tensile cap screws which could be used to apply a small pre-stress to the specimen if required. The vessel was mounted vertically with injection of gas through a rod mounted in the lower end-closure, Figure 1, the dimensions of which are presented in Figure 2.

---

[2] Invar, also know as Alloy 36, is a nickel-iron alloy with a low thermal expansion coefficient.
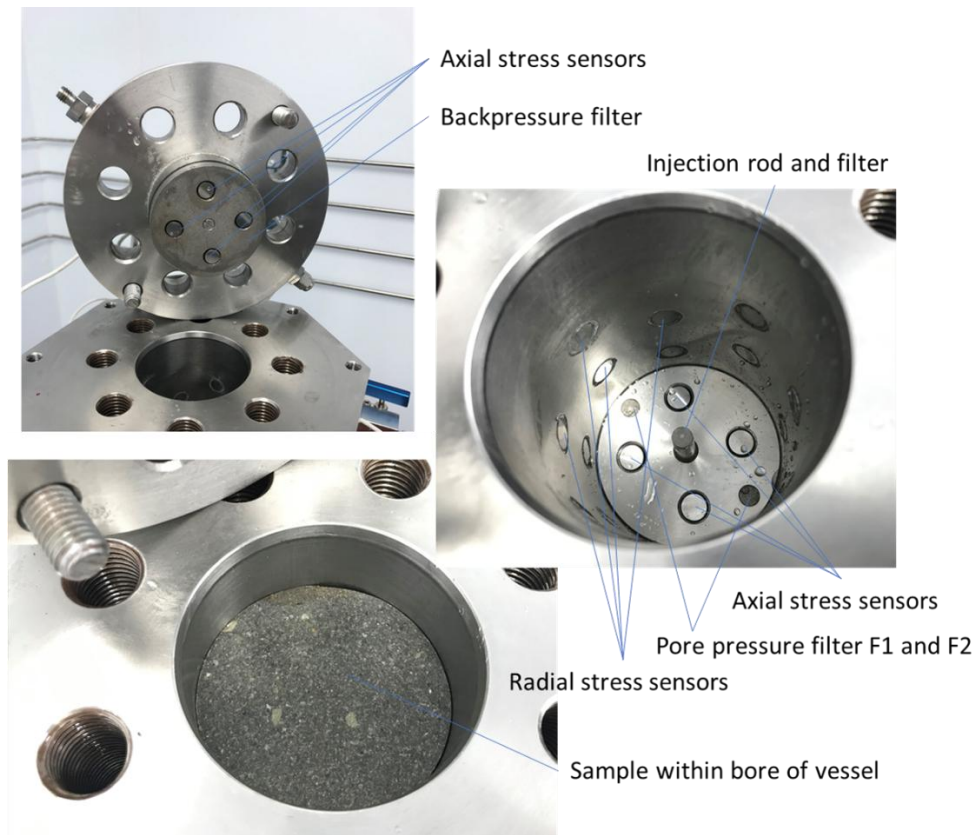
Figure 1. Photos of apparatus and the test sample installed within the bore of the vessel.

The 60 mm internal bore of the pressure vessel was honed and hard-chromed to give a highly polished surface. Two pore pressure filters, labelled F1 and F2, Figure 1, were mounted in the lower end-closure and used to provide local measurements for pore pressure during the course of the experiment. The total stress sensors were located in a geometric pattern, Table 1, with 4 radial arrays, each comprised of four sensors, spaced evenly along the sample. Each end-closure also contained four axial total stress sensors, mounted in a square configuration, visible in Figure 1 and Figure 2 [C] and [D].

The central or injection filter was embedded at the end of a 6.4 mm diameter stainless steel tube and was used to inject helium (see section 2.1.3) during gas testing. The end of the filter was profiled to match a standard twist drill to minimise voidage around the injection tip.
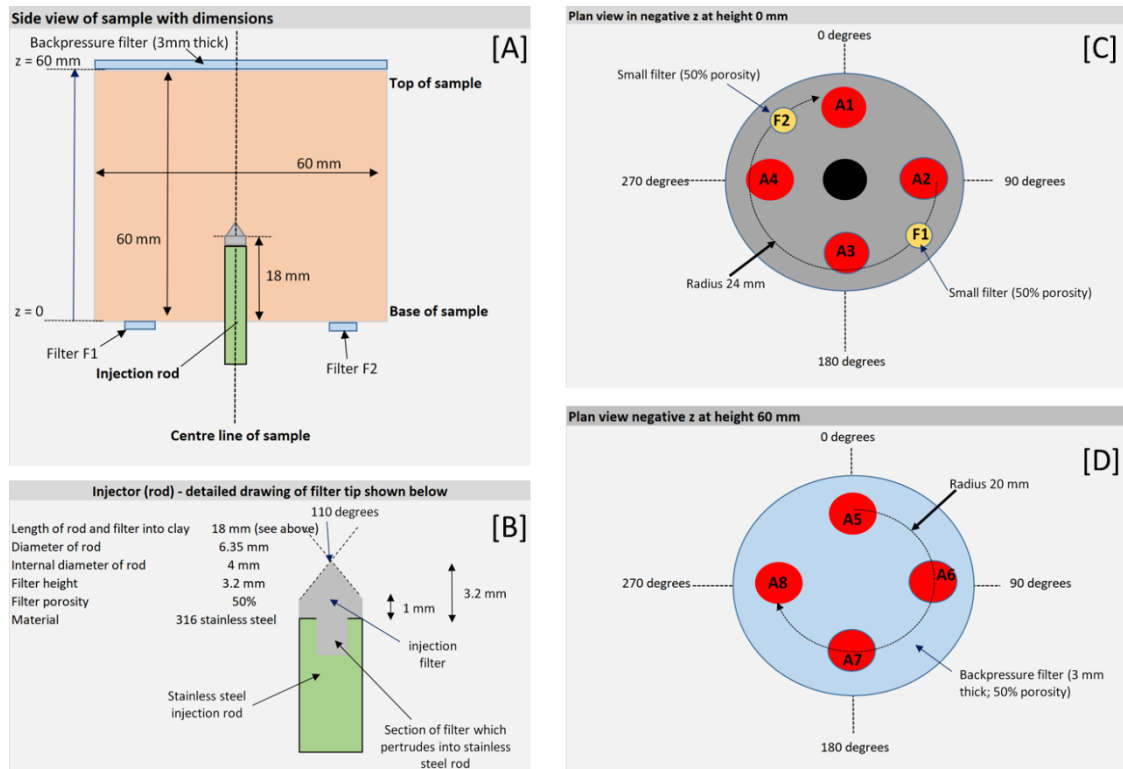
Figure 2. Schematic of apparatus. [A] shows the dimensions of the sample and filters. [B] shows the dimensions of the injection filter. [C] and [D] show the location of the axial sensors in contact with the base and top of sample respectively.

Pressure and flow rate of test fluids were controlled using two ISCO-260, Series D, syringe pumps, operating from a single digital control unit. Given the potential for gas leakage past the injection pump seal, a constant flow rate was developed by displacing the gas from a pre-charged cylinder by injecting water. This also helped to ensure that the helium was water-saturated with water vapour prior to injection, reducing the potential for desiccation. A second pre-charge vessel was placed in the backpressure circuit to collect the gas as it was discharged from the sample. Test data was over-sampled at an acquisition rate of one scan per 20 seconds. Thereafter, data processing was based on every 10th datapoint, unless something of note occurred within the data. All pressure transducers were calibrated to an accredited laboratory standard and linear least-squares regression fits were applied to the data. This ensured the output from each sensor could be compared, removing experimental artifacts due to the response of a particular sensor.

Table 1. Sensor locations. Sensor prefixed with the letter A=axial and R=radial. Radius equates to the centre line of the vessel running axially along its length. Height (z) is the distance from the base of the sample. Surface area relates to the circular size of the sensor/filter, see Figure 1.

Sensor name	Rotation (degrees)	Radius (mm)	Height, z (mm)	Surface area (mm²)
A1	0	20	0	50.27
A2	90	20	0	50.27
A3	180	20	0	50.27
A4	270	20	0	50.27
R1	0	30	12	50.27
R2	90	30	12	50.27
R3	180	30	12	50.27
R4	270	30	12	50.27
R5	45	30	24	50.27
R6	135	30	24	50.27
R7	225	30	24	50.27
R8	315	30	24	50.27
R9	0	30	36	50.27
R10	90	30	36	50.27
R11	180	30	36	50.27
R12	270	30	36	50.27
R13	45	30	48	50.27
R14	135	30	48	50.27
R15	225	30	48	50.27
R16	315	30	48	50.27
A5	0	20	60	50.27
A6	90	20	60	50.27
A7	180	20	60	50.27
A8	270	20	60	50.27
F1	135	24	0	28.27
F2	315	24	0	28.27

2.1.2 Geotechnical properties

Geotechnical properties for the test sample FPR-21-004 were not available at the onset of the modelling exercise, as testing was still ongoing. As such, geotechnical data was provided by a second sample, FPR-20-030, manufactured in exactly the same way as that for FPR-21-004, with data presented in Table 2. Data are calculated based on a grain density of 2.77 g/cm³.

Table 2. Geotechnical properties based on sample FPR-20-030.

Moisture content	Bulk density (kg/m³)	Dry density (kg/m³)	Void ratio	Porosity	Saturation
0.25	1989	1592	0.740	0.425	0.93

2.1.3 Test history

Details of each test stage are presented in Table 3. Sample FPR-21-004 was subject to a series of test stages to promote swelling and resaturation (stages 1 and 2), equilibration (stage 3) gas injection (stage 4) and self-sealing (stage 5).

Table 3. Experimental stages and boundary conditions for test FPR-21-004 (E=equilibration, H=hydration, G=gas ramp, S=shut-in).

Stage	Stage type	Start time (d)	Injection pressure gas (kPa)	Back-pressure water (kPa)	Filter F1 (kPa)	Filter F2 (kPa)	Gas disp. rate (μl/h)
1	E	0	0	250	250	250	-
2	H	3.1	1000	1000	1000	1000	-
3	E	27.2	1000	1000	1000	1000	-
4	G	28.4	2000+	1000	-	-	180
5	S	84.9	-	1000	-	-	-

2.1.4 Results

Following installation of the sample, a small backpressure of 250 kPa was simultaneously applied to the backpressure filter and both F1 and F2 filters, Figure 1. On day 3.1 (test stage 2), pressure in all three filters was increased to 1.0 MPa, and the sample allowed to hydrate. The subsequent development of axial and radial stresses is shown in Figure 3 and Figure 4. At the same time, water pressure was increased and the gas (helium) pressure in the injection filter was also incremented to match the change in water pressure. This was done in order to prevent accidental water flow into the filter and thus remove the possibility of slug flow (i.e., gas displacement of water from the filter ahead of gas entry into the sample) during gas injection (stage 4).

Examination of the axial stress data, Figure 3, shows a progressive increase in stress, axially throughout the sample. Unsurprisingly, stresses were systematically higher at the top of the core, adjacent to the large backpressure filter, and thus had unlimited access to water. At the base of the sample, access to water was limited to that available in the small filters F1 and F2, see average stresses A1-A4 in Figure 3[B]. By the end of stage 2, this resulted in an average axial stress of 7.5 MPa, compared to 8.5 MPa at the top of the sample. Close inspection of the data in Figure 3 indicates that swelling was ongoing at the end of stage 2. However, based on the final 5 days of data from this stage, the rates of change were relatively small: 11.3 and 3.4 kPa/d for A1-A4 and A5-A8 respectively. The higher rate of change in the base of the sample relates to the aforementioned availability (or rather lack) of water. It is also noteworthy that by the end of the stage, the variation in axial stress measured across each plane was very similar, at 0.69 MPa and 0.63 MPa for A1-A4 and A5-A8 respectively, see Table 4.

The development of radial stress evolves in a similar manner to that of the axial stress. When the clay was exposed to water, radial stresses also rapidly increased, Figure 4, approaching a well-defined asymptote by the end of the stage. Inspection of the data shows some variability, even across the same plane of measurement, such as the difference in values between sensors R9 to R12, or R13 to R16. Analysis of the data in Table 4 indicates larger variations in pressure exist as the distance to the points of measurement increase from the three sources of hydration. This results in some degree of heterogeneity in the resultant stress field at the end of stage 2, probably linked to a combination of incomplete homogenisation of the bentonite and subtle variations in the microstructure of the sample. The data in Figure 5 indicates that average radial stress does not change along the length of the sample, and by the end of the test axial and radial stresses are approximately equal. This suggests that friction between the sample and vessel wall is likely to play a small (if any) role in the development of the stress on

the scale of the experiment. The difference between axial stress at the top and bottom of the sample (Figure 3) therefore relates to the availability of water (which is less at the base of the sample) suggesting incomplete homogenisation at this region of the sample. However, the length of time required to fully homogenise bentonite is unclear and remains a research priority within the international community. As time was limited and the average values of radial stress, Figure 5, were relatively similar across each measurement, the sample was deemed ready for gas testing.
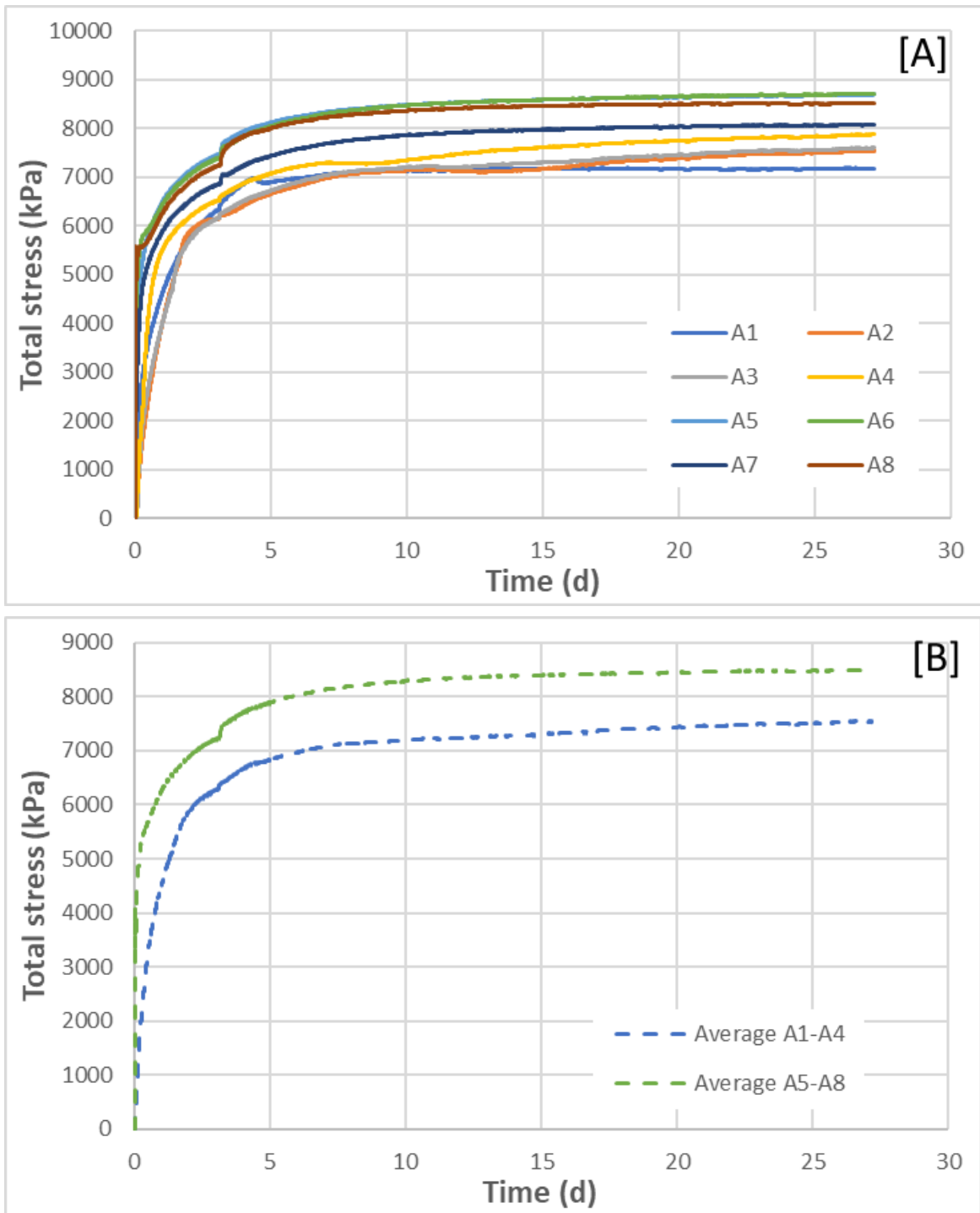
Figure 3. Test FPR-21-004 showing the development of axial stress during test stages 1 and 2. In [A] each sensor is shown and in [B] the average stress is shown: sensors A1 to A4 (located at the base of the sample) and A5 to A8 (positioned on the top face of the sample).
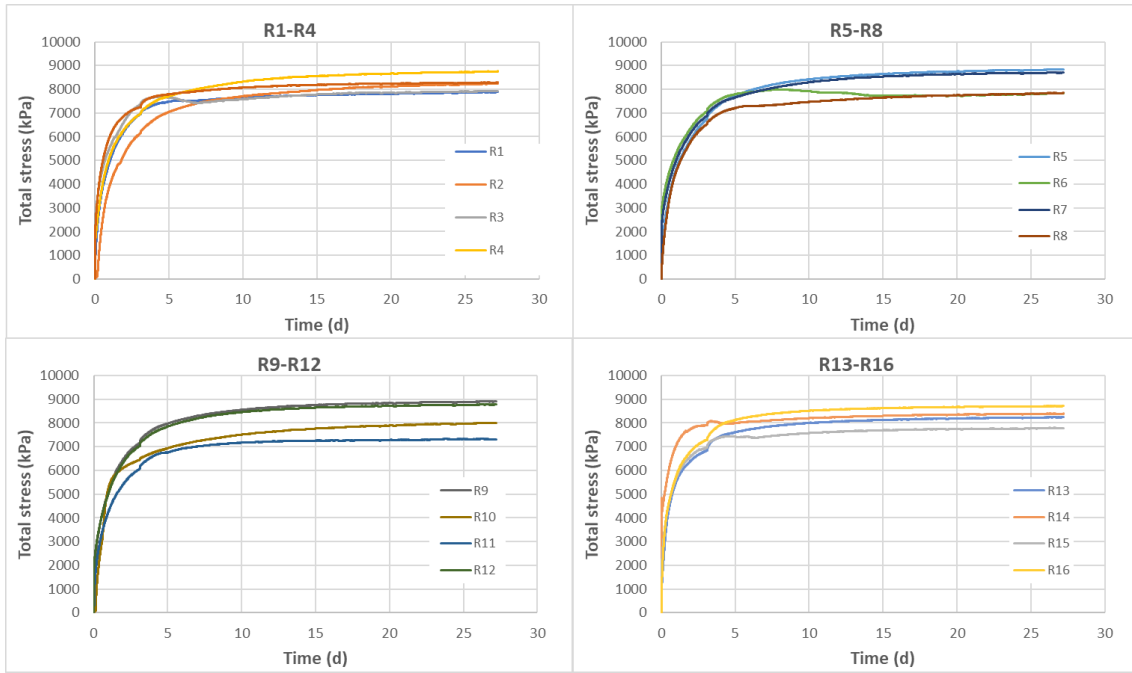
Figure 4. Test FPR-21-004 showing the development of radial stress during test stages 1 and 2. Sensors R1-R4 are closest to the base of the sample and R13-R16 are closest to the top of the sample, Figure 1.

Table 4. Minimum and maximum pressures at the end of stage 2 for test FPR-21-004.

Sensors	Max value at end of stage 2 (MPa)	Min. value at end of stage 2 (MPa)	Difference in pressure (MPa)
A1-A4	7.86	7.17	0.69
R16-R13	8.71	7.79	0.92
R12-R9	8.90	7.32	1.58
R8-R5	8.83	7.82	1.01
R4-R1	8.75	7.88	0.87
A5-A8	8.70	8.07	0.63
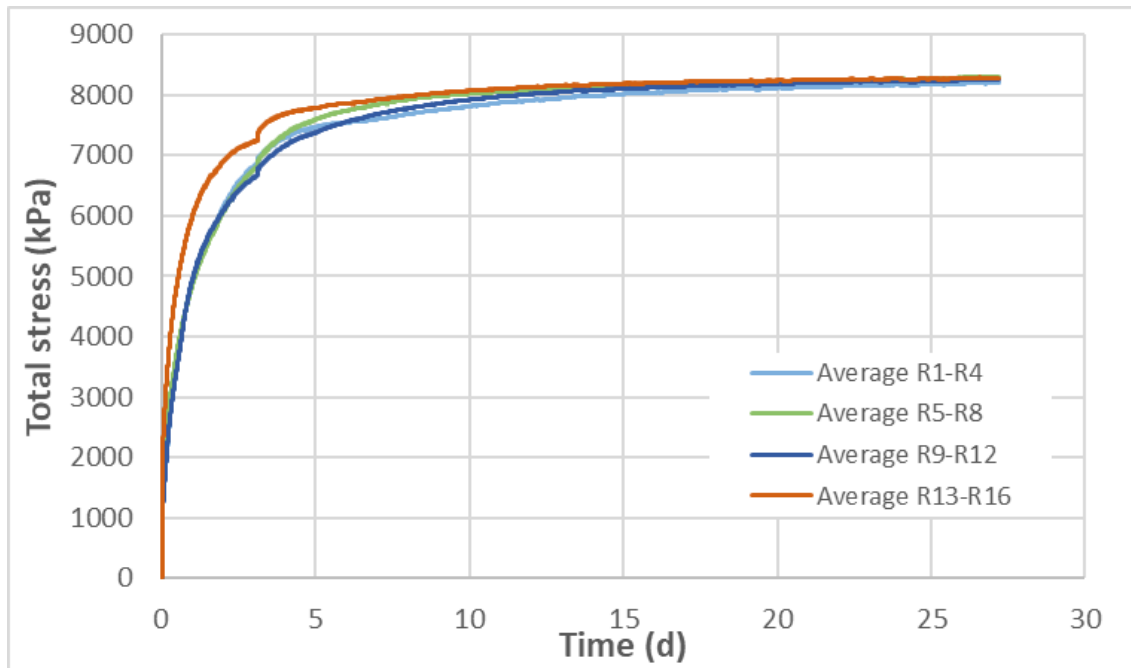
Figure 5. Test FPR-21-004 showing the development of radial stress at each plane of measurement during test stages 1 and 2. The position of each 'array' is in Table 1.

Following a brief period of further equilibration, gas testing (stage 4) began on day 28.4 with the injection pump set at a constant displacement rate of 180 µl/h. Gas pressure gradually increased for the following 49.4 days, reaching a peak value of 12.36 MPa at day 77.8, see Figure 5. This was followed by a spontaneous negative pressure transient leading to a quasi-steady state around day 84.9. At this point, the injection pump was stopped, test stage 5, and the pressure allowed to slowly decay. Gas pressure continued to decline until the test was stopped at day 117.

Closer inspection of the axial stress data, see Figure 6[A], suggests a small gas entry (i.e., onset of flow into the clay) event occurred around day 70.1, shortly after gas pressure exceeded the lowest value of axial stress. However, inspection of the outflow data, Figure 6[B], shows no obvious sign of discharge. In the absence of a suitable sink, gas pressure therefore continued to increase, finally resulting in a major gas entry event around day 74.3 at a gas pressure of around 9.84 MPa. In the intervening time between the precursor and major entry events, the rate of change in all stress traces began to increase, providing clear evidence of a hydrodynamic effect caused by the coupling between gas pressure and axial stress.
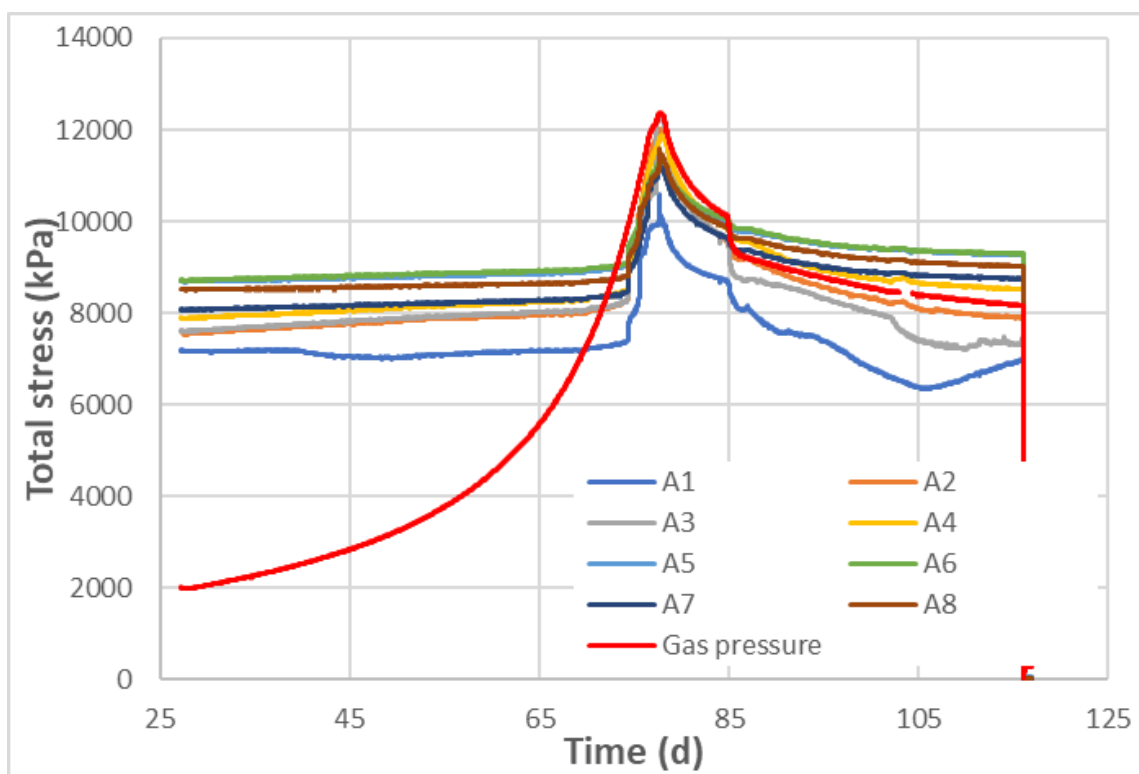
Figure 6. Test FPR-21-004 showing the development of gas pressure and axial stress, stage 5. The gradual increase in most sensors from day 28 to 70 can be attributed to continued hydration of the bentonite.

Further examination of the outflow data following the major gas entry event at day 74.3, Figure 7[B], suggests a very small increase in outflow occurred around this time, possibly caused by compaction of the clay following major gas entry. However, gas breakthrough did not occur until day 75.5, from which it can be inferred that it took 1.2 days for sufficient pathways to develop and locate the backpressure filter. At this point, outflow rapidly increased and was associated with a series of rapid changes in the stress field, Figure 7[A]. However, the initial development of permeability was short-lived, as conductive pathways began to close and outflow quickly decreased. From day 76.1 to 76.5, outflow reduced to pre-major breakthrough levels and was accompanied by further increases in gas pressure and stresses within the sample, as gas pathways developed to reconnect with the backpressure filter. Towards the right margin of Figure 7[B], outflow from the sample spontaneously increased for a second time at day 76.5 and was again associated with complex changes in the stress field.
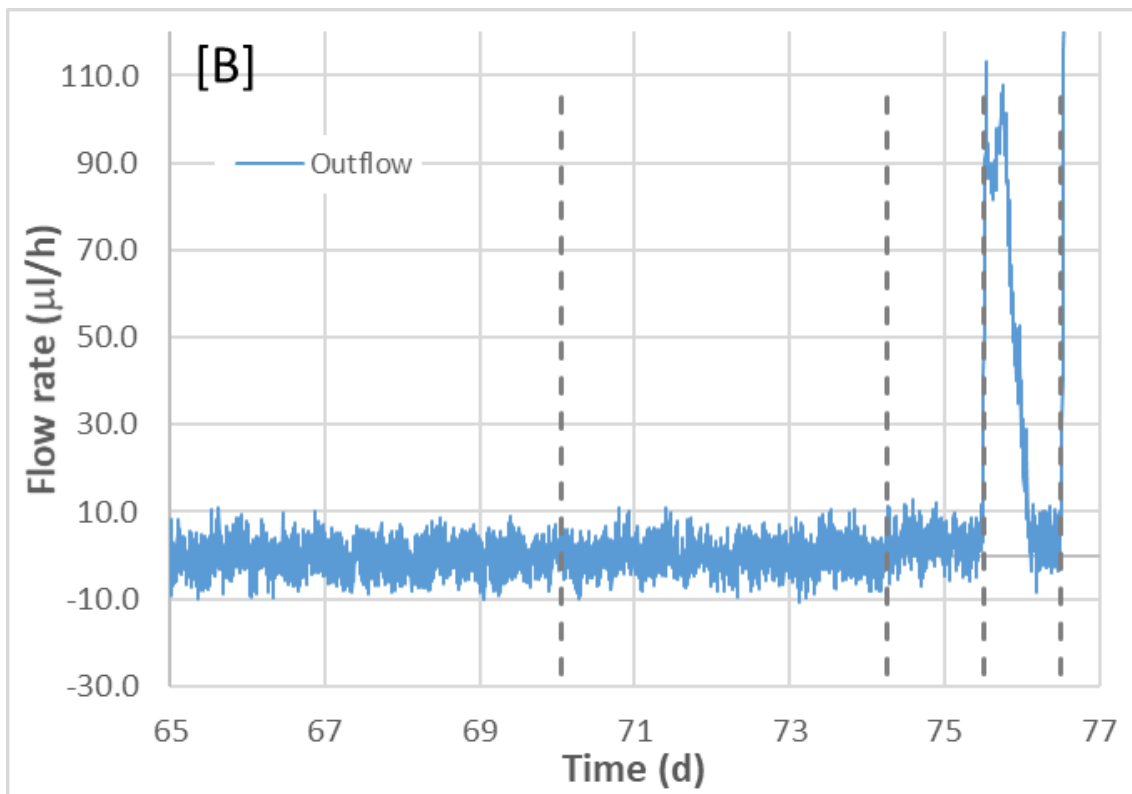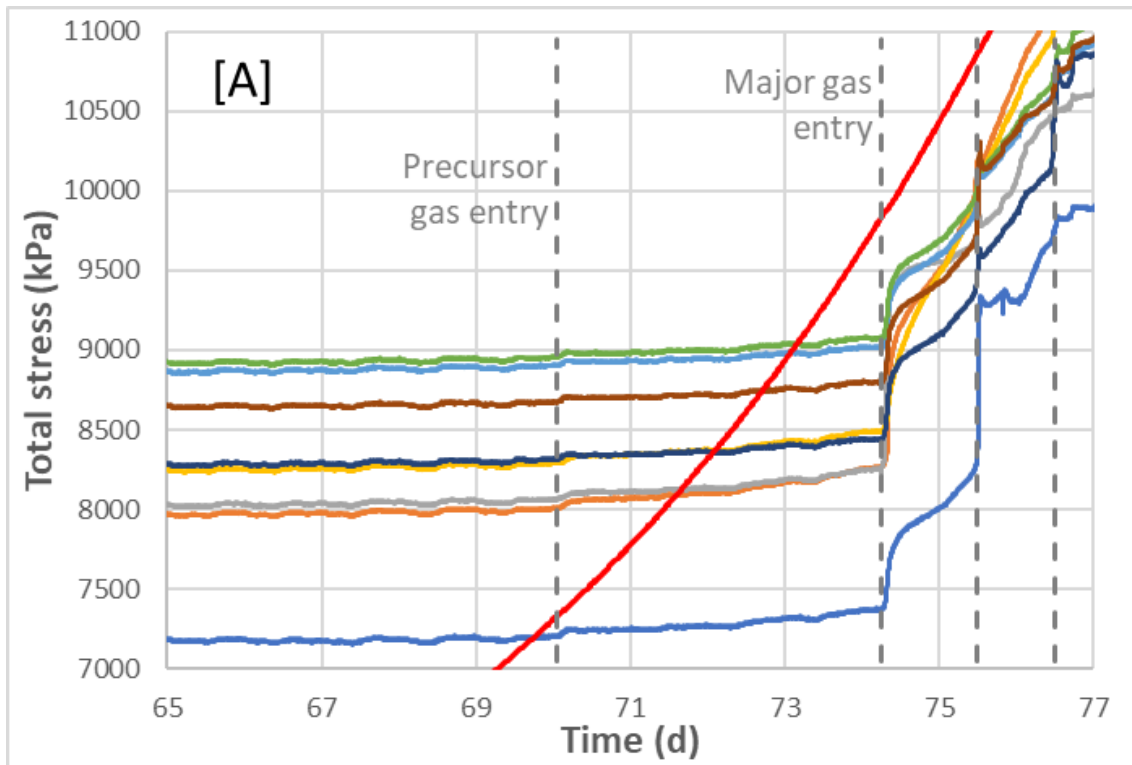
Figure 7. Data from part of stage 4 of test FPR-21-004 with dotted lines denoting significant events. [A] expanded view of gas pressure and axial stress data showing precursor gas entry around day 70.1 followed by major gas entry at day 74.3. Line colours are the same as those on Figure 6. [B] shows time averaged outflow data under experimental conditions with major gas outflow occurring at day 75.5.

Figure 8 shows the evolution of axial stress in response to the development of flow out of the sample. Gradual and abrupt changes in gas pressure and stress were observed which are thought to link to the development of flow paths within the sample. Following major gas breakthrough outflow, stress and gas pressure were highly coupled. In general, gas pressure remained slightly above that of axial stress, suggesting some degree of pressure drop along gas pathways. However, the orientation of the pathways to the direction of stress measurement strongly impacts the measured value of stress. Therefore, a detailed analysis of the stress response (axial and radial) is required and will be undertaken at a future date.

While the peak gas pressure response was more rounded in shape compared to the that of outflow, peak gas pressure occurred prior to peak outflow. This suggests a degree of time-dependent behaviour in the development of gas pathways and thus effective gas permeability within the sample. However, by the end of the test stage at day 84.9, Figure 8[B], inflow and outflow were converging, signifying the test was approaching a near steady state condition. However, close examination of the data shows small discrepancy between inflow and outflow data at day 84.9. As the system was not in true steady-state, it is not possible to identify the true origin of this discrepancy, but might stem from a small background leak.

As soon as the injection pump was stopped, gas pressure, axial stress and outflow from the sample rapidly decreased, Figure 9. For the first time, gas pressure dropped below axial stresses A2 and A5 through A8, suggesting depressurisation of some pathways and trapping of residual gas in others. From day 87, a more gradual decline in gas pressure and axial stress was observed. By the end of the stage, gas pressure was over 1.0 MPa lower than axial stress at sensors A5 and A6. Examination of Figure 9 indicates the variation in total stress increases as the shut-in stage progresses. This is likely caused by the localised closure of gas pathways, resulting in the entrapment of gas within the sample, perturbing the stress field.

The disconnect between outflow and changes in axial stress and gas pressure suggests complex patterns of flow drainage, which spatially and temporally evolved within the clay. Pathway closure can therefore be rapid, as in the early stages of the shut-in response, or slow, as illustrated by the subsequent gradual decline in axial stresses and gas pressure. The former may be driven by the elastic (compressibility) of the material and the other by the slow diffusion and egress of gas trapped along now partially sealed pathways.

Figure 10 shows the evolution of radial stress during gas injection, test stages 4 and 5. These sensors showed qualitatively similar behaviour as that previously discussed for

axial stress. Considerable variations in stress values were observed across each plane, Figure 11, ranging from 140 kPa to 2650 kPa. The data clearly shows the evolutionary and complex nature of the stress field induced during advective gas flow and is likely linked to the localised internal development of gas pathways within the clay.
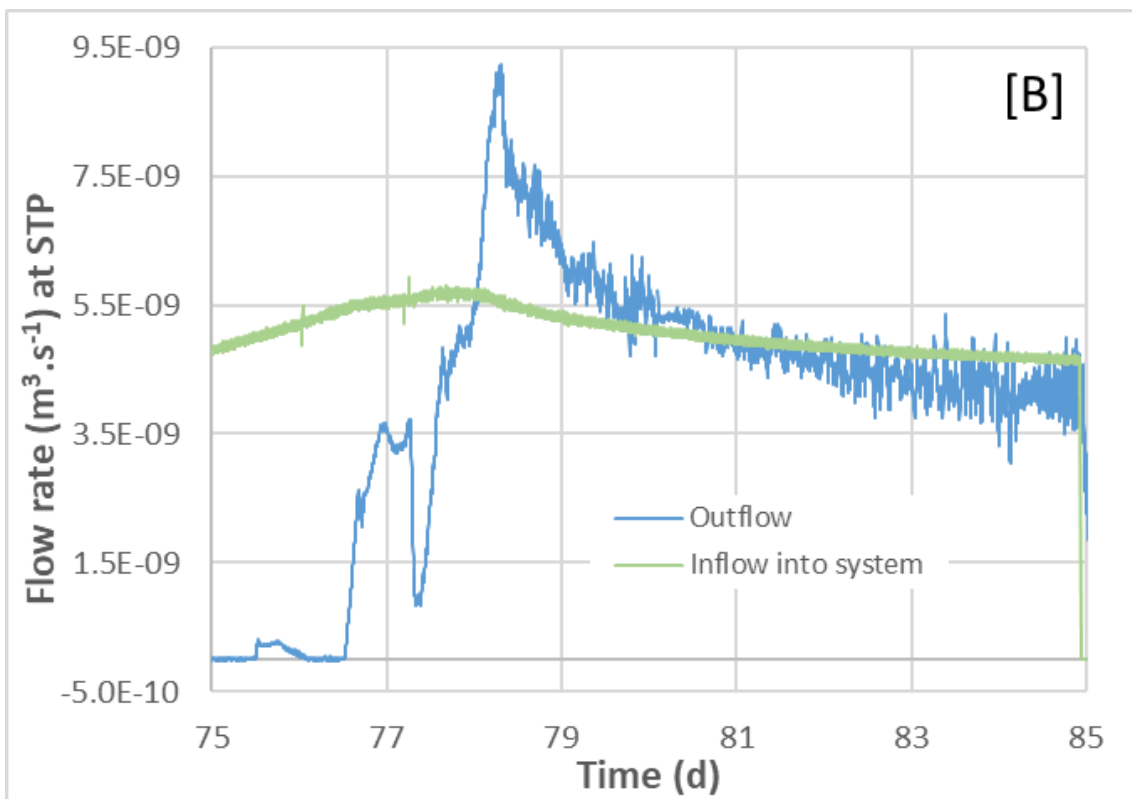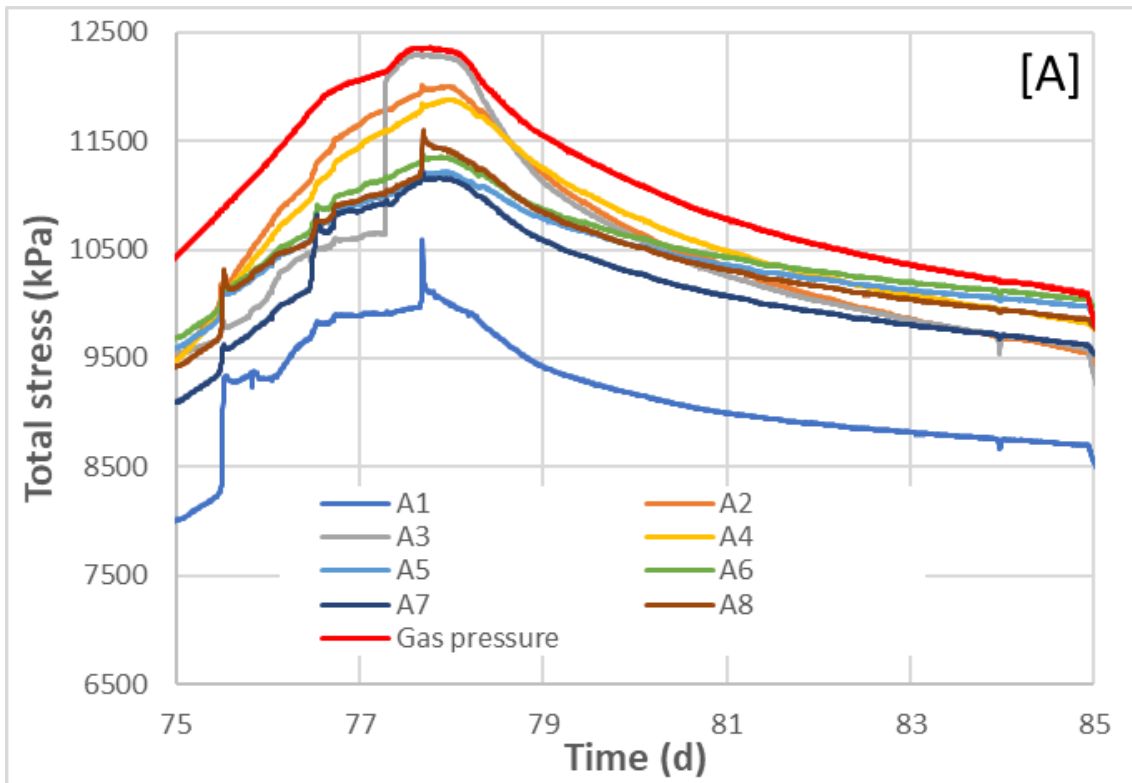
Figure 8. Data from part of stage 4 of test FPR-21-004. [A] development of axial stress and [B] evolution of inflow and outflow data at STP, from day 75-85. Combined, the data illustrates the complex coupling between development of flow and accompanying changes in stress within the bentonite.
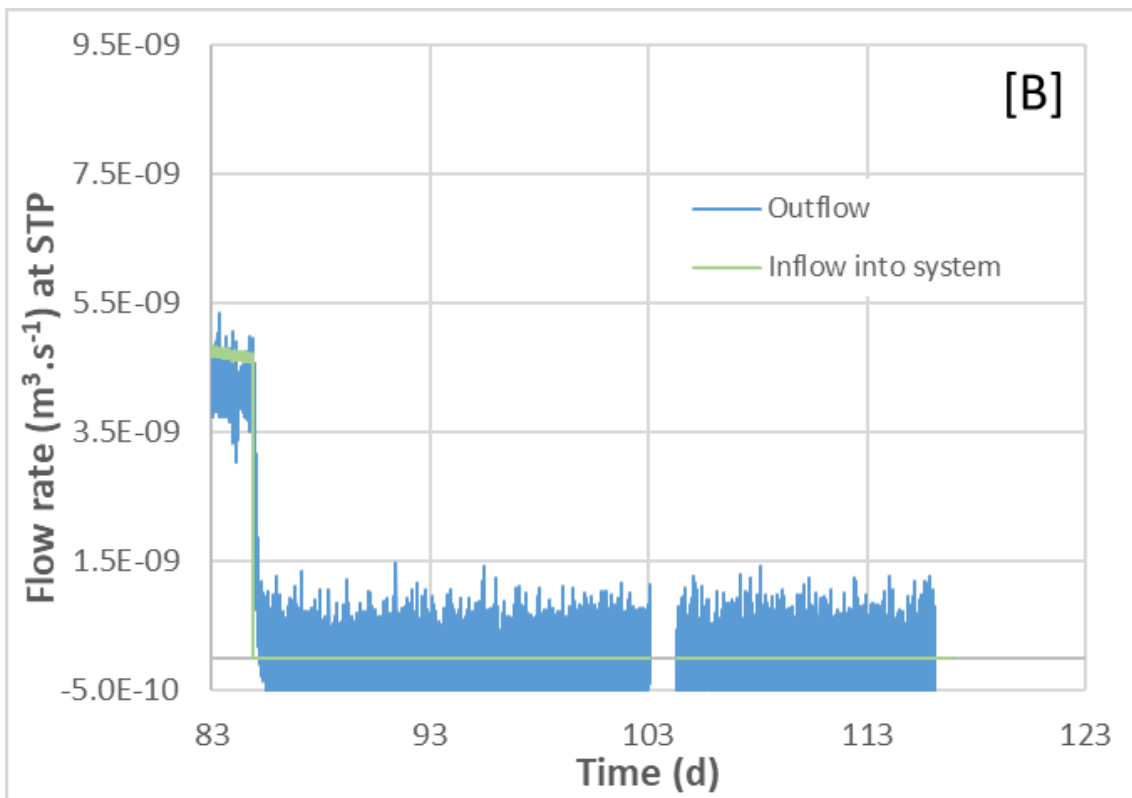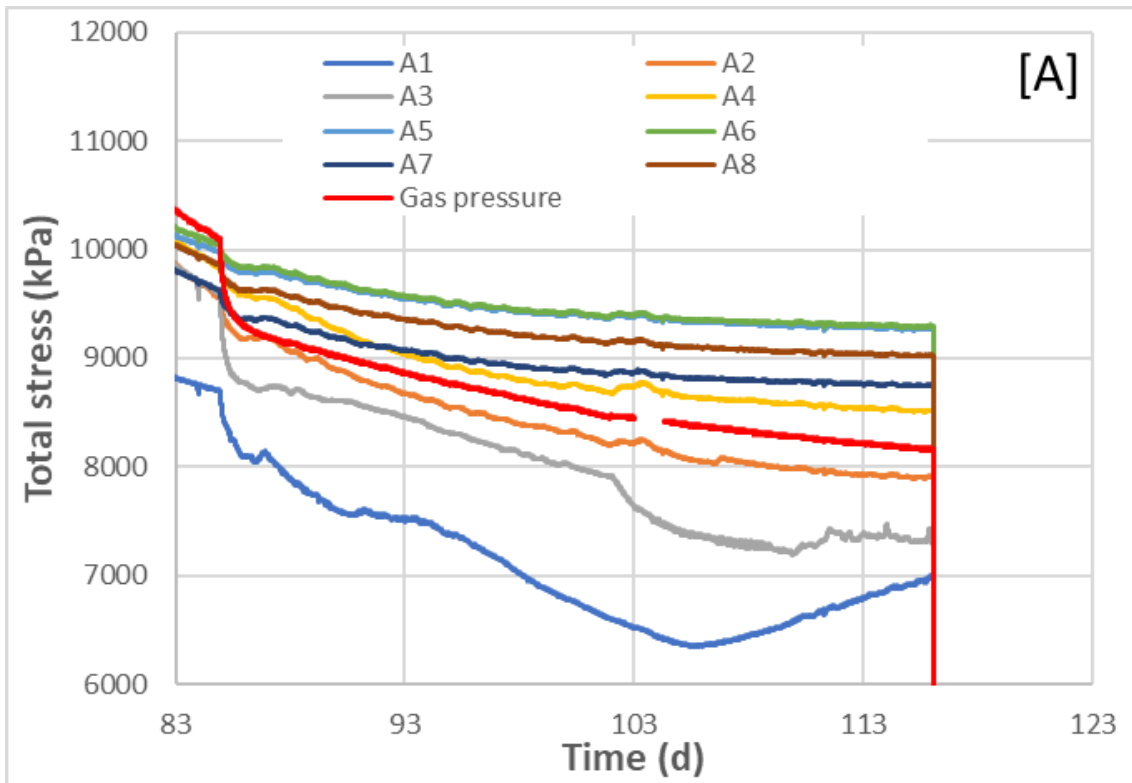
Figure 9. Shut-in, test stage 5, for sample FPR-21-004. [A] change in gas pressure and axial stress and [B] evolution of outflow (at STP) following the cessation of pumping at day 84.9 (the missing data at day 103 was caused by a problem with the data logger).
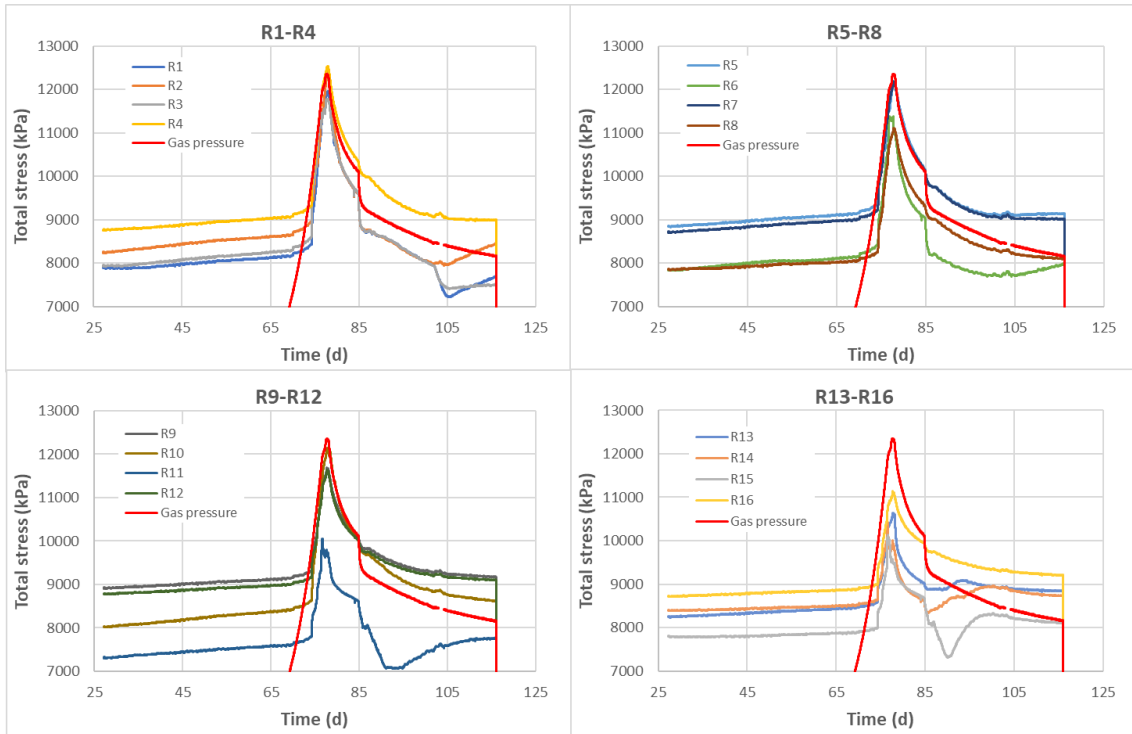
Figure 10. Radial stress data for FPR-21-004. Radial stresses R13 through R16 register the lowest values as these sensors were located below the injection filter.
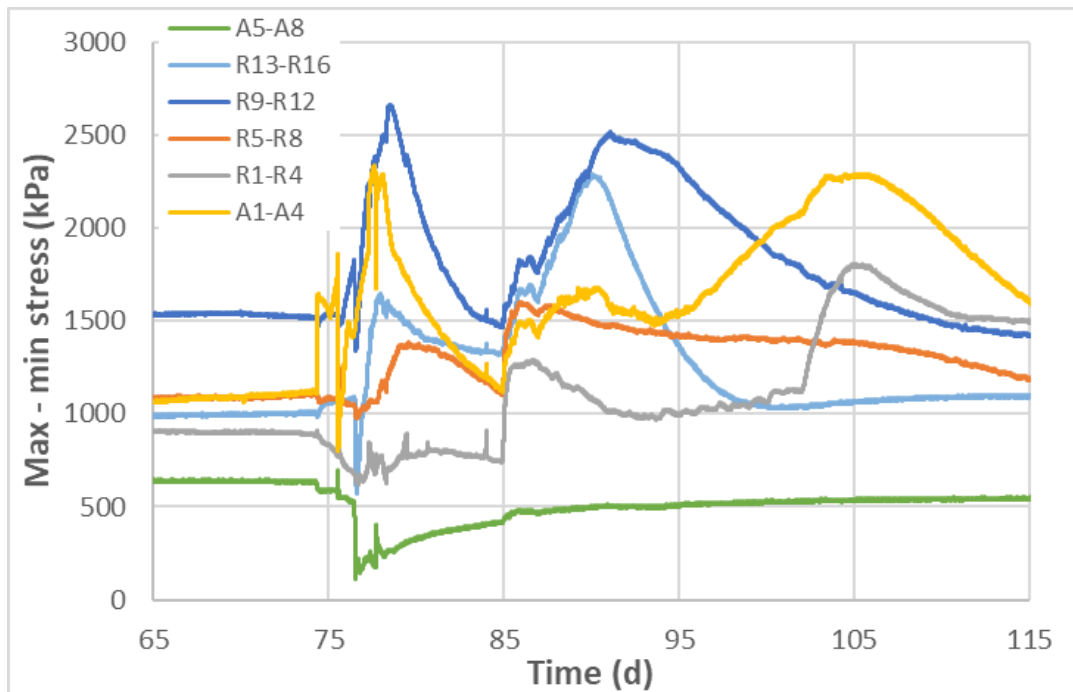
Figure 11. Difference between maximum and minimum stress at each axial and radial plane of measurement plotted as a function of time.

A plot of average stress for each plane of measurement, Figure 12, shows that once major gas entry occurred, stress increased fairly consistently throughout the sample with the exception of R13-R16. Here peak stress was substantially lower compared to all other arrays, suggesting fewer pathways propagated towards the top of the sample. In contrast, during the major gas entry and breakthrough events, average stress values for A1-A4 were similar to those in array A5-A8, suggesting some pathways must have been horizontally orientated across the vertical axis of the sample. The highest stress values occurred in array R1-R4, closest to the backpressure filter, indicating that (1) the gas pressure gradient induced presumably small pathways and (2) most of the pressure drop between the gas phase and the water within the backpressure filter occurred in a narrow zone close, or at, the edge of the sample.
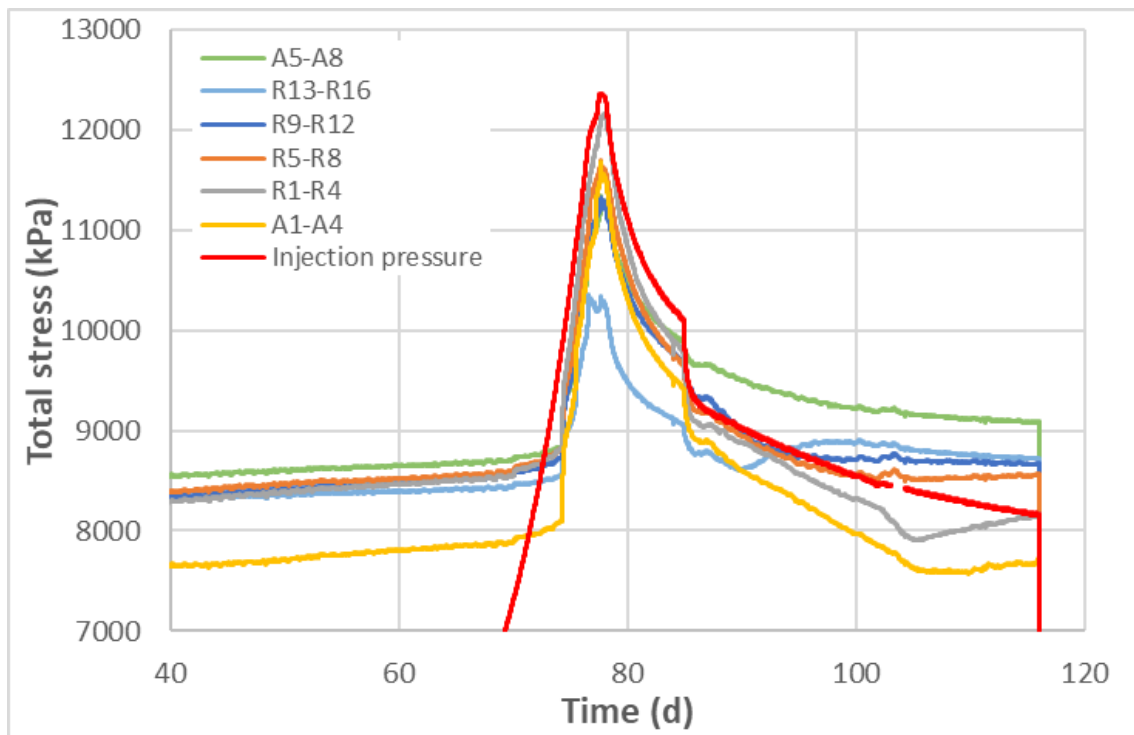
Figure 12. Average stress at each plane of measurement along the axis of sample FPR-21-004.
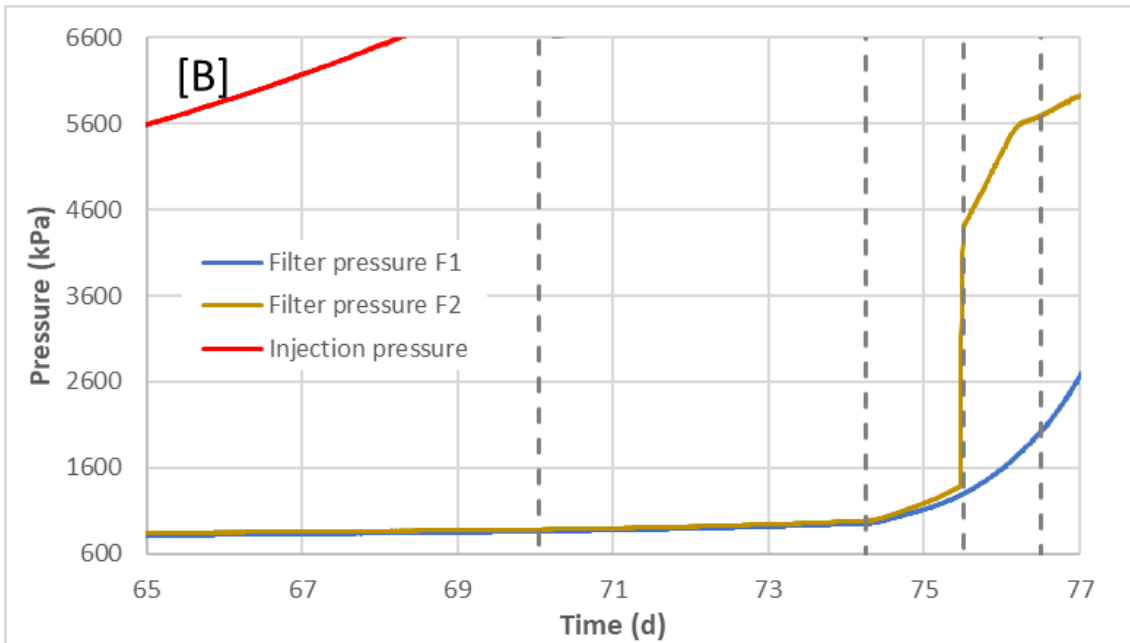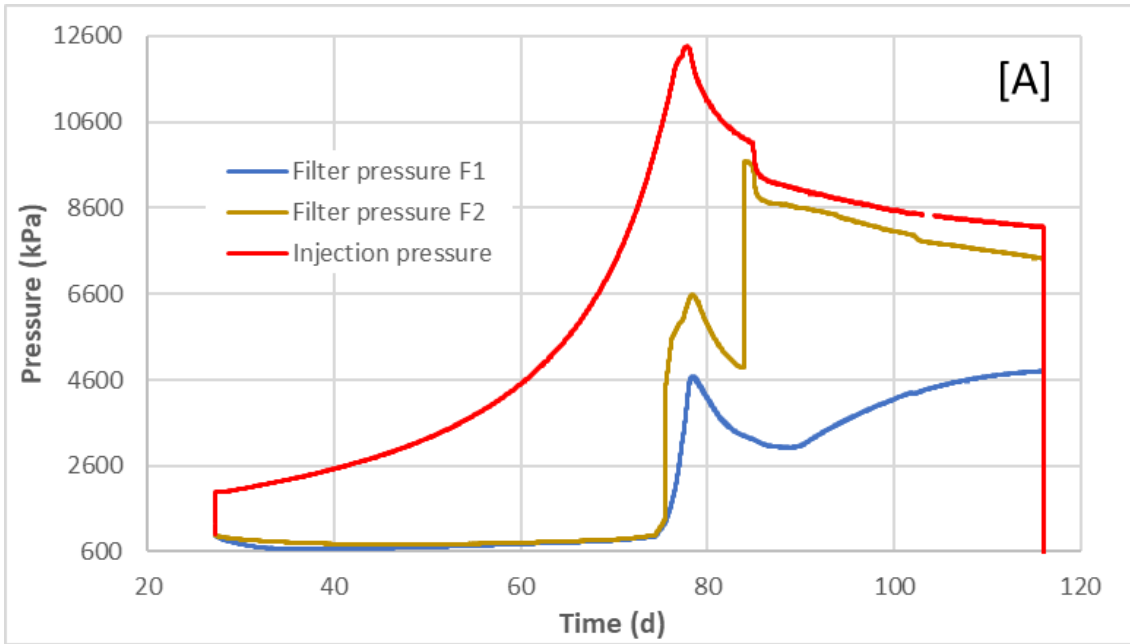
Figure 13. [A] pore pressure development in filters F1 and F2 during test FPR-21-004. [B] expanded data from day 65 to day 77 showing the filter response during initial gas entry, major gas entry, initial gas breakthrough and major gas breakthrough respectively from left to right.

The evolution in pore pressure at filters F1 and F2, within sample FPR-21-004, is shown in Figure 13[A]. Following the cessation of hydration at day 27.2, a gradual decrease in pressure was observed, illustrating that the sample was not in full hydraulic equilibrium at the onset of gas testing. As hydration continued from the backpressure filter, a

gradual increase in water pressure was seen from around day 38 and 49 in filters F1 and F2 respectively. Figure 13[B] shows the development of pore pressure during gas entry and subsequent breakthrough events. As major gas entry occurred at day 74.3, both filters showed an increase in pressure, probably related to a hydrodynamic effect during the displacement and compaction of the clay at gas entry. As injection gas breakthrough occurred at day 75.5, filter F2 showed a rapid increase in pressure, most likely due to the arrival of gas at the filter. Gas pressure peaked at 6.64 MPa and then began to gradually decrease. A second breakthrough event in the same filter, occurred at day 84 when pressure rapidly increased. Filter pressure then appeared correlated to the gas pressure with an offset of around 0.7 MPa by the end of stage 5. This data also demonstrates that the pressure drop along the connected gas pathways, from the injection point to the filter, was relatively small.

In contrast, the development of pressure within filter F1 showed no abrupt changes in pressure associated with filter F2. This suggests that filter F1 was likely recording local hydrodynamic changes in porewater pressure due to displacement and localised compaction of the clay as gas pathways formed. However, the increase in pressure of filter F1 from around day 87, as gas pressure declined, might be linked to the slow discharge of gas into the filter as the pathways began to drain.

2.2 Full-scale gas injection test

The final stage of the task was designed to assess the modelling capabilities against a full-scale gas experiment. In particular, models were employed to simulate one of the gas injection experiments (gas injection test 4) performed as a part of the Lasgit project (LArge-Scale Gas Injection Test), see Figure 14. Lasgit was a full-scale demonstration experiment operated by The Swedish Nuclear Fuel and Waste Management Company (SKB) at the Äspö Hard Rock Laboratory at a depth of 420 m, with the two main objectives of providing quantitative data to improve process understanding and validating modelling approaches used in performance assessment, see Cuss et al. (2022) for a detailed description of this 17-year project.

Figure 14. A panoramic view of the Large-scale gas injection test (Lasgit) 420 m below ground at the Äspö Hard Rock Laboratory in Sweden (from Cuss et al. 2022). The blue container on the left housed the artificial hydration and gas injection systems which were connected into the borehole along channels cut into the gallery floor. The cap and rock anchors of the deposition hole can be seen into the centre right.

2.2.1 Test history

Gas injection test 4 started on Day 2726.08 (20th July 2012) and was completed at Day 3283.06 (26th January 2014), lasting for a total stage time of 556.98 days. It was the third gas injection test conducted in filter FL903, located on the lower array of filters on the canister surface, see Figure 15. It comprised of two stages: (1) a two-stage hydraulic test to determine the hydraulic properties of the bentonite at filter FL903 and (2) a gas injection test, where gas pressure was raised from background levels up to gas peak pressure using a four-stage ramp, being held at constant pressure in between, which is the focus of the modelling exercise.

In this test, approximately 3750 ml of helium was added to a stainless steel interface vessel, located within the blue container (Figure 5) at a starting pressure of 1868 kPa. The injection filter was thoroughly flushed of water using pressurised helium and the drain from filter FL903. Once flushed, it was common for flow to take a few days to stabilise as gas went into solution and any remaining water within the filter was expelled into the bentonite. The first pressure ramp was started at Day 2988.07 (8th April 2013)

by the injection of water into the base of the interface vessel at a rate of 2.45 ml h^{-1}. This raised pressure from 1868 to 2867 kPa in 23.9 days, as shown in Figure 16, when pressure was held constant from Day 3011.99 for 26.0 days. The second pressure ramp was started at Day 3038.04 on (28th May 2013) by the injection of water into the base of the interface vessel at a rate of 1.2 ml h^{-1}. This raised pressure from 2868 to 3856 kPa in 23.1 days, after which pressure was held constant from Day 3061.17 for 26.1 days. The third pressure ramp was started at Day 3087.24 (16th July 2013) by the injection of water into the base of the interface vessel at a rate of 0.725 ml h^{-1}. This raised pressure from 3867 to 4852 kPa in 23.2 days, after which pressure was held constant from Day 3110.48 for 52.6 days. The fourth, and final, pressure ramp was started at Day 3163.04 (30th September 2013) by the injection of water into the base of the interface vessel at a rate of 0.35 ml h^{-1}. This raised pressure from 4854.01 to a gas peak pressure of 6174 kPa at Day 3205.31, 42 days after the start of the fourth pressure ramp. The injection of water into the base of the interface vessel continued at 0.35 ml h^{-1}, until Day 3235.13 when flow was reduced to 0.175 ml h^{-1}, and Day 3256.19 when it was reduced further to 0.088 ml h^{-1}. Injection was stopped at Day 3283.02 (28th January 2014) and in total, 2910.5 ml of water was injected into the base of the interface vessel. For a detailed description of each gas ramp, authors refer to the Lasgit final report by Cuss et al. (2022).
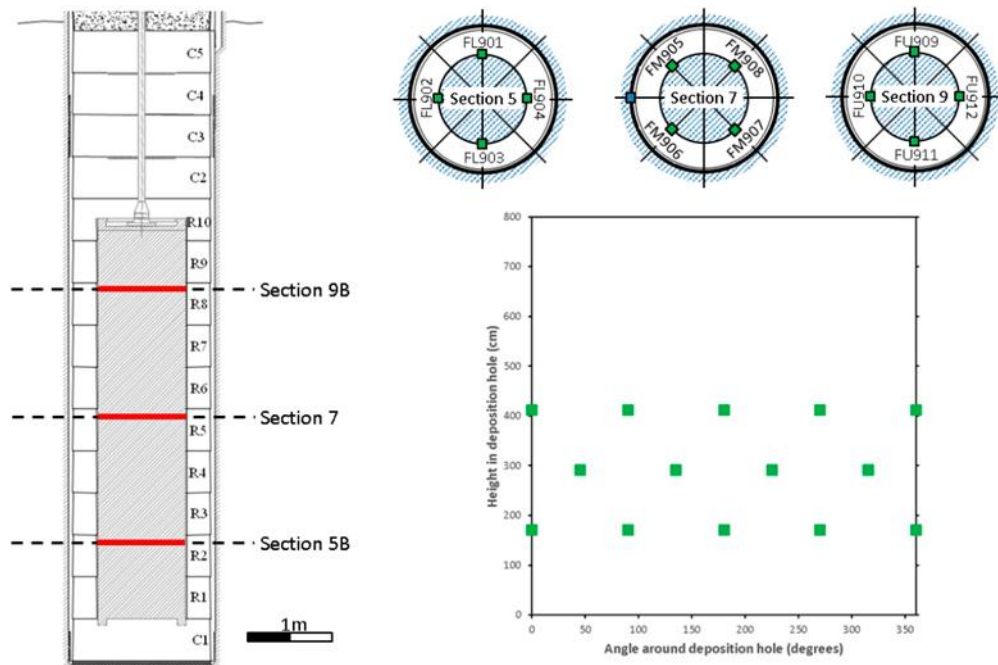
Figure 15. Plan view of the location of the canister filters (from Cuss et al. 2022).
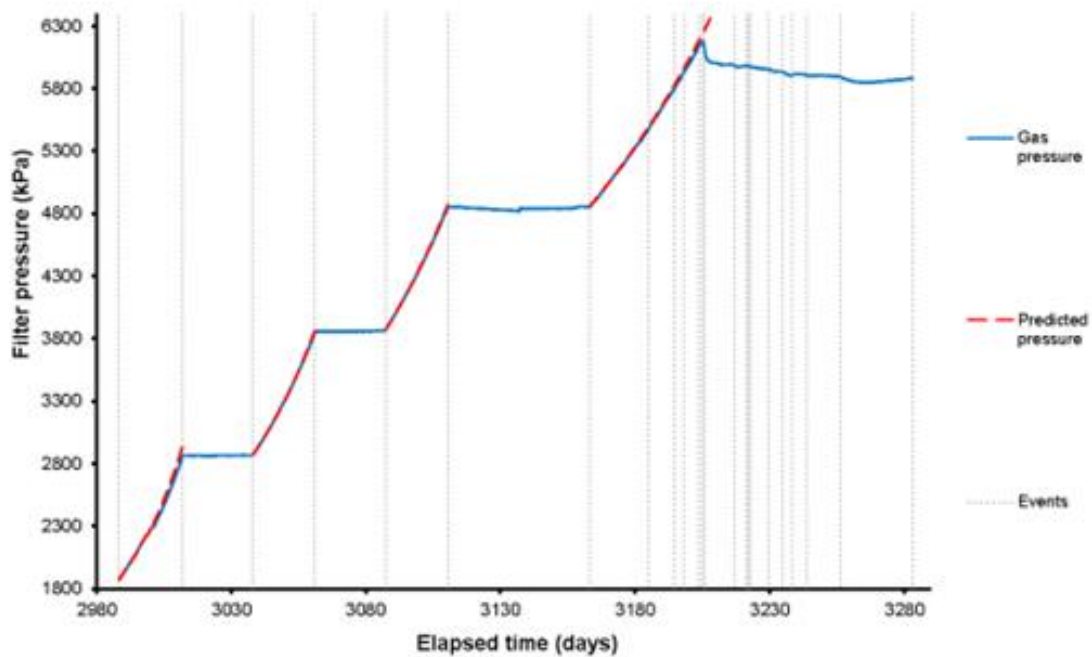
Figure 16. Recorded and predicted gas pressure during Gas Test 4 (from Cuss et al. 2022).

2.2.2 Results

Figure 17 shows the flow of gas into the system and into the clay at STP. As clearly seen, the rate of gas entry reduced between each successive gas ramp. Flow into the clay was seen in each ramp, with little flow observed during periods of constant pressure. In particular,

- Throughout the first gas ramp, the STP flow into the clay ranged from 1.25×10^{-8} to 1.48×10^{-8} m^3s^{-1}. This resulted in a small flow into the clay, with 0.1 mol entering the clay. As gas pressure was held constant at around 2867 kPa, a small amount of gas was seen to leave the buffer, as shown by a reducing cumulative volume of gas. Following this initial reduction, a flow rate of 17.8 µl h^{-1} was observed between Day 3021 and 3037, representing 282 µmol d^{-1}.

- Throughout the second period, the STP flow into the clay ranged from 9.3×10^{-9} to 1.24×10^{-8} m^3 s^{-1}. This resulted in a small flow into the clay, with 0.12 mol entering the clay. As gas pressure was held constant at around 3860 kPa, a total

of 0.014 mol entered the clay, with an average flow rate of 21.3 µl h^{-1}, representing 538 µmol d−1.

- Throughout the third gas period, the STP flow into the clay ranged from 7.51×10^{-9} to 9.41×10^{-9} m^3 s^{-1}. This resulted in a small flow into the clay, with 0.13 mol entering the clay. As gas pressure was held constant at around 4 853 kPa, a flow rate of 13.5 µl h^{-1} was observed, representing 651 µmol d^{-1}.

- Throughout the fourth gas ramp (where gas entry and peak pressure occurred), the STP flow into the clay ranged from 4.52×10^{-9} to 5.71×10^{-9} m^3 s^{-1}. This resulted in a small flow into the clay, with 0.21 mol entering the clay. Significant gas entry was seen to begin at Day 3203.73, as seen by an increase in flow rate into the clay. This resulted in a single peak in flow of 3.27×10^{-8} m^3 s^{-1} at Day 3205.72 (note: data shown in Figure 17 is time averaged). The peak in flow was short-lived with flow into the clay matching flow into the system within four days. From then afterwards the flow into the clay was slightly greater than the flow into the system, giving a slow reduction in gas pressure. As gas reduction appeared steady, the flow rate of the injection pump was lowered in two steps, approximately halving flow at each step. As before, flow into the clay approximated flow into the system, with slightly higher flow into the clay resulting in the continued reduction in gas pressure. However, in the final stage the flow into the clay reduced, resulting in an increase in gas pressure. In particular, 0.21 mol entered the clay up until peak gas pressure. Following gas entry, a total of 1.13 mol entered the clay.

As also seen in the lab-scale test, there exists a pronounced coupling between pore water pressures at the rock wall and gas entry (see Figure 18). Indeed, at Day 3203.73 (when flow accelerated), a response was seen in UR905 and UR908. This occurred at a gas pressure of 6141 kPa. At Day 3204.66, pore pressure at UR908 showed a stepped increase of around 12 kPa and radial stress at PR907 and PR908 started to increase, as did flow into the clay. At Day 3205.31, peak gas pressure occurred (at a pressure of 6174 kPa) resulting in a single peak in flow of 3.27×10^{-8} m^3 s^{-1} at Day 3205.72. This peak in flow was short-lived with flow into the clay matching flow into the system within four days. From then onwards the flow into the clay was slightly greater than the flow into the system, giving a slow reduction in gas pressure. Soon after the peak event, at Day 3205.88, pore pressure at UR905, UR907, and UR908 peaked. At Day 3206.40, radial stress at PR905, PR906, and PR907 increased by 8.6, 28.6, and 9.6 kPa respectively, while PR909 decreased by 7.1 kPa. Stress at PR908 increased from Day 3204.66 onwards and coincident with the changes seen in the other sensors reduced by ~5 kPa, before quickly recovering with a peak in stress ~15 kPa higher than the starting magnitude. Then, pore

pressure remained relatively static, until Day 3217.11, when some sensors (UR905, UR908, UR916 and UR919) showed small, short lived, reductions in pore pressure of ~4 to 10 kPa thus suggesting that gas flow was pulsed, see Cuss et al. (2022) for a detailed description of these events. At Day 3235.11, a decrease was seen in pore pressure at UR919, with disturbances in UR905, UR908, and UR916. Then, at Day 3238.16, a 10 kPa step reduction in UR908 was followed by irregular pore pressure. The flow rate of the injection pump was lowered in two steps, approximately halving flow at each step. Flow into the clay approximated flow into the system, with slightly higher flow into the clay resulting in the continued reduction in gas pressure measured in the interface vessel. In the final stage the flow into the clay reduced, resulting in an increase in gas pressure.
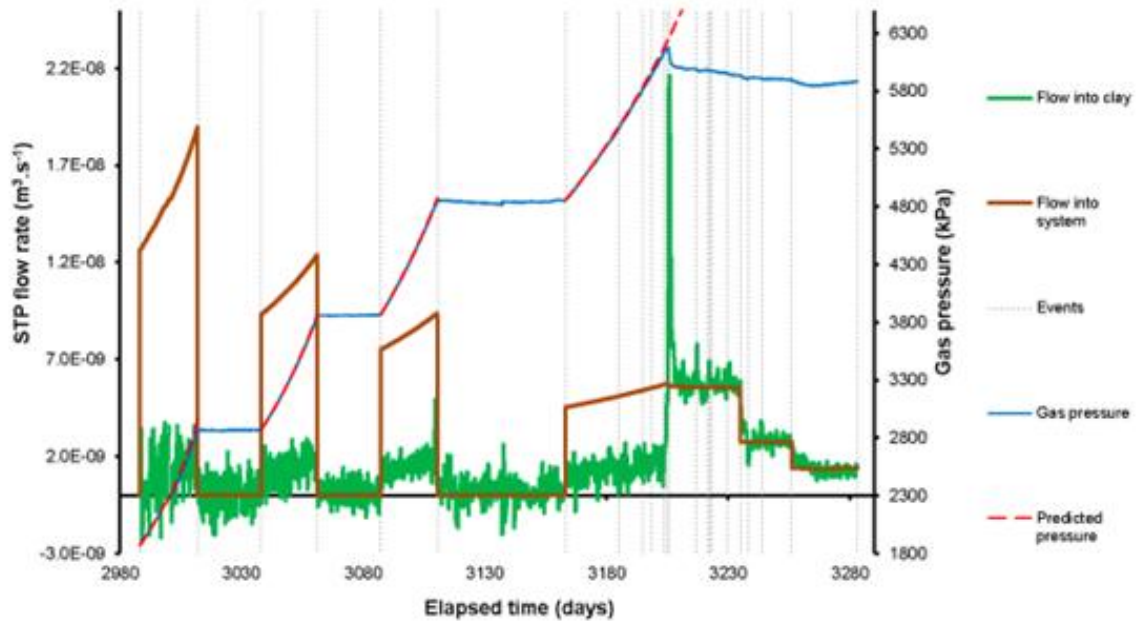
Figure 17. Flow of gas into the system and the clay during Gas Test 4 (from Cuss et al. 2022).
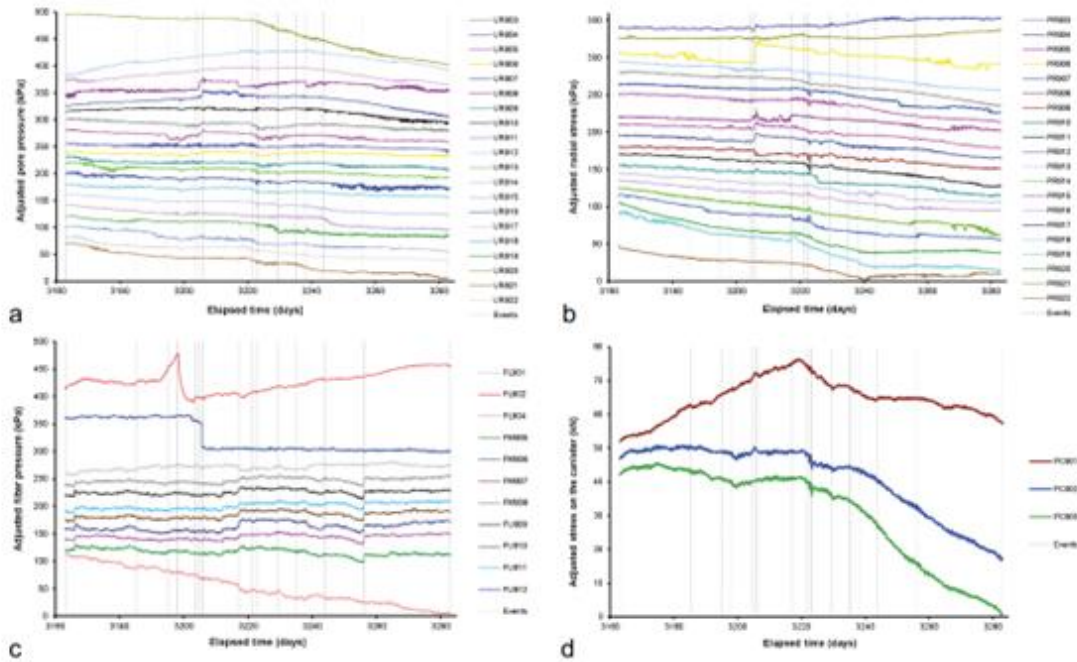
Figure 18. Example of sensor response around the time of gas entry during Gas Injection Test 4. All parameters have been transposed about the y-axis to emphasise the detail observed. a) Pore pressure at the deposition wall; b) Radial stress on the deposition wall; c) canister filter pressure; d) stress on the canister surface (from Cuss et al. 2022).

3   Modelling approaches

Five different approaches have been adopted by the participating teams. On the one hand, a conceptual model that analyses the complexity of the gas migration process by means of nonlinear dynamics and deterministic chaos theory has been developed by SNL. On the other hand, four different numerical approaches have been adopted by BGR/UFZ, KAERI, LBNL and CIMNE-UPC/Andra respectively. The numerical capabilities of three of these numerical approaches (BGR/UFZ, LBNL and CIMNE-UPC/Andra) were

first assessed by comparing the simulated results against the experimental ones obtained from the laboratory as part of a blind prediction exercise (stage 2) and then, after some modifications, were employed to simulate the full-scale experiment (stage 3). Note that the model developed by KAERI has only been used to simulate the Lasgit test (stage 3), since they joined the task in November 2021. All these numerical approaches are based on the general theory of multi-phase flow modelling and are combined with additional properties to describe some of the key features observed in laboratory- and field-tests that distinguish clay-rich media from other rock-types (e.g., deformation of the porous media, creation of dilatant preferential pathways which open and eventually self-seal). Indeed, in them, the bentonite sample is modelled as a deformable porous medium that behaves as an elastic (LBNL, CIMNE-UPC/Andra), an elasto-plastic (BGR/UFZ) or a damaged (KAERI) solid. Intrinsic permeability is treated as a function of other properties during the gas injection test, representing the dilatant pathways. In particular, intrinsic permeability is assumed to depend either on the strain tensor (BGR/UFZ), on the effective minimum compressive stress (LBNL) on the embedded fractures aperture and spacing (CIMNE-UPC/Andra) or on a damage parameter (KAERI). The water retention curve is also assumed to be a function of embedded fractures aperture and spacing in the model developed by CIMNE-UPC/Andra.

A more detailed description of these models is provided in the following section.

3.1 Enriched multi-phase flow models

3.1.1 Model developed by BGR/UFZ

Conceptual model

Model derived for the laboratory-scale test

The model expands upon the work performed by BGR/UFZ within the Task A DECOVALEX-2019 (D-2019), where the team developed a hydro-mechanical model for migration of gas through a low-permeable linear elastic geomaterial that included a pressure-dependent intrinsic permeability. Indeed, for the current phase of DECOVALEX-2023, BGR/UFZ developed a fully coupled, hydro-mechanical model based on multi-phase flow theory, whose key features are:

- Constitutive relations for the hydraulic behaviour: the Mualem model is adopted for the description of the relative permeabilities of gas and water whereas the relationship between water saturation and capillary pressure is based on the van Genuchten formulation, see van Genuchten (1980).

- Constitutive relations for the mechanical behaviour: bentonite is assumed to behave as an elasto-plastic porous medium. Hooke's law is assumed to describe the stress-strain relationship in the elastic regime of the material whereas the Drucker-Prager failure criterion is assumed to describe the plastic deformation (perfect plasticity with non-associated flow). This is enhanced with a tension cut-off parameter to limit the load carrying capacity of the model near the tensile region.

- Hydro-mechanical coupling: Biot's theory (Biot and Willis 1957) is assumed to describe the hydro-mechanical coupling. That is, the effective stress tensor $\boldsymbol{\sigma}'$ (Pa) is calculated from the pore pressure $\mathbf{p}$ and the total stress tensor $\boldsymbol{\sigma}$ as

$$\boldsymbol{\sigma}' = \boldsymbol{\sigma} - \alpha \mathbf{p} \tag{1}$$

(where α (-) is the Biot's coefficient) and used to define the linear momentum balance equation of the porous medium

$$\nabla\left[\boldsymbol{\sigma}' + \alpha\left(p_g - S_w p_c\right)\mathbf{I}\right] + \rho\boldsymbol{g} = 0 \tag{2}$$

where p_g (Pa) is the gas pressure, S_w (-) is the water saturation, p_c (Pa) is the capillary pressure, $\mathbf{I}$ is the identity tensor, ρ (kg/m³) is the total density and $\boldsymbol{g}$ (m/s²) is the gravitational acceleration.

Material heterogeneity is included in the model via the gas entry pressure and Young's modulus, which are described with a heterogeneous distribution. Both can be derived from a non-uniform distribution of the dry density, which has been observed in similar experiments (Villar et al. 2020). The approach does not attempt to represent the scale of the microstructure in finite elements. Rather, it tries to simulate a statistical reproduction of measured value ranges by means of variance and mean value. Since there is not a detailed analysis of the dry density of the bentonite sample, measured stresses and pressures are used for the implementation of the heterogeneity. The variance of the Young's modulus is derived from the stress measurements and the gas entry pressure is derived from the observed gas entry into the bentonite. The stress measurements at the beginning of the experiment (Figure 3) are approximately between 7 MPa and 8.5 MPa. Assuming a linear relationship between measured stress and Young's modulus, a standard deviation of 0.27 GPa can be calculated. The mean value for the Young's modulus is 3.5 GPa. A Gaussian normal distribution is assumed for

the distribution. For the distribution of the gas entry pressures, the measured gas pressures are analysed at which gas first enters the bentonite and at which the main part of gas enters. The first inflow is measured at a gas pressure of 7.3 MPa, while the main inflow occurs at 9.8 MPa (Figure 7). From this, a mean value for the gas entry pressure of approx. 10 MPa and a standard deviation of 2 MPa are determined.

Dilatant pathways are modelled by including the strain-dependent intrinsic permeability relationship developed by Xu et al. (2011)

$$\mathbf{k} = f(\varepsilon_{vol})e^{b_1\bar{\varepsilon}^p}\mathbf{k}_0 \tag{3}$$

where

$$f(\varepsilon_{vol}) = \begin{cases} 10^{b_2\varepsilon_{vol}}, & \varepsilon_{vol} \geq 0 \text{ (compaction)} \\ 10^{b_3\varepsilon_{vol}}, & \varepsilon_{vol} < 0 \text{ (extension)} \end{cases} \tag{4}$$

with ε_{vol} (-) being the volumetric strain, $\bar{\varepsilon}^p$ (-) being the equivalent plastic strain, $\mathbf{k}_0$ (= 5×10^{-20} m^2) being the initial intrinsic permeability tensor and b_1, b_2 and b_3 being empirical parameters controlling flow that need to be calibrated against experimental results. In particular, parameters b_2 and b_3 account for the increased flow velocities in the case of microfissuring, which might be observed when the gas pressure is still lower than the minimum principal stress and tensile strength whereas b_1 is used to define a rapid increase of permeability once the tensile failure is reached. The volumetric strain is 0 at the beginning of the simulation. Maximum permeability increments triggered by volumetric strain and plastic strain are at a factor of 100 each. That is, a theoretical increase in intrinsic permeability of 10,000 can occur at high volumetric and plastic deformations. However, it should be noted that the model is only suitable for models with small plastic deformations. However, it should be noted that the model is only validated for small plastic deformations and only small deformations can be realistically calculated with the implementation of the finite element method used here. The prescription of their values is difficult and the sensitivity analysis performed to simulate the test will be discussed in the section 4. The higher permeability paths are triggered by the heterogeneous distribution of Young's modulus, which is expected to result in a non-uniform strain development. Its mean needs also to be empirically calibrated and details about the sensitivity analysis performed to simulate the test are also reported in section 4.

Main conceptual modifications: from the laboratory- to the field-scale model

No significant conceptual changes were made to the previous model when simulating the full-scale test.

The main modification was to consider that the bentonite is actually composed of three different materials: (1) the pre-compacted bentonite blocks, (2) the swollen bentonite and (3) the interfaces between the bentonite blocks, as described below. These three different regions were described by means of different properties (e.g., different dry densities, gas entry pressures and tensile strengths), thus enabling the description of flow paths. Hence, heterogeneity via the Young's modulus, which was used in the laboratory-scale exercise to represent flow paths, plays here a minor role, as the parametric differences between these three materials are much more significant.

The second conceptual adjustment refers to the technique to incorporate heterogeneity into the model. Although, as said, in the Lasgit modelling exercise, the formation of preferential pathways is less affected by the heterogeneous spatial distributions, the technique to derive heterogeneous Young's modulus values was also modified in order to represent micro-structures. Indeed, when simulating the laboratory-scale test, a Gaussian normal distribution was assumed to derive the spatial distributions. Instead, in the full-scale modelling exercise, the pore size density (PSD) functions of comparable materials (MX-80 bentonite) were used to identify the dominant pore modes and also to analyse the porosity and void ratio in the structure (Seiphoori, 2015). This was done by using the Young-Laplace equation (Delage and Lefebvre, 1984), which allows the description of the capillary pressure as a function of the pore throat width/radius via the relationship

$$p_{\mathrm{c}} = \frac{2T_{\mathrm{s}}\cos(\theta)}{a} \tag{5}$$

where T_s (=0.072 N/m) is the surface tension of the wetting fluid, θ is the angle between the wetting fluid and the solid phase and a is the radius of the pore throat. Assuming then a constant state of quasi-full saturation $\left(\theta = 0°, p_{\mathrm{c}} = \frac{2T_{\mathrm{s}}}{a}\right)$ and taking into account that the gas entry pressure corresponds to the gas pressure that must be applied for the gas phase to enter the pore space ($p_{\mathrm{entry}} = p_{\mathrm{gas}}$), Eq. (5) leads to

$$p_{\mathrm{entry}} = p_{\mathrm{gas}} = p_{\mathrm{c}} + p_{\mathrm{w}} = \frac{2T_{\mathrm{s}}}{a} + p_{\mathrm{w}} \tag{6}$$

thus showing that the gas entry pressure depends on the radius of the pore throat and the water pressure. Then, using the PSD of the fully saturated compacted bentonite (Figure 19A), relative proportions of pore sizes can be estimated and the probability density of gas entry pressure (Figure 19B) and hence, Young's modulus, can be derived.

It is noted that directly linking the pore sizes to water retention is a simplification for swelling clays such as bentonite where the retention characteristics are controlled by a range of physical and chemical processes within and around the clay grains, but pore size was felt to be a useful proxy for these other processes.

The rest of the changes are related to the adjustment of some of the material parameters. Indeed, some of them have been calibrated for the new experiment (e.g., the empirical parameters used to define the strain-dependent permeability model of Eq. (4)) and others (e.g., the friction angle and the cohesion strength) have been defined based on the literature rather than via a calibration process (as was the case for the laboratory-scale experiment), see Appendix A. This is due to the fact that the full-scale test is less constrained than the laboratory-scale experiment and hence, plasticity is thought to play a less significant role.
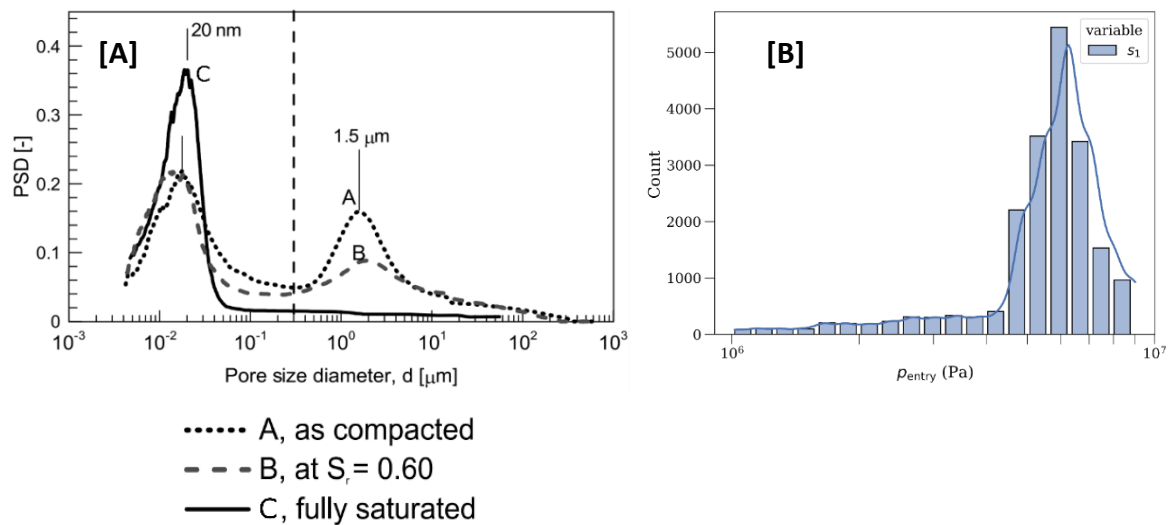
Figure 19. [A] Pore size density in relation to different pore size diameters for three states: compacted but dry (A) with equal amounts of micropores and macropores, compacted and partially saturated (B) with twice as many of micropores than macropores, and compacted and fully saturated state (C) with mainly micropores (edited after Seiphoori (2015)) and [B] Probability density of gas entry pressure in the bentonite materials

Model geometry and numerical software

To simulate both tests, the finite element method (FEM) is employed. The computer software OpenGeoSys (OGS - version 5.8) is used, see Kolditz et al. (2012). OGS has been developed as an open-source initiative since the mid-1980s for numerical simulations of thermal-hydro-mechanical-chemical processes in porous and fractured media.

Laboratory-scale test

A triangular 2D axisymmetric mesh is used to analyse the laboratory-scale test described in Section 2.1, see Figure 20. The injector (assumed rigid) is explicitly modelled by means of the addition of a source term (whose value needs calibration against experimental measurements) that allows the simulation of the increasing pressure. It is defined by a high porosity (= 0.5) and a high permeability value (= 1×10^{-17} m^2). Relatively low values have been chosen here for the injector material, to reduce numerical issues at the boundary between the injector and the bentonite. However, in relation to the bentonite permeability, the intrinsic and relative permeability combined are around 10^{10} higher.
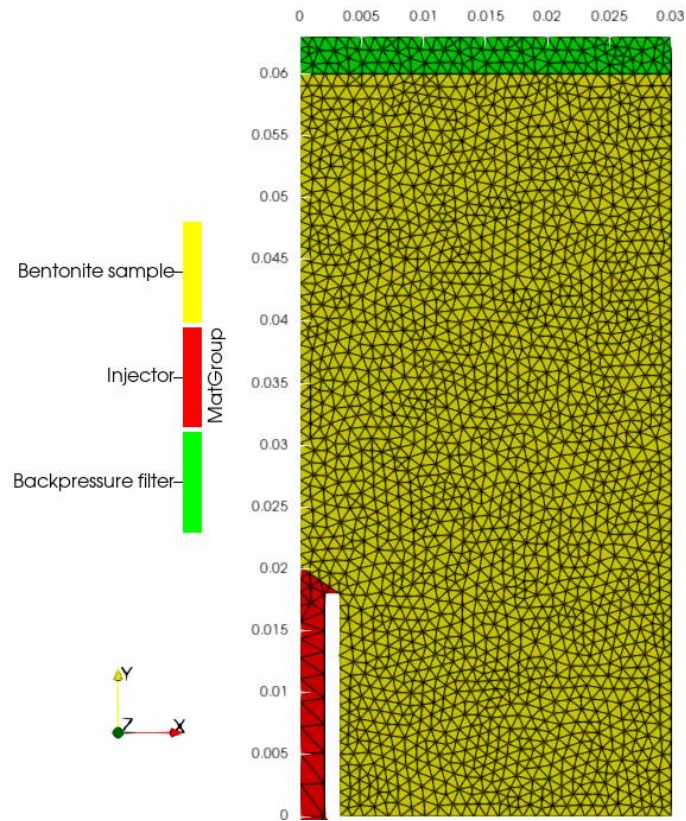
Figure 20. Axisymmetric mesh (with 2716 triangular elements and 1448 nodes) used by BGR/UFZ to simulate the laboratory-scale test.

Field-scale test

A hexahedral mesh of one quarter of the bentonite hollow cylinder is employed, Figure 21[A]. A height of 1.5 m is considered. Six different material groups are assumed, see Figure 21[B]. Three of them are employed to describe the bentonite: (1) the pre-compacted bentonite blocks, (2) the swollen bentonite and (3) the interfaces between the bentonite blocks, whose properties are reported in Appendix A. Four other materials are considered to describe the (4) solid rock, (5) the fractured rock on the outside of the model, (6) the injection filter and (7) the copper wall. Compared to the bentonite, these four materials have a higher Young's modulus (E = 1000 GPa). Different permeability values for each zone are assumed: the rock and copper cylinder have k = 1×10^{-25} m², the fractured rock has k = 1×10^{-18} m² and the injection filter has k = 1×10^{-16} m².

[A]   **[B]**
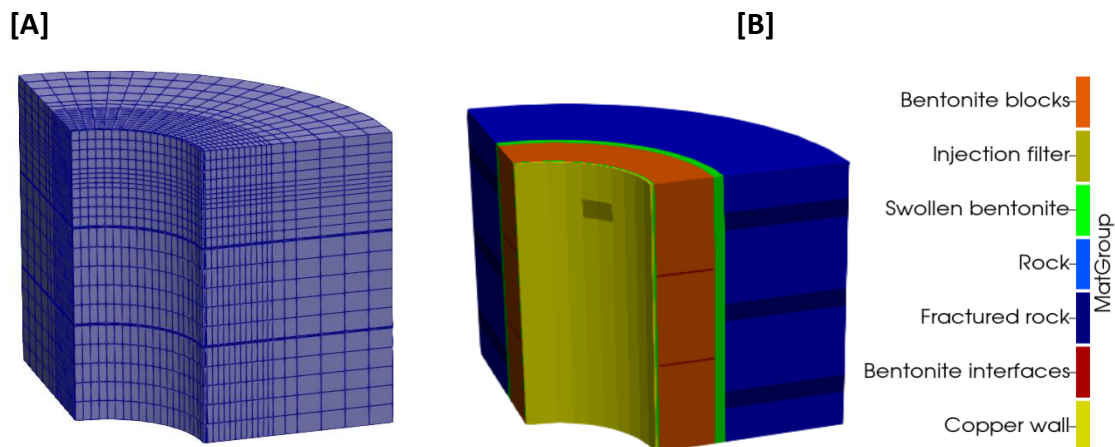
Figure 21 [A] Mesh (with 21840 hexahedron elements and 24354 nodes) used by BGR/UFZ to simulate the Lasgit test and [B] geometry with the six material groups considered.

Initial and boundary conditions

Laboratory-scale test

The sample has been considered to be initially saturated (initial mean saturation of 97%) by assuming an initial capillary pressure of 2.0 MPa. However, due to a relatively large variance in the gas entry pressure, a high variability of gas saturation can be observed in the numerical results. A constant gas pressure of 3.0 MPa has been prescribed to account for a water pressure of 1 MPa (as dictated by the sorption equilibrium equation, see Gray and Hassanizadeh, 1991). An initial compressive effective stress of 7.0 MPa (in each direction) has been defined to account for the swelling stress reached by the material during saturation.

No displacements are prescribed at the boundaries including the central borehole, see Figure 20. Injection pressure is prescribed at the bottom of the injector material group whereas backpressure is prescribed at the upper boundary.

Field-scale test

Prior to the gas injection test, the hydration phase (over the period from day 2100 to day 3100) is simulated, with initial conditions of Table 5. Indeed, the swelling of the

bentonite pellets and blocks is modelled with respect to the change in stress and pressure. To account for swelling pressure in the bentonite, the linear swelling model proposed by Rutqvist et al. (2011)

$$\Delta\boldsymbol{\sigma}_{sw} = \boldsymbol{\sigma}_{sw,max}\Delta S_w\mathbf{I}, \ \forall S_w \in [S_{res}, S_{max}] \quad (7)$$

where $\boldsymbol{\sigma}_{sw,max}$ (Pa) is the maximum swelling pressure, is assumed. This is considered to increase non-linearly with an increase of dry density. In particular, the empirical relationship for MX-80 bentonite

$$\boldsymbol{\sigma}_{sw,max} = 0.01e^{3.85\rho_d} \quad (8)$$

(established by Seiphoori, 2015) is employed.

Table 5. Initial conditions prescribed for the simulation of the hydration phase

	Bentonite (pre-compacted blocks, swollen bentonite and interfaces)	Injection filter	Rock and copper canister wall
Capillary pressure	3 MPa	3 MPa	3 MPa
Effective stresses	σ_{xx} = 3.23 MPa σ_{yy} = 3.23 MPa σ_{zz} = 3.73 MPa	σ_{xx} = 0 MPa σ_{yy} = 0 MPa σ_{zz} = 0 MPa	σ_{xx} = 4.23 MPa σ_{yy} = 4.23 MPa σ_{zz} = 4.73 MPa
Gas pressure	2.4 +1 x 10^5 z MPa	1.85 MPa	2.4 +1 x 10^5 z MPa

During the hydration phase, the capillary pressure is reduced from an initial value of 3 MPa to 0.4 MPa and the mean water saturation is increased from $S_w = 0.9$ to $S_w = 0.998$. Subsequently, the gas injection is applied with a Neumann boundary condition. The following boundary conditions are assumed (see Figure 22):

- Mechanical BC: u_z = 0 at top and bottom, u_x = 0 at the left and at inner and outer boundaries and u_y = 0 at the right and at inner and outer boundaries.
- Hydraulic BC: gas pressure is prescribed at the bottom and at the outer boundaries (p_g = 2 MPa) and capillary pressure is prescribed at the outer boundaries (p_c = 0.4 MPa).
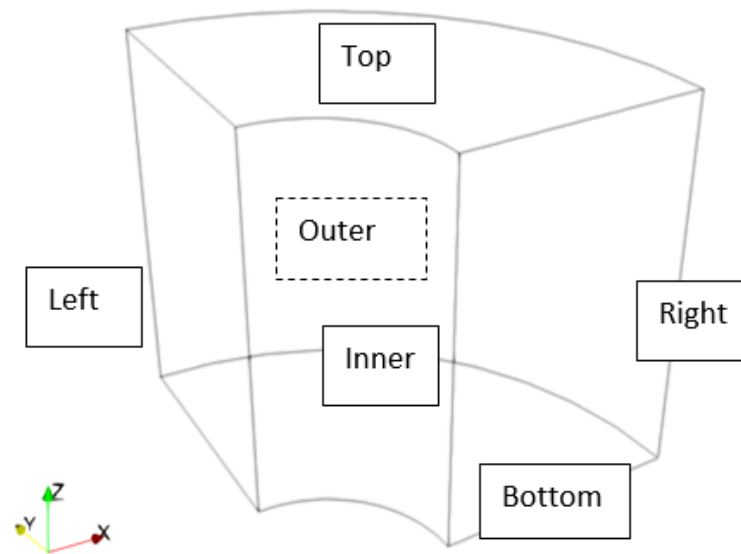
Figure 22. Boundaries for the Lasgit modelling exercise.

3.1.2 Model developed by LBNL

Conceptual model

Model derived for the laboratory-scale test

This model builds upon LBNL's previously experience gained during Task A DECOVALEX-2019 (D-2019) since, as part of D-2019, LBNL developed and numerically applied two different approaches: a multiphase flow model (i) combined with additional hydro-mechanical features and (ii) coupled to a discrete fracture modelling approach, see Kim et al. (2021). Indeed, for the current phase of DECOVALEX-2023, LBNL enhanced their homogeneous continuum approach, which is based on the linking of the multiphase fluid flow simulator TOUGH2 with the commercial FLAC^{3D} geomechanical code thus enabling the simulation of processes characterised by strongly-coupled flow and geomechanics. Key features of this current enhanced continuum approach are:

- Constitutive relations for the hydraulic behaviour: as done by BGR/UFZ, the van Genuchten formulation is used to define the water retention curve. Relevant capillary pressure parameters for the bentonite are adopted from Senger and

Marschall (2008). In this model, the Corey model is adopted for the description of the relative permeabilities of gas and water.

- Constitutive relations for the mechanical behaviour: bentonite is assumed to behave as a linear elastic porous medium, with a volumetric swelling and a swelling stress that depends on the changes in water saturation ΔS_l according to

$$\Delta \boldsymbol{\sigma}'_{\mathrm{sw}} = \mathbf{K} \Delta S_l \beta_{\mathrm{sw}} \tag{9}$$

where $\boldsymbol{\sigma}'_{\mathrm{sw}}$ (Pa) is the swelling stress, $\mathbf{K}$ (Pa) is the bulk modulus, S_l (-) is the liquid saturation and β_{sw} [-] is a calibrated moisture swelling coefficient ($\beta_{\mathrm{sw}} = 0.02$ in D-2019 and decreased up to $\beta_{\mathrm{sw}} = 0.015$ in D-2023 to better match the experimentally-observed stress increase), see Rutqvist et al. (2011) for more details.

- Hydro-mechanical coupling: in this model, the effective stress tensor $\boldsymbol{\sigma}'$ (Pa) responds to the maximum phase pressure p^ϕ in the pore, that can be either gas pressure (if gas partially saturated) or liquid pressure (if fully water saturated). That is,

$$\boldsymbol{\sigma}' = \boldsymbol{\sigma} - p^\phi \mathbf{I} \tag{10}$$

where again, $\boldsymbol{\sigma}'$ and $\boldsymbol{\sigma}$ are the effective and total stress tensors respectively, $\mathbf{I}$ is the identity tensor and the pore pressure p^ϕ is defined as

$$p^\phi = \max(p_l, p_g) \tag{11}$$

with p_l and p_g liquid and gas phase pressures respectively.

As in D-2019, this model assumes a fracture-like behaviour of the flow path. Hence, a pressure dependent permeability function

$$k = k_{\mathrm{matrix}} + \frac{b_h^3}{12a} \tag{12}$$

is again considered, where a [m] is the element width and b_h [m] is a non-linear function of the effective minimum compressive stress that reads

$$b_h = \frac{b_{h0}}{1 + 9\left(\frac{\sigma_n - P}{\sigma_{n,\mathrm{ref}}}\right)} \tag{13}$$

with b_{h0} (m) being the (calibrated) maximum aperture for permeability, σ_n (Pa) the total stress normal to the fracture and $\sigma_{n,\mathrm{ref}}$ (Pa) the adjusted reference stress normal to the fracture. The aperture versus pressure relationship of Eq. (13) corresponds to the Bandis et al. (1983) model and its parameters need to be calibrated by matching pressure and outflow responses observed in the experiments, see section 4 for more details. To be able to simulate the abrupt gas breakthrough response, the concept of a constant

effective gas entry pressure has been adopted by LBNL. As done by BGR/UFZ, a heterogeneous gas entry pressure might be considered in future approaches, together with heterogeneous porosity and permeability fields.

Main conceptual modifications: from the laboratory- to the field-scale model

As in the case of BGR/UFZ (section 3.1.1), no conceptual changes were added to the previous model when simulating the full-scale test.

Due to the fact that, experimentally, gas flows along interfaces, and as done also by BGR/UFZ, LBNL's main modification was to include interfaces between (1) bentonite blocks, (2) the canister and the bentonite and (3) the rock and the bentonite. The conceptual model described in the above section is also used to describe the behaviour of these interfaces, but with different material properties. Indeed, interfaces are represented with a lower gas entry pressure (simulated with the residual gas saturation, S_{gr}) and a higher permeability value.

A second conceptual adjustment was applied to improve the post-peak pressure behaviour. This consisted of scaling the capillary pressure to account for the permeability change due to the opening of a flow path. Indeed, assuming that dilatant flow paths can be represented as fracture-like elements, the capillary pressure of these elements is scaled according to Olivella and Alonso (2008) by the function of permeability as

$$P'_0 = P_0 \left(\frac{k_0}{k} \right)^{1/3} \tag{14}$$

where P_0 is the initial van-Genuchten capillary pressure, P'_0 is the corrected capillary pressure, k is the permeability and k_0 is the initial permeability.

Model geometry and numerical software

The simulator applied in this study is the TOUGH-FLAC code (Rutqvist et al., 2002; Rutqvist 2011; 2017), that combines the TOUGH2 multiphase flow simulator (Pruess et al., 2012) with the commercial geomechanics code FLAC3D (Itasca, 2018). TOUGH2 enables the simulation of multiphase fluid flow and heat transport based on the integral finite difference method whereas FLAC3D is a finite-difference code that allows the representation of geomechanical features. Similar to other TOUGH-based geomechanical simulators, the two codes are sequentially coupled: in particular, fluid

flow variables (such as pore pressure and saturation) calculated by TOUGH2 are transferred to FLAC3D, which then computes effective stresses and associated deformations, returning updated values for the stress-dependent permeability. The selection of small time-steps is important to find stable solutions of the hydraulic and mechanical response: a maximum time step of 1 day is here prescribed while smaller time-steps (e.g., 100 seconds) are automatically calculated by TOUGH2 for convergence in the multiphase flow calculations around the gas breakthrough. This is the main computational challenge that arose when running simulations: during abrupt changes in saturation and permeability (at the instant of gas breakthrough) time steps were reduced to very small values for convergence in the sequentially coupled hydro-mechanical solution process.

Laboratory-scale test

To simulate the laboratory-scale test, a quadrilateral 2D axisymmetric mesh has been used, see Figure 23. The use of an axisymmetric model allows to obtain simulation results within a reasonable time (on the order of 20 min) by employing relatively small number of elements and nodes, see Appendix A.3. However, it is inherently limited to the analysis with homogeneous material properties, thus meaning that heterogeneous properties and flow paths cannot be rigorously considered. To properly consider heterogeneous material properties, a full 3D model would be required. As seen, the injector is explicitly modelled considering a representative volume of the injection chamber. For the simulations (see section 4), gas is injected by prescribing its injection rate (in kg/s). This value needs to be calibrated by fitting the pressure increment in the injection chamber against the observed pressure increments.
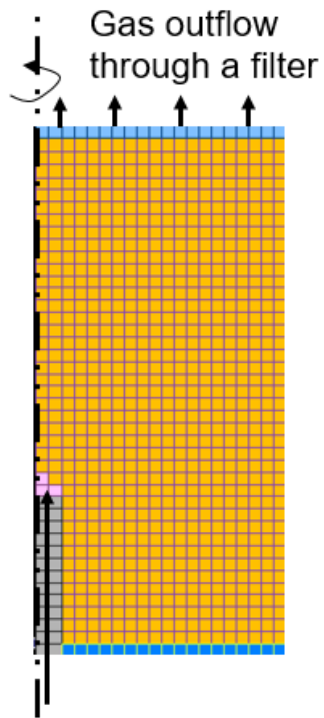
Figure 23. Axisymmetric mesh (with 857 elements, including element representing the injection filter and the injection chamber) used by LBNL to simulate the laboratory-scale test.

Field-scale test

To simulate the full-scale test, a 3D symmetric model has been used, see Figure 24. As already commented, interfaces between (1) bentonite blocks, (2) the canister and the bentonite and (3) the rock and the bentonite are considered.
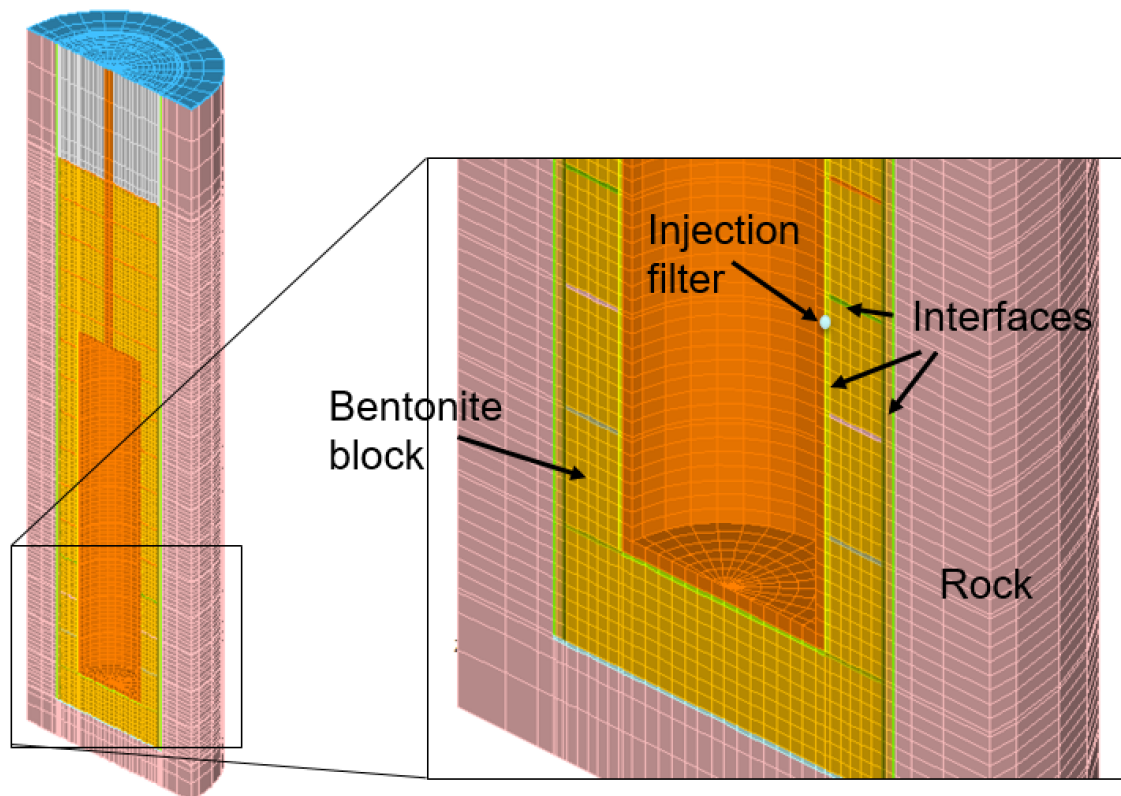
Figure 24. Half-symmetric 3D model used to describe the Lasgit experiment. The model has 37,107 elements.

Initial and boundary conditions

Laboratory-scale test

The sample and the injection chamber have been considered to be fully initially saturated (2 MPa water pressure). A backpressure of 1 MPa has been also assumed and an initial stress of 8.0 MPa has been defined. The sample is mechanically confined during the entire simulation: no displacements normal to the boundaries are prescribed. A no-flow condition has been assumed at the boundaries, except at the injection and outflow filters.

Field-scale test

The sample was initially assumed to be fully saturated with bentonite having a constant initial pressure of 0.8 MPa and rock having a constant initial pressure of 2 MPa. The initial stress conditions were considered as 5 MPa in the radial and tangential directions

and 6 MPa in the vertical direction. Initial temperature is supposed to be 15 ℃ and the initial pressure of the injector is 1868 kPa.

Regarding the boundary conditions, displacements normal to boundaries are fixed to zero and gas injection is only applied in one element of the canister mesh, which is connected to the bentonite. This injection element was initially filled with gas at a pressure of 1868 kPa. Water was then injected into the gas filled injection element to compress the gas and raise the pressure according to the steps shown in the field. Due to the fact that only one half of the 3D geometry is modelled, only one half of the injection filter and the injection rate is simulated. The volume of the element was calibrated in order to achieve a good match with the field data. The calibrated volume was 2000 ml, thus meaning that the total injector volume (for the whole 3D specimen) was calibrated to be 4000 ml, a slightly larger value than the quoted 3750 ml gas injection volume reported from the field.

3.1.3 Model developed by CIMNE-UPC/Andra

Conceptual model

Model derived for the laboratory-scale test

This model is built on the work carried out by CIMNE-UPC/Andra within the previous phase of the DECOVALEX project, see Damians et al. (2020), where a coupled hydro-gas-mechanical 3D numerical model was developed assuming a heterogeneous initial permeability field and embedded fractures (Olivella and Alonso, 2008). This approach is characterised by the following key features:

- Constitutive relations for the hydraulic behaviour: in the model developed by CIMNE-UPC/Andra, the retention curve is defined by the van Genuchten model. In this case, the retention curve may change with the opening of the embedded fractures as pore size controls the gas entry values, and fractures may represent large pores leading to a reduction of the gas entry value. Relative permeabilities are also assumed to be fracture-dependent to account for preferential paths. This is achieved by assuming that the relative permeability, which is a function of the effective degree of saturation, is decomposed into matrix and fracture terms, as discussed in the following paragraph.

- Constitutive relations for the mechanical behaviour: deformation is modelled assuming elasticity with net stress (fluid pressure as the maximum between gas and liquid). A dilatancy term (ψ angle) is added in the deviatoric component of the volumetric strains

$$\Delta\varepsilon_v = \frac{\Delta p'}{K} - \frac{\Delta q}{3G}\tan\psi \tag{15}$$

$$\Delta\varepsilon_d = \frac{\Delta q}{3G} \tag{16}$$

where p' and q correspond to the net mean stress and deviatoric stress invariants, and K and G to the bulk and shear modulus, respectively (compression positive). As done by LBNL, net mean stress is defined as total stress minus Biot's coefficient times fluid pressure (maximum between gas and liquid pressures).

- Hydro-mechanical coupling: in the proposed approach, it is assumed that the mechanical constitutive model and the permeability model are coupled but independent. That is, the mechanical behaviour is coupled to the hydraulic/gas because the volumetric strains cause changes in permeability, through changes in aperture.

To account for the preferential paths, a constitutive model based on an integrated embedded permeability is employed. The strategy is based on the decomposition of the intrinsic permeability into a matrix and a fracture intrinsic permeability

$$k_{\text{int}} = k_{\text{matrix}} + k_{\text{fracture}} \tag{17}$$

which undergo respective variation with porosity and aperture and read

$$k_{\text{matrix}} = \frac{k_0(1-\phi_0)^2}{\phi_0^3}\frac{\phi^3}{(1-\phi)^2} \tag{18}$$

$$k_{\text{fracture}} = \frac{b^3}{12a} \tag{19}$$

where k_0 (m^2) is the initial permeability (randomly distributed along the material); ϕ_0 (=0.44) is the initial porosity; ϕ (-) is the current porosity value, changing in space and time during the test; a (m) refers to the internal associated width for each fracture (which is equivalent to the assumed spacing between fractures) and b (m) is the aperture of the fractures. This value depends on the strain ε (-) and on the initial strain ε_0 (-) and may be computed as

$$b = b_0 + \langle\varepsilon - \varepsilon_0\rangle a \leq b_{\text{max}} \tag{20}$$

with b_0 (m) and b_{max} (m) being the initial and maximum aperture of the fractures. Liquid- and gas-phase permeabilities are also decomposed into matrix and discontinuities or fractures terms. These read

$$k_{\text{liquid}} = \left(S_{\text{eff, liquid}}\right)^{n_{\text{liquid}}} \left(k_{\text{matrix}} + k_{\text{fractures}}\right) \tag{21}$$

$$k_{\text{gas}} = \left(S_{\text{eff, gas}}\right)^{n_{\text{gas}}^{\text{matrix}}} k_{\text{matrix}} + \left(S_{\text{eff, gas}}\right)^{n_{\text{gas}}^{\text{fractures}}} k_{\text{fractures}} \tag{22}$$

respectively, with $S_{\text{eff, liquid/gas}}$ (-) being the saturation degree for liquid or gas and $n_{\text{liquid/gas}}^{\text{matrix/fractures}}$ (-) a power for each case state (i.e., for liquid or gas state, and for matrix or fractures media). As previously stated, liquid and gas relative permeabilities are defined by the effective saturation degree of liquid and gas respectively. Hence,

$$k_{\text{r,liquid/gas}} = \left(S_{\text{eff, liquid/gas}}\right)^{n_{\text{liquid/gas}}} = \left(\frac{S_{\text{liquid/gas}} - S_{\text{liquid/gas}}^{\text{min}}}{S_{\text{liquid/gas}}^{\text{max}} - S_{\text{liquid/gas}}^{\text{min}}}\right)^{n_{\text{liquid/gas}}} \tag{23}$$

Main conceptual modifications: from the laboratory- to the field-scale model

As in the case of the previous teams (sections 3.2.1 and 3.1.2), no conceptual changes were added to the laboratory-scale model when simulating the full-scale test.

As also seen in other models, the role of the interfaces is a key component in the development of the full-scale model. Therefore, as done by the rest of the teams, CIMNE-UPC/Andra's main modification was to include the effect of the canister-bentonite gap interface. In particular, three different assumptions were first considered: (1) an open gap scenario, where the gap is assumed to have a high permeability; (2) a transitional state scenario, where gap closure due to swelling might take place (with reduced hydraulic properties from bentonite, and affecting about 100 mm thick of the bentonite blocks as a damaged zone assumption); and (3) a closed gap scenario (homogenised state), with homogenised properties from the bentonite blocks, see Figure 25. This final strategy simplified the complexity of the modelling problem, since the swelling effect was assumed to be a static case without considering any mechanical performance, and hence, it was finally adopted for the calculations.

Other modifications with respect to the laboratory-scale exercise are related to the inclusion of additional interfaces and the adjustment of some parameters such as (a) the volume factor of the injection, (b) the description of the heterogeneity and (c) the Biot's coefficient (with values of 0.5 and 0.75), see text below and Appendix A for a detailed description.

a) open gap b) gap closure c) closed gap
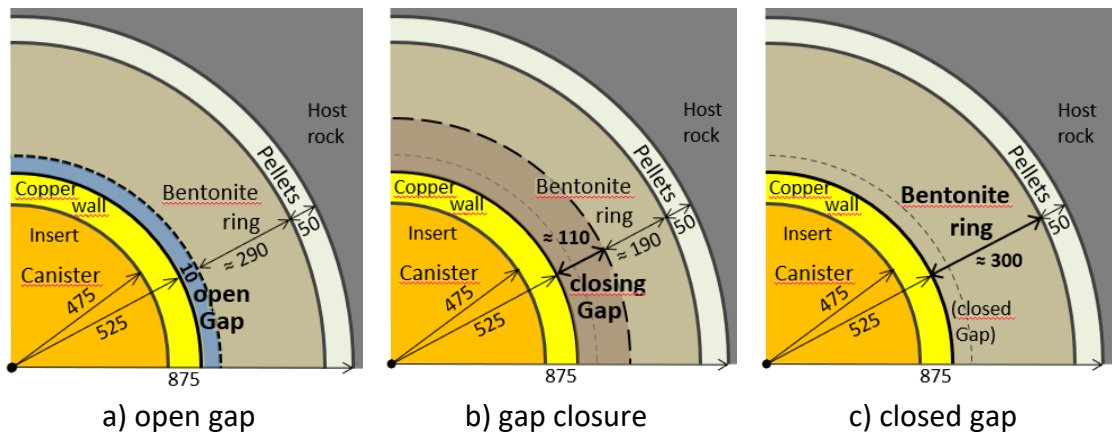
Figure 25. Model geometry: gap closure scenarios: (a) open gap/initial state, (b) transitional gap-closure, and (c) closed gap/homogenized states. (Measurements in mm).

Model geometry and numerical software

Numerical simulations were conducted using the computer software CODE_BRIGHT (Olivella et al., 1996). CODE_BRIGHT is a simulation program based on the finite element method (FEM) that has been developed collaboratively by the Universitat Politècnica de Catalunya·BarcelonaTech (DECA-UPC) and the International Centre for Numerical Methods in Engineering (CIMNE). This software provides the necessary computational tools for accurately analysing and modelling the phenomena under investigation.

Laboratory-scale test

To simulate the blind prediction test, a 3D hexahedral mesh has been employed, see Figure 26. As seen, the 3 mm-thick base (F1 and F2) and backpressure filters have been considered. The injector has been explicitly modelled, assuming all relevant components (i.e., injection rod and injection filter tip), Figure 26(a). Additional global features of the injection/pumping system device (i.e., interface vessel, pipework, etc.) have not been considered but they have been represented through an equivalent volume factor applied to the injection filter. A detailed sensitivity analysis regarding the volume of the injector was performed.

As in previous Task A D-2019, calculations were performed by considering a heterogeneous medium, where three different sample zones have been assumed to be randomly distributed, see Figure 26(b). This produces heterogeneity of permeability and retention curve. It is worth noting that mesh size is always a numerical challenge when modelling hydro-mechanical process and thus, the choice of the mesh involved a

compromise between simplicity on the one hand and the capability of representing heterogeneity on the other.

(a)   (b)
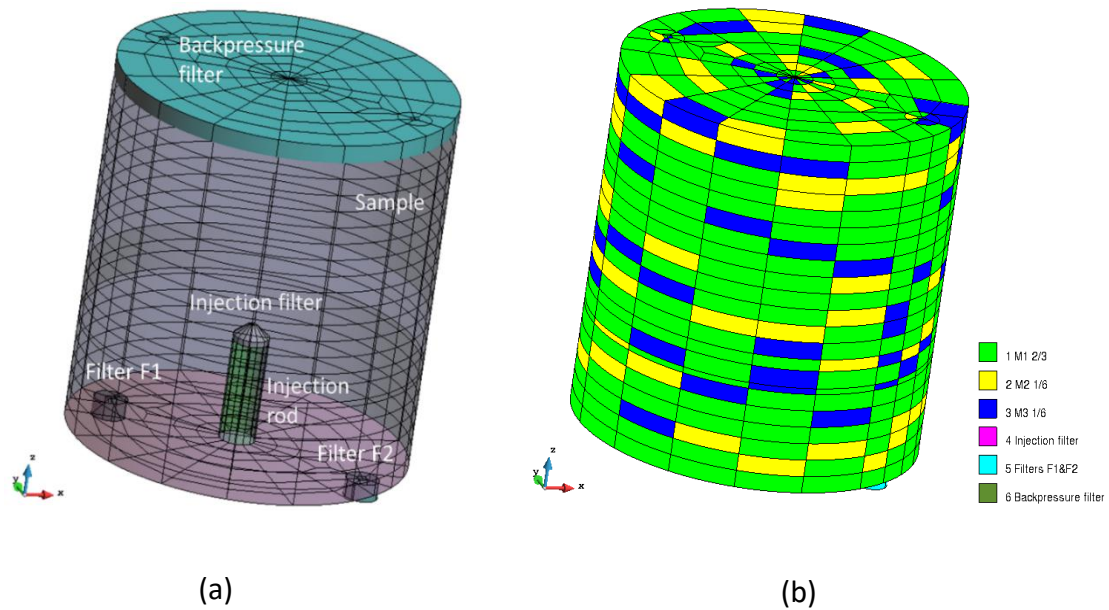
Figure 26. 3D mesh (with 3430 elements and 3909 nodes) used by CIMNE-UPC/Andra to simulate the laboratory-scale test: (a) shows the modelled sample mesh and the main component details and (b) shows the material heterogeneity (2/3–1/6–1/6 weighting).

Field-scale test

To simulate the Lasgit experiment, a three-dimensional FEM model was developed (Sayad Noghretab et al. 2022 and Sayad Noghretab et al. 2023). Initially, a complete model setup was generated, but only a quarter of the model was finally employed for the hydro-gas calculations and calibrations, Figure 27. The FEM mesh consists of 66948 elements, comprising 62794 tetrahedra for the volumes and 4154 triangles for the surfaces. The mesh encompasses a total of 13170 nodes, resulting in 26340 degrees of freedom. The model's geometry encompasses various components, including the coping (consisting of a concrete plug and steel lid), the canister (comprising inner and outer copper walls), bentonite rings and cylinders, and pellets (Figure 28) to depict the entire system's dimensions accurately.

In particular, at the injection section, the FEM mesh was generated with 4538 elements (4380 tetrahedra for the volumes and 158 triangles for surfaces), with a total of 1078 nodes. The model geometry dimensions, including the canister, bentonite rings cylinders, pellets, and filter arrays, were made in agreement with the test specifications provided by the British Geological Survey (Figure 28).
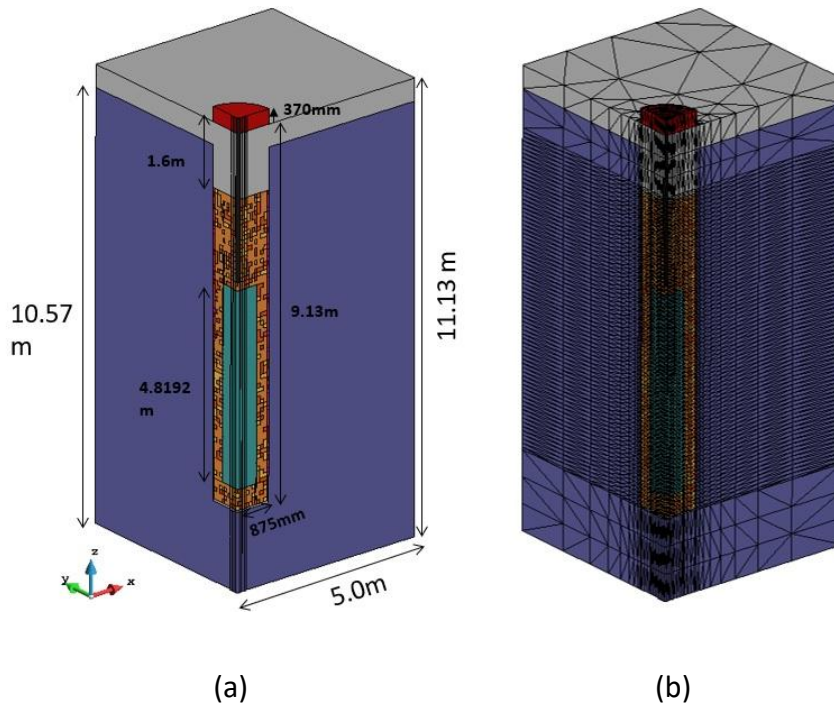
Figure 27. The ¼ model geometry used by CIMNE-UPC/Andra to simulate the full-scale test: (a) shows a general view of the model and (b) shows the mesh (with 66948 tetrahedra and triangle elements with 13170 total nodes).

The model includes additional hydraulic surfaces, which were modelled at the bentonite block contacts (i.e., horizontal interface surfaces) and at the bentonite/pellets and pellets/rock contacts (i.e., vertical interface surfaces), as shown in Figure 29. Although these interfaces exhibited similar properties to the bentonite material, they were considered as separate materials with distinct permeability changes (Table 6) to potentially serve as pathways for gas migration through the buffer.

Filter arrays were also included, represented by external surfaces with a thickness of 1 mm, complemented by a triangular mesh (Figure 30). Flow rates and pressures were prescribed at the outer nodes of these surfaces, and each surface was connected to a single node located on the outer surface of the canister's copper wall, specifically at the Filter Array position. These external surfaces have proven to effectively capture the system volumes associated with pipework, the injection vessel pump, and any additional devices present in the gas injection system before the gas enters the sample. The representation of these components in the model was achieved through the application of an equivalent injection volume factor (a calibrated parameter) to these injection filter surfaces.
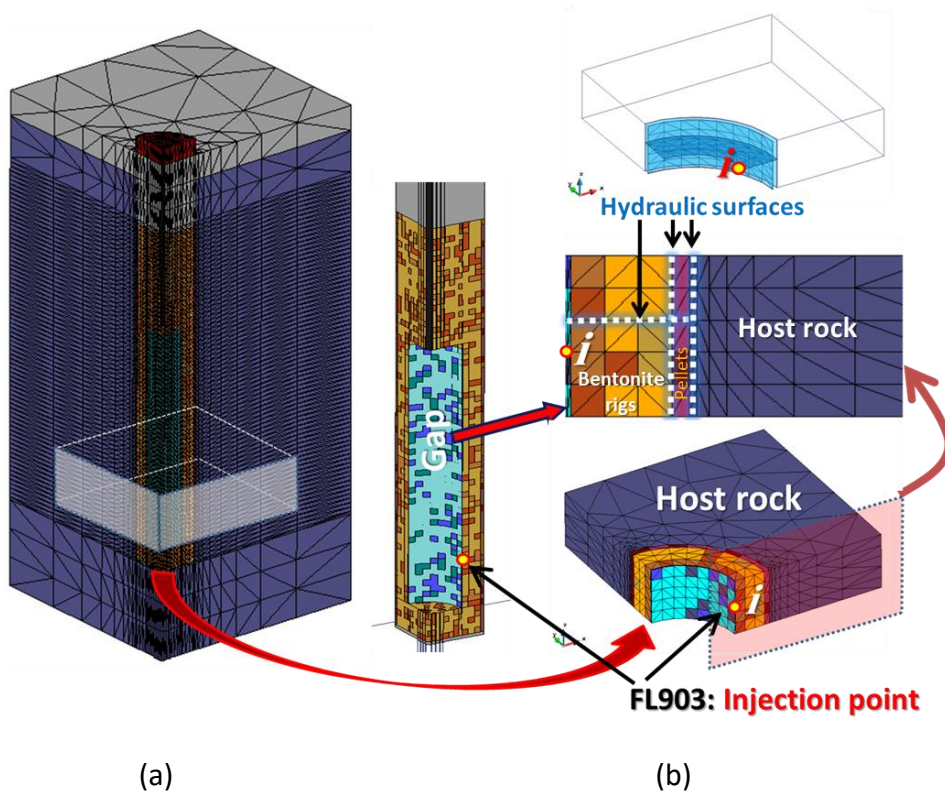
Figure 28. Model geometry and 3D FE models for (a) the 1/4 full-setup and (b) the injection section model.
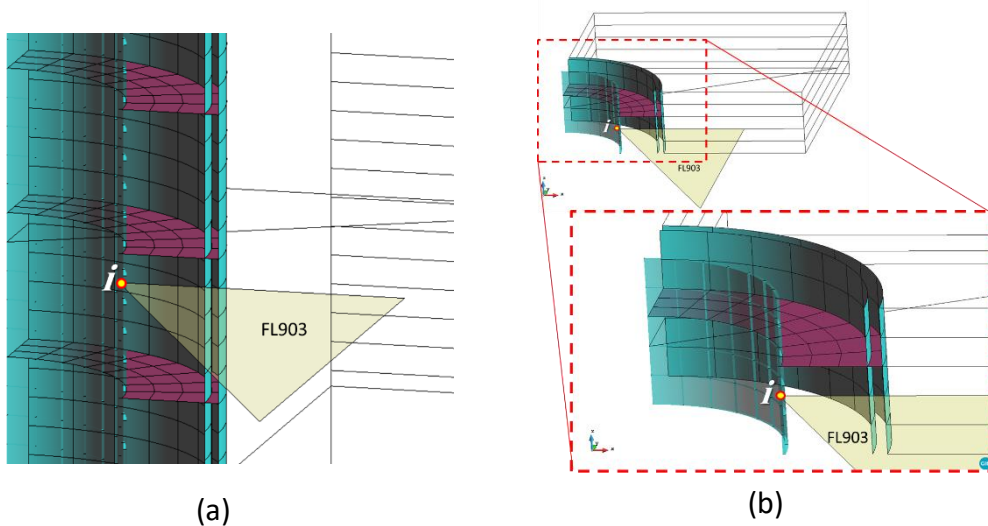
Figure 29. Model geometry of horizontal and vertical interfaces and their position to the injection point (FL903): (a) 1/4 full set-up, (b) injection section model

Table 6. Horizontal, vertical, and horizontal-vertical sensitivity cases on the surfaces between the bentonite blocks (horizontal surfaces) and gap, canister, and bentonite interactions (vertical surfaces).

Materials	Horizontal Intrinsic permeability	Vertical Intrinsic permeability
Horizontal sensitivity cases	1.0×10^{-17} m^2 1.0×10^{-19} m^2	1.0×10^{-20} m^2
Vertical sensitivity cases	1.0×10^{-20} m^2	1.0×10^{-17} m^2 1.0×10^{-19} m^2
Horizontal and vertical sensitivity cases	1.0×10^{-17} m^2 1.0×10^{-19} m^2	1.0×10^{-17} m^2 1.0×10^{-19} m^2
Base Case	1.0×10^{-20} m^2	1.0×10^{-20} m^2
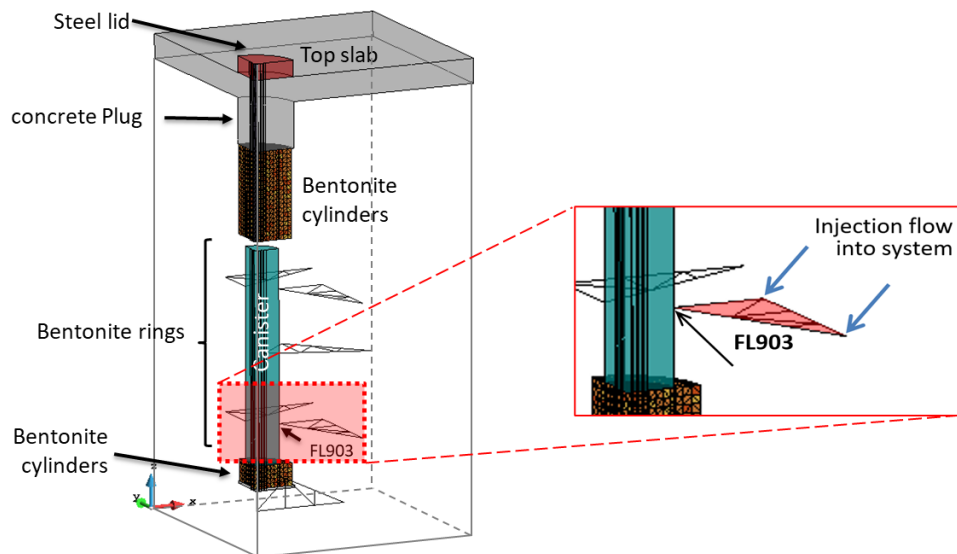
Figure 30. Injection filter details (FL903 filter array location): external volumes to prescribe given injection gas volume-into-system flow rates (external volume equivalent to the system volume).

As done for the laboratory-scale test, a heterogeneous medium was also considered for the full-scale test (Figure 31). In this study, the geometrical domain of the bentonite (rings and cylinders), pellets and gap (that is expected to be filled by the surrounding bentonite after swelling) was divided into small sub-zones to which different initial

properties were assigned. In particular, three different permeability distributions were assumed to follow a probabilistic model, incorporating a layer-by-layer random permeability distribution in three different zones. As a base case scenario, the permeabilities in these zones were weighted with 2/3, 1/6, and 1/6 with values of 1×10^{-21} m^2, 1×10^{-20} m^2, and 1×10^{-19} m^2 respectively. Afterwards, a sensitivity analysis was performed to better understand the impact of different proportions of the heterogeneity distribution on the calculated gas pressure. The impact of this sensitivity on the calculated results was considered small, from a practical point of view.

At the gap layer, intrinsic permeability values varied according to the different states of the gap closure (Figure 25), see Table 7. It is important to note that changes in porosity do not affect the model's predictive capability. Thus, for simplicity, a constant porosity was assumed for the bentonite and pellet materials.
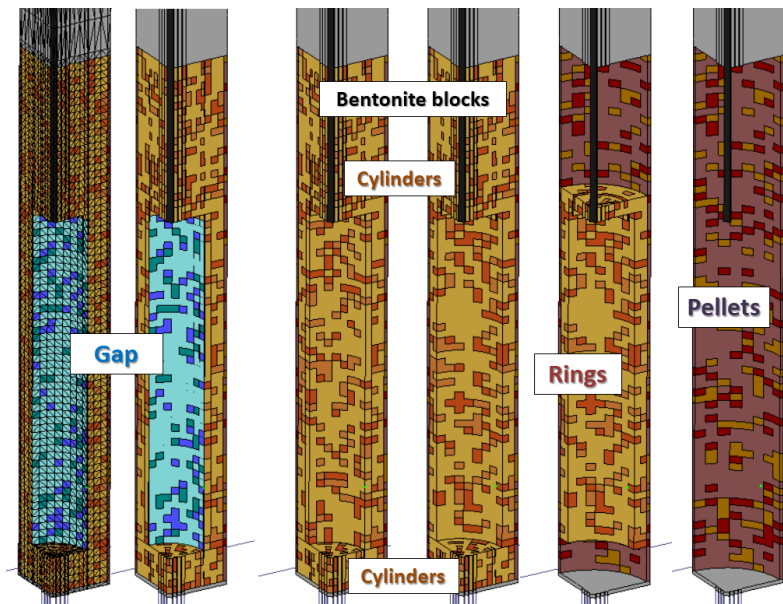
Figure 31. Heterogeneity on permeability randomly distributed to the bentonite blocks (cylinders and rings), pellets, and gap (1/4 full-setup).

Table 7. Heterogeneity on permeability random distribution.

Materials	Distribution (weighting) strategy	Intrinsic permeability	Porosity
Bentonite	1/6 = 16.7%		0.366

Pellets	1/6 = 16.7% 2/3 = 66.7%	1.0×10^{-19} m^2 1.0×10^{-20} m^2 1.0×10^{-21} m^2	0.706
Gap	1/6 = 16.7% 1/6 = 16.7% 2/3 = 66.7%	Variable Intrinsic permeability and porosity (According to Gap closure states: open – transitional – closed scenarios)	

Initial and boundary conditions

Laboratory-scale test

The sample was considered to be initially water saturated. First, no initial stress was considered. After the experimental dataset was released, an initial stress of 8 MPa was prescribed, corresponding to the swelling stress reached by the material during saturation. Boundary conditions reflecting the constant volume boundary test features were assumed. All sample contours were assumed with full prescribed displacement conditions with no displacements allowance in any direction (this also includes the sample-injection rod and filter contact). Once experimental results were released, refined boundary conditions (a refined injected gas flow ramp) were considered thus improving the numerical curves.

Field-scale test

The sample was initially assumed to be water-saturated with a constant pore pressure of 0.1 MPa. Furthermore, the gas pressure and liquid pressure at the external surfaces, which simulate the injected gas volume, were set equal to 0.1 MPa. The initial stress conditions were considered as 10.5 MPa in the horizontal directions (x and y) and 5.25 MPa in the vertical direction. The boundary conditions were carefully selected to align with the specified Lasgit set-up, specifically through the use of the Filter array FL903. These assumptions and boundary conditions were crucial in accurately capturing the behaviour of the gas test and ensuring the model's alignment with the experimental setup.

3.1.4 Model developed by KAERI

Conceptual model

Model derived for the full-scale test

This model is built on the work carried out by KAERI within the previous phase of the DECOVALEX project, see Lee et al. (2019, 2020), where the team developed a hydro-mechanical model for migration of gas through a low-permeable material that included a damage model to account for the deterioration of the rock after gas breakthrough. Indeed, for the current phase of DECOVALEX-2023, KAERI developed a hydro-mechanical model based on standard multi-phase flow theory, whose key features are:

- Constitutive relations for the hydraulic behaviour: the classical multi-phase Darcy law is solved with a mass balance equation for each component (water and gas phases), assuming constant temperature.
- Constitutive relations for the mechanical behaviour: the classical two-phase flow model is coupled to the elastic damage model proposed by Tang et al (2002). According to this model, the host rock is assumed to be brittle-elastic. That is, the stress-strain relationship is divided into an elastic phase (where no damage or irreversible damages occur) and a damage phase, that accounts for the deterioration of the rock (decrease of strength, rigidity and toughness, for instance). The effective stress tensor $\boldsymbol{\sigma}'$ (Pa) is thus defined as

$$
\begin{aligned}
\text{Before gas breakthrough (elastic model): } \boldsymbol{\sigma}' &= \mathbf{C}:\boldsymbol{\varepsilon} \\
\text{After gas breakthrough (damage model): } \boldsymbol{\sigma}' &= (1-D)\mathbf{C}:\boldsymbol{\varepsilon}
\end{aligned} \tag{24}
$$

where $\boldsymbol{\varepsilon}$ (-) is the infinitesimal strain tensor, $\mathbf{C}$ (Pa) is the fourth-order stiffness tensor, D (-) is the damage parameter and $:$ is the double tensor contraction.

As seen in Equation 24, the elastic modulus of the rock progressively degrades as damage grows. In fact, only damage under tensile stress was considered and hence, damage induced by the compressive stress was not included into the model. Hence, when the tensile stress in an element reaches its tensile strength, the damage variable

$$
D = \begin{cases} 0 & \varepsilon \leq \varepsilon_{t_o} \\ 1 - \dfrac{f_{tr}}{E_0 \varepsilon} & \varepsilon_{t_o} \leq \varepsilon \leq \varepsilon_{t_u} \\ 1 & \varepsilon_{t_u} \leq \varepsilon \end{cases} \tag{25}
$$

is used, where f_{tr} (Pa) stands for the residual tensile strength, E_0 (Pa) is the initial (or undamaged) elastic modulus, ε (-) is the principal strain and ε_{t_o} (-), ε_{t_u} (-) are tensile strain limits.

- Hydro-mechanical coupling: standard Biot's theory is assumed to describe the hydro-mechanical coupling with

$$\boldsymbol{\sigma}' = \boldsymbol{\sigma} - \alpha\bar{p}\mathbf{I} \tag{26}$$

and

$$\bar{p} = S_g p_g + S_w p_w \tag{27}$$

This is used to define the linear momentum balance equation of the porous medium

$$\nabla(\boldsymbol{\sigma} - \alpha\bar{p}\mathbf{I}) + \rho\boldsymbol{g} = 0 \tag{28}$$

Dilatant pathways are modelled by including a damaged-dependent intrinsic permeability field, where

$$\mathrm{k_{int}} = \mathrm{k_{int,undamaged}} + \mathrm{k_{int,damaged}} \tag{29}$$

and

$$\mathrm{k_{int,undamaged}} = \mathrm{k_{int,0}}e^{A\left(\frac{\phi}{\phi_0}-1\right)} \tag{30}$$

$$\mathrm{k_{int,damaged}} = \frac{D}{D_{\mathrm{kmax}}}\left(\mathrm{k_{max}} - \mathrm{k_{int,undamaged}}\right) \tag{31}$$

being $\mathrm{k_{int,0}}$ (m²) the initial intrinsic permeability, A (-) an empirical factor calibrated from the experimental tests, $\mathrm{k_{max}}$ (m²) the experimental maximum permeability of the damaged sedimentary rock and D_{kmax} (-) the experimental rock damage value that corresponds to $\mathrm{k_{max}}$.

The two main modifications with respect to the approach employed in the DECOVALEX-2019 phase are (1) the inclusion of the interface between the void and the buffer material and (2) the designation of different material properties for each of the different elements that compose the domain under consideration (e.g., void, bentonite, pellets and rock).

Model geometry and numerical software

To simulate the full-scale model, the COMSOL Multiphysics® (see COMSOL, 2018) software was used. Consistent with BGR/UFZ and CIMNE-UPC/Andra, only one quarter of the bentonite cylinder was considered, Figure 32.

(a)   (b)   (c)
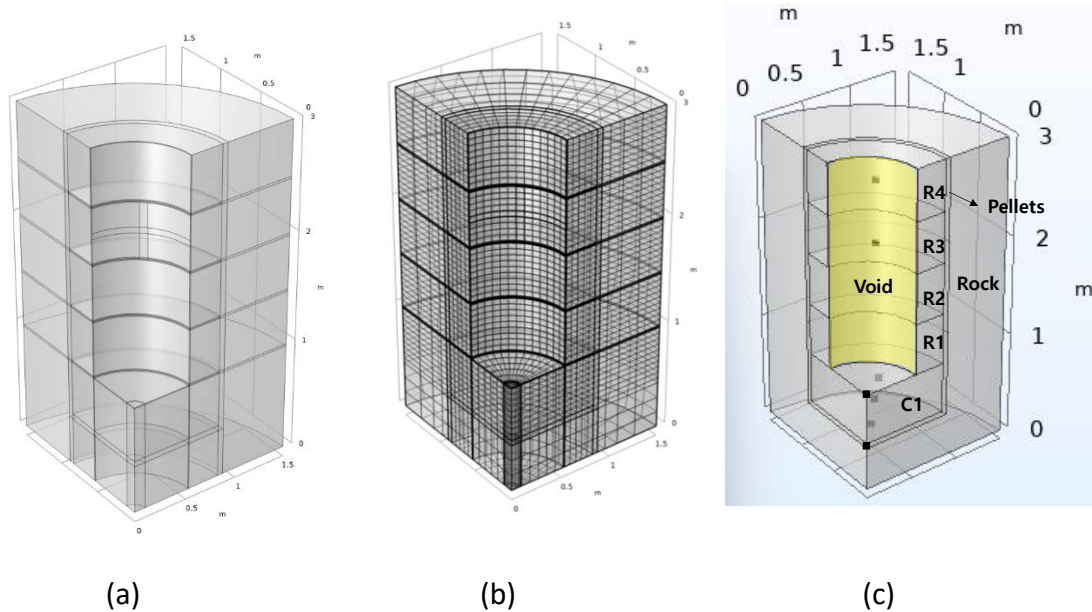
Figure 32. As done by other teams, [a] only a quarter of the bentonite cylinder was considered. In particular, [b] a mesh with 9635 elements (hexahedral and tetrahedral for the cylindrical shapes) and 11067 nodes was used by KAERI, with [c] different materials under consideration.

Initial and boundary conditions

The initial gas pressure was prescribed at 1868 kPa, and the initial water saturation was 0.99. The capillary pressure was calculated using the van Genuchten model and then, the initial water pressure was calculated by the initial gas pressure and capillary pressure. Regarding the mechanical model, the initial total stress tensor is assumed to be diagonal with $\sigma_{xx} = \sigma_{xx} = -5\text{ MPa}$ and $\sigma_{zz} = -6\text{ MPa}$, where the sign minus means compression. Temperature is supposed to be prescribed at 20 °C.

The initial gas pressure was assigned to the outer boundary of the rock components and the injection pressure data over time was applied to the injection area as a Dirichlet

boundary condition. Regarding the mechanical model, a fixed constraint boundary was applied to the bottom surface, and a roller boundary was applied to all boundaries except at the bottom surface.

3.2 Alternative conceptual model developed by SNL

The new conceptual model expands the work performed by Faybishenko et al. (2022) where a phenomenological concept of nonlinear dynamics and deterministic chaos theory was employed to analyse the gas pressure and the gas influx and outflux obtained from a one-dimensional test performed on a water-saturated pre-compacted Mx80 bentonite sample at the British Geological Survey (Figure 33). Indeed, the computation of a set of diagnostic parameters (e.g., global embedding dimension, correlation dimension, information dimension, spectrum of Lyapunov exponents) suggested that the prevailing processes during the gas test are (i) chaotic diffusion both at the onset of gas influx and during the final phase of the experiment and (ii) chaotic advection after the breakthrough. The time series analyses of the data indicate that the observed chaotic behaviour of the system can be described by 3-5 independent variables (Faybishenko et al. 2022). Note that its numerical development is still in a very preliminary phase and it cannot be used yet to reproduce the experiments.

The primary research focus of the SNL team within the current D-2023 project was to understand the actual mechanism(s) for the emergence of the observed complex behaviour of gas migration in water saturated compact bentonite. In particular:

- **Channelling postulate**: although gas migration in a porous medium is generally treated as an immiscible displacement process within a rigid solid framework, this is unlikely to be the case for compacted bentonite, where the pore size is generally extremely small (on a scale of nanometres). Indeed, the capillary pressure p_c in such a medium can be estimated by

$$p_c = \frac{2\gamma\cos(\theta)}{r} \tag{32}$$

where γ (N/m) is the surface tension between gas and water; θ (degrees) is the contact angle water on the solid; and r (m) is the radius of the pore neck. Typical values of these parameters (γ = ~70 mN/m, θ = ~40°, r = 1 - 10 nm, see Wang et al. (2013) and Wang (2014)) lead to a significantly higher p_c (~10 - 100 MPa) than the gas pressure generally used in experiments, see Figure 33. Therefore, the entry of gas into the pores of a compacted bentonite to displace the porewater is unlikely. Instead, the gas injected would tend to compress the bentonite matrix as a whole by expelling the pre-existing pore water surrounding the pathways. Then, the only possible way for gas to move through such media is by channelling, see Figure 34.
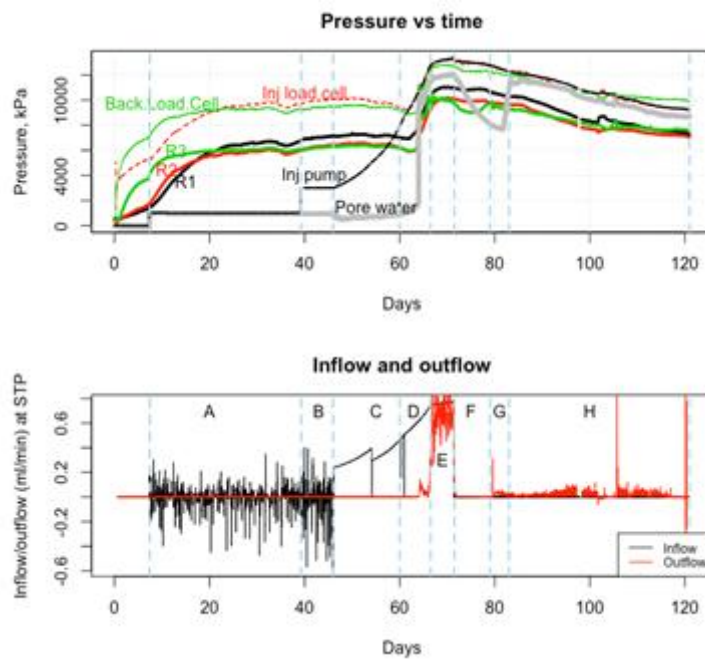
**Figure 33. Time series of gas pressures and fluxes
recorded during the Mx80 gas injection experiment
conducted by the British Geological Survey.**

Channelling can emerge autonomously from the morphological instability of a gas-bentonite interface, Figure 34. This instability can be attributed to two positive feedbacks:

1. As a channel protrudes into the bentonite matrix as an infinitely small perturbation to the gas-bentonite interface, the hydraulic gradient becomes steeper at the tip of the channel, causing more water expulsion from the other side of the bentonite layer and therefore further enhancing channel growth; and

2. as a channel grows, the more tensile stress is created at the tip of the channel, causing local pore dilation and even fracturing at the tip and therefore in turn promoting channel opening.
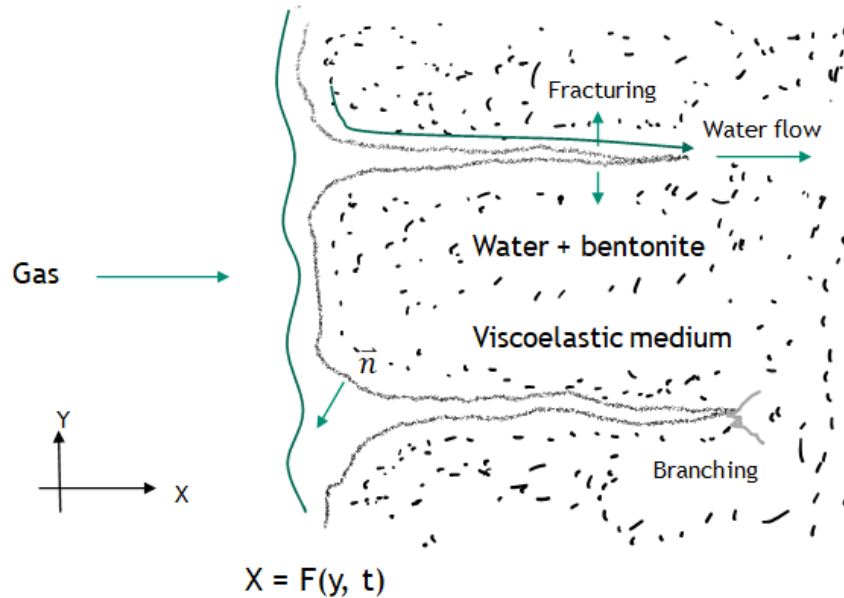
Figure 34. Illustration of gas flow channel development

- **Gas-bentonite interface description (hydrological instability)**: as shown in Figure 34, the problem can be conceptually simplified as a 2D system in which a water saturated bentonite matrix is compressed by the pressurised gas on the left side with porewater expelled from the right side. Due to a low-permeability bentonite matrix, we assume that the compaction of bentonite is limited by the porewater flow and for simplicity, the permeability of the bentonite matrix k is assumed to remain roughly constant during compaction.

The compaction process can then be described by the equation

$$\nabla^2 P = 0 \tag{33}$$

where P is the porewater pressure. At the gas-bentonite interface ($X = F(Y, t)$),

$$P \approx P_g + \gamma_e \frac{\partial^2 F}{\partial Y^2} \tag{34}$$

$$\frac{\partial F}{\partial t} = -k\frac{\partial P}{\partial X} + k\frac{\partial P}{\partial Y}\frac{\partial F}{\partial Y} \tag{35}$$

whereas at the right side ($X = L$),

$$P = P_L \tag{36}$$

where P_g is the gas injection pressure, γ_e is the effective surface tension of the interface between the injected gas and the bentonite matrix, k is the permeability of the bentonite matrix, t is the time and P_L is the porewater pressure at the exit of water flow.

By performing a linear stability analysis of Equations 33 to 36 by imposing infinitely small perturbations to an initially planar gas-bentonite interface, the dispersion equation

$$\zeta = -k\left(\frac{\partial \bar{P}}{\partial X} + \gamma_e m^2\right)m \tag{37}$$

is obtained, which relates the growth rate of perturbation (ζ) to the wave number of the perturbation (m), with $\bar{P}$ being the porewater pressure for the planar solution. Note that $\frac{\partial \bar{P}}{\partial X} < 0$. The growth rate can thus become positive for $m < \sqrt{-\frac{\partial \bar{P}}{\partial X}/\gamma_e}$, implying that the gas-bentonite interface can become morphologically unstable and therefore fingered, leading to the development of gas flow channelling into the bentonite matrix. If the effect of surface tension was ignored, the interface would become unstable with respect to all wave numbers and, in this case, the channel patterns formed would be fractal (Nittmann et al., 1985).

- **Gas-bentonite interface description (mechanical instability)**: during bentonite compaction by gas injection, another interface instability mechanism can potentially come into play. Indeed, at the tip of an interface perturbation, tensile stress at the tip can be increased, resulting in local pore dilation and even fracturing at the tip, and therefore, interface fingering. Initially, after hydrologic compaction, the system is critically stressed. However, at a perturbation tip of a perturbed interface, tensile stress is seen.

Assuming a viscoelastic behaviour for the bentonite matrix, the governing equations

$$\nabla^4 \psi = 0 \tag{38}$$

are derived for the bentonite matrix, where ψ is the Airy stress function. In this case, at the gas-bentonite interface ($X = F(Y, t)$),

$$-\left(P_g - \gamma_e \frac{\partial^2 F}{\partial Y^2}\right) = \frac{\partial^2 \psi}{\partial Y^2} + \frac{\partial F}{\partial Y}\frac{\partial^2 \psi}{\partial X \partial Y} \tag{39}$$

$$-\frac{\partial F}{\partial Y}\frac{\partial^2 \psi}{\partial Y^2} + \frac{\partial^2 \psi}{\partial X \partial Y} + \frac{\partial F}{\partial Y}\frac{\partial^2 \psi}{\partial X^2} = 0 \tag{40}$$

$$\sigma_t = -\frac{\partial F}{\partial Y}\frac{\partial^2 \psi}{\partial X \partial Y} + \frac{\partial^2 \psi}{\partial X^2} \tag{41}$$

$$\frac{\partial F}{\partial t} = \alpha(\sigma_t - \bar{\sigma}_t) \tag{42}$$

and at $X = L$,

$$\frac{\partial^2 \psi}{\partial X^2} = \sigma_{YY}^\infty \tag{43}$$

$$\frac{\partial^2 \psi}{\partial Y^2} = -P_g \tag{44}$$

where σ_t is the normal stress along the tangential direction of the interface, α is the growth rate constant and $\bar{\sigma}_t$ is the σ_t evaluated at the planar interface.

Again, by performing a linear stability analysis of Equations 38 to 44 by imposing infinitely small perturbations on an initially planar gas-bentonite interface, the dispersion equation

$$\zeta = \alpha m \left[2 \left(P_g + \sigma_{YY}^\infty \right) - \gamma_e m \right] \tag{45}$$

is obtained. In this case, the growth rate ζ becomes positive for $m < 2 \left(P_g + \sigma_{YY}^\infty \right) / \gamma_e$, implying that the gas-bentonite interface would become morphologically unstable, leading to the development of gas flow channeling into the bentonite matrix. Again, if the effect of surface tension was negligible, the interface would become unstable with respect to all wave numbers and hence, the channel patterns would be fractal (Nittmann et al., 1985).

- **Crack branching description**: mechanical instability of a gas-bentonite interface can be extended to understand channel branching. In a 2D system, the tip of a channel can be viewed as circular hole internally pressurised by the injected gas, see Figure 35. As before, by performing a linear stability analysis of Equations 38 to 44, written first into a radial coordinate system (r, θ), the dispersion equation

$$\zeta = \frac{2\alpha \left(P_g + \sigma_{rr}^\infty - \frac{\gamma_e}{R} \right) m^2 (m-1) - \frac{2\alpha\gamma_e}{R} (m^2 - 1)^2}{2(m+1)(m-1)} \tag{46}$$

is obtained, where R is the radius of the unperturbed interface. To match the boundary conditions around a circle, m must be a positive integer. Again, the growth rate of perturbation can be positive, implying that the interface can become unstable and thus channel branching can take place. Interestingly, the analysis shows that, to have a proper solution to the perturbed equations, wave number m must be larger than 2. That is, a channel can only branch into three or more channels. However, the stabilising term $\frac{2\alpha\gamma_e}{R} (m^2 - 1)^2$ in Equation 46 increases rapidly with $\sim m^4$. We thus expect that the most likely branching number would be close to three. So far, we have formulated and analysed the

problems for 2-D systems. Physically, the same process would take place in 3-D. However, the related mathematical analyses would be much more complex since in 3-D, a channel developed would look like a tube.
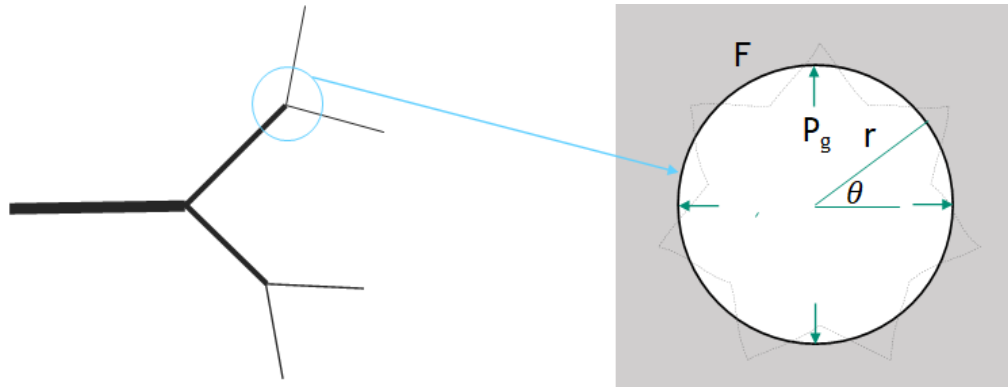
Figure 35. Channel branching through mechanical instability of gas-bentonite interface.

- **Channel deformation postulate**: to understand the channel deformation mechanism, a 2D system in which a flow channel is embedded in a viscoelastic bentonite matrix (Figure 36) is considered.
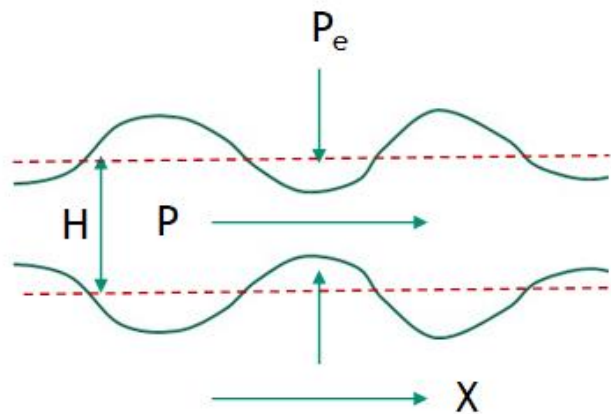
Figure 36. Gas percolation in a deformable channel.

Due to the Bernoulli effect, positive feedback may exist between flow velocity and channel deformation: a local dilation of the channel reduces the flow velocity and therefore increases the fluid pressure, which in turn causes the local channel expansion, leading to the instability of the channel wall. On the other hand, this instability can be countered by the surface tension of the interface. This process can be described by the following dynamic equations:

$$\frac{\partial H}{\partial t} = \frac{\partial}{\partial X}\left(kH^3\frac{\partial P}{\partial X}\right) \tag{47}$$

$$\frac{\partial H}{\partial t} = \lambda\left(\omega H^2 + (P - P_e) - (H - H_e)E + \gamma_e\frac{\partial^2 H}{\partial X^2}\right) \tag{48}$$

where H is the width of the channel, k is the conductivity of the channel, E is the Young's modulus of the bentonite matrix, P_e and H_e are the gas pressure and channel width for an unperturbed case, respectively and λ and ω are adjustable parameters. Terms ωH^2 and $\gamma_e\frac{\partial^2 H}{\partial X^2}$ capture the Bernoulli effect and the surface tension effect, respectively.

As done before, by performing a linear stability analysis of Equations 47 and 48 and by imposing infinitely small perturbations on it, the dispersion equation

$$\zeta = \frac{\lambda k\bar{H}^3 m^2\left(2\omega\bar{H} - E - \gamma_e m^2\right) + 3\lambda k\bar{H}^2\frac{\partial\bar{P}}{\partial X}mi}{\lambda + k\bar{H}^3 m^2} \tag{49}$$

is achieved, where $\bar{H}$ is the the width of the channel for a planar solution

Equation 49 indicates that a positive Re(ζ) can be attained for a large positive $2\omega\bar{H} - E$ value, implying a possible morphological instability of the matrix wall and leading to gas bubble formation within the channel. The nonzero Im(ζ) implies that the chain of bubbles formed can continuously move downstream, see Wang and Budd (2012). This postulated behaviour seems confirmed by the observed periodic or chaotic variations in gas flow rate in other gas injection tests (Figure 37), where each individual spike of flow rate may represent the arrival of a single gas bubble. As shown in Equation 49, as the effect of surface tension vanishes, Re(ζ) becomes positive for all wave numbers. In this case, the size distribution of bubbles within a channel becomes more random, and as a result, gas flow appears more chaotic. On the other hand, if the surface tension term is on the same magnitude as the instability term, the size distribution of gas bubble becomes more regular, resulting in a periodic gas flow rate.
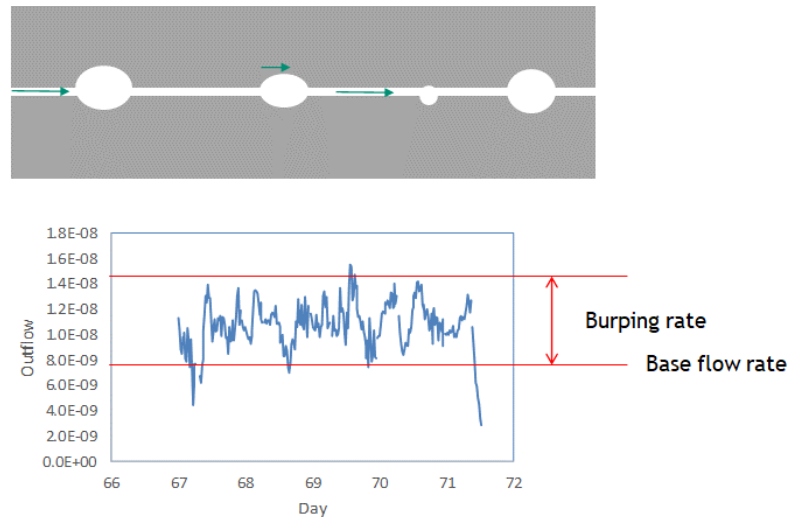
Figure 37. Periodic or chaotic gas flow rate induced by channel wall instability

4 Numerical results

4.1 Laboratory-scale test

The capabilities of three numerical models (BGR/UFZ, LBNL and CIMNE-UPC/Andra) were assessed by comparing the simulated results against the experimental ones obtained from the laboratory. For the sake of comparison, final numerical outcomes (obtained after releasing the laboratory data) are given for brevity.

In particular, the following time histories were specified to be reported and are the key features of the comparison exercise:

1. Radial stresses curves in the 16 sensors (from R1 to R16).
2. Axial stresses in the 8 sensors (from A1 to A8).
3. Pore pressures in the 2 filters (F1 and F2).
4. Gas saturation profiles in the 24 sensors (from R1 to R16 and from A1 to A8).
5. Inflow into the system and outflow curves (at STP).

However, the teams were not asked to explicitly include the behaviour of the sensors used to measure changes in the stress within the bentonite sample. This has no bearing on the validity of the model outputs as sensor deformations were on the micron-scale (orders of magnitude below the models' scales). Some teams did include the representation of the injection system to improve model predictions.

A visual inspection of the experimental data (see Figure 38) indicates that experimental radial and axial stresses can be summarised by four key components: (i) a quiescence phase, followed by (ii) the gas breakthrough, which leads to a (iii) peak value, which is then followed by (iv) a negative decay.
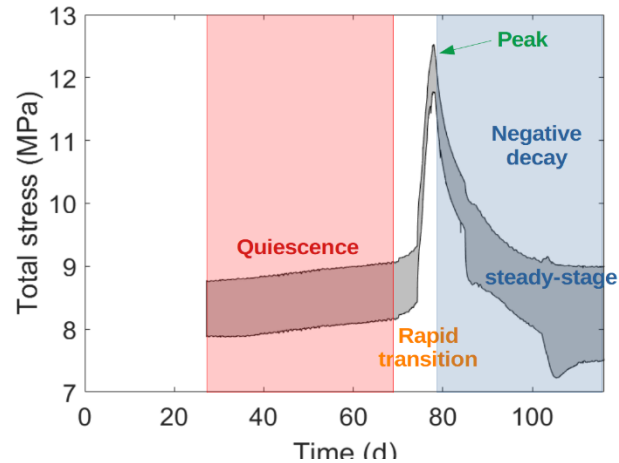
Figure 38. Key components that characterise experimental stresses.

Radial and axial stress results are shown in Figure 39 and Figure 40 respectively. As seen:

- **Quiescence phase**: after releasing the experimental data, all the teams obtain good initial values.
- **Rapid transition**: reasonable responses are obtained after the modelling work performed during the task. However, some models still struggle to predict the rapid evolution of the system. Other key specific features (such as the breakthrough timing) still require a better representation. Indeed, the rapid stress increment is in general earlier modelled than experimentally observed.
- **Peak values**: they are in general reasonably-well captured. Maximum radial stress differences are observed at 48 mm from the base of the sample, where numerical peak values of 12.8 MPa are predicted by both BGR/UFZ and CIMNE-UPC/Andra, whereas experimental values are about 11 MPa (15% overprediction).
- **Negative decay**: models are capable of giving a reasonable representation of the negative decay. Some simulations should have been run for a little longer in order to analyse whether the steady-stage phase is finally captured.

[A]

[B]

[C]

[D]
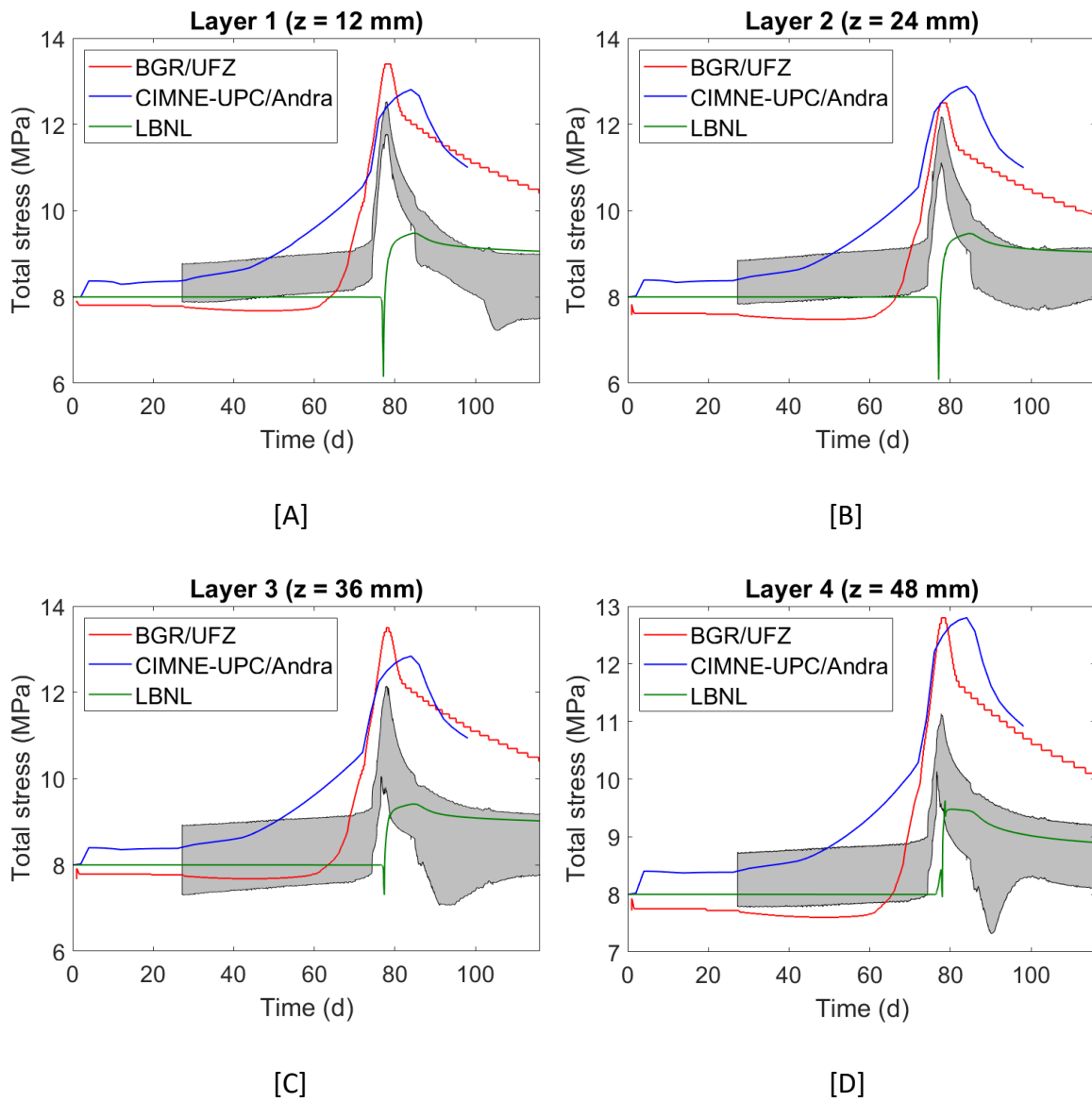
Figure 39. Radial stresses obtained at each layer with the three numerical models. Grey zones represent experimental radial stresses.
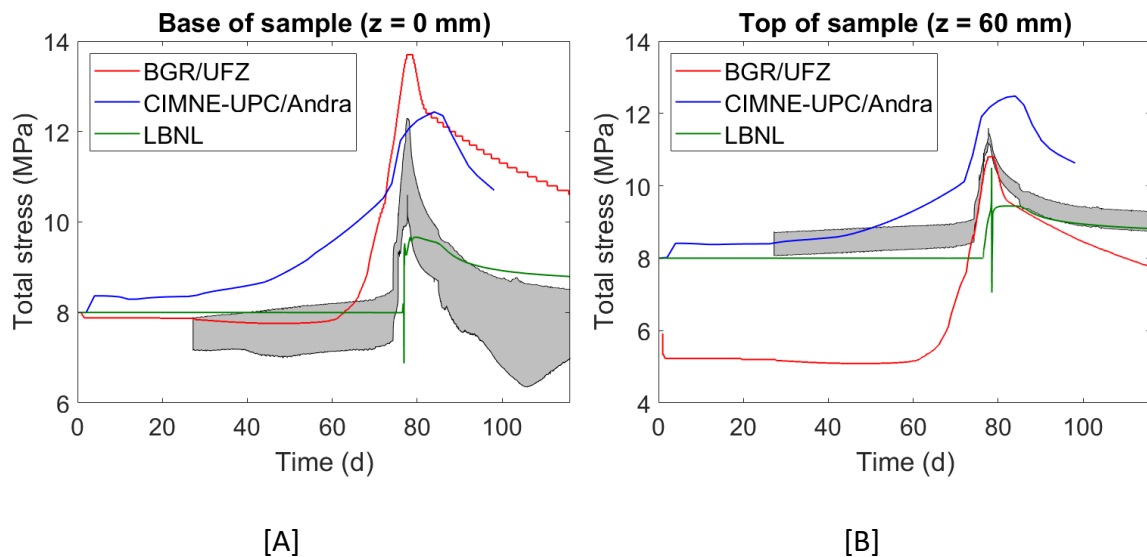
Figure 40. Axial stresses obtained at both the base and the top of the sample with the three numerical models. Grey zones represent experimental axial stresses.

Similarly, as with stresses, a visual inspection of the pore pressure data (Figure 41) indicates that:

- **Quiescence phase**: some teams obtain good initial values, although others underpredict the initial stage.
- **Rapid transition**: this remains, in general, a difficult experimental feature to capture. In some models, the response is too slow and the breakthrough is captured at earlier times than seen in the experiment. This is most likely a numerical diffusion effect and necessary to get gas into the sample for the numerical methods used.
- **Peak values**: reasonably good peak values are obtained with the three models.
- **Negative decay**: the post-peak shape trend is well defined by all models. Again, the steady-stage phase is not numerically observed, as simulations have not run for sufficient time.

Inflow and outflow curves were also analysed. As seen in Figure 42[A], some modelling teams used the experimental inflow as a boundary condition whereas others modelled the change in volume of gas based on the injection pump rate to determine the pressure from the ideal gas law. Thus, the analysis of the inflow modelling results makes it difficult

to carry out a direct comparison. Figure 42[B] shows the outflow results. The model developed by LBNL is capable of obtaining good fits with respect to both the abrupt increase in fluid flow and its timing. Other curves either show an earlier (BGR/UFZ) or a later (CIMNE-UPC/Andra) peak, whose value is overpredicted (almost a factor of 2 was observed). The observed shape of the post-breakthrough curve, which shows a shut-in behaviour and is directly linked to the stress state, is poorly reflected by all the models. This suggests a better understanding or representation of the hydro-mechanical coupling is still required for a detailed representation of the system.
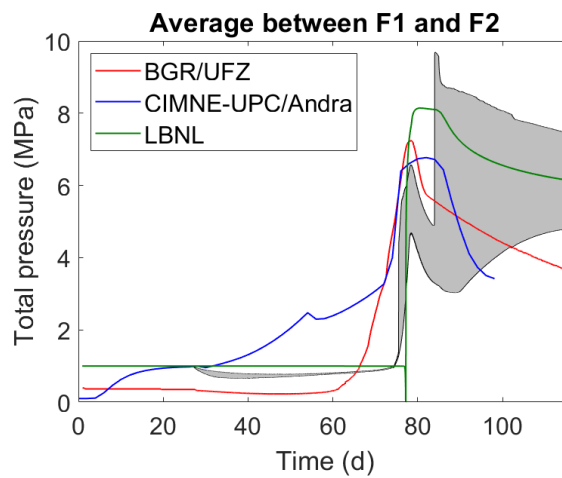
Figure 41. Average pore pressure obtained with the three numerical models plotted against the whole range of experimental pore pressure.
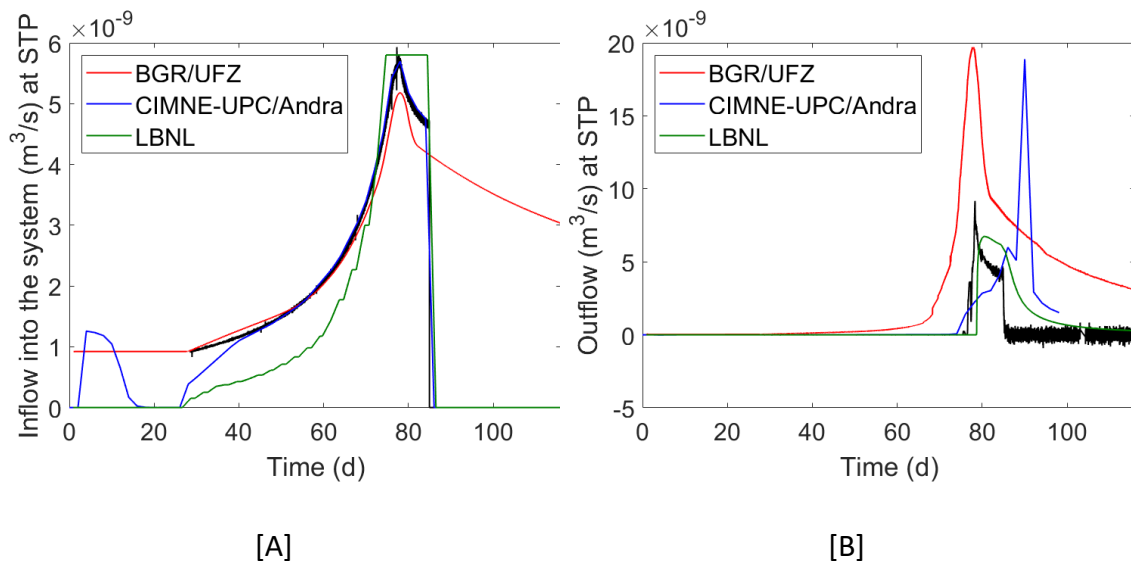
Figure 42. Flow curves at STP obtained with the model developed by CIMNE-UPC/Andra plotted against the experimental data: [A] inflow into the system and

As a summary, although the numerical approaches are not able to describe the full complexity of the physical processes, they are capable of matching key aspects of the evolution (e.g., peak values, breakthrough-timings, decay). The fact that some of the requested outputs are well represented without necessarily obtaining a good match to the entire dataset suggests that some of the underlying conceptual models are more/less sensitive to the individual couplings that appear in the system, and therefore that different models may be better/worse at representing selected aspects of the system evolution.

It is worth noting that these numerical fits are obtained after a calibration process. Indeed, the adjustment of a very large set of parameters (see Appendix A) is needed and detailed sensitivity analysis are required. Their determination is extremely cumbersome (with uniqueness not guaranteed) since although each parameter mainly controls a particular effect with respect to the global response, all of them are correlated due to the very pronounced coupling between the hydraulic and mechanical response. These calibrated models lead to some calculated properties, such as gas saturations, being beyond physically reasonable values, suggesting the physical description of the system remains incomplete. Indeed, as seen in Figure 43, some high gas saturation profiles are obtained by some models. As also seen, BGR/UFZ saturation profiles are nearly constant throughout the simulation. This limitation is due to the fact that this model assumes that the pore fluid in the bentonite is located in the intra-aggregated pore spaces and

therefore, it does not change much during the gas flow experiment. Indeed, the stochastic distribution of the gas entry pressure (see section 3.1.1) is the responsible mechanism for the variability of the saturation in the bentonite.

The shown time series data are obtained in single points (at the sensors) and thus, categorical conclusions cannot be drawn. That said, post-test measurements yielded no measurable gas saturations within the sample as a whole. Therefore, high gas saturation profiles suggest that either the model capillary relationship governing desaturation is incorrect or too many pathways (with too high permeability) are present in the model.
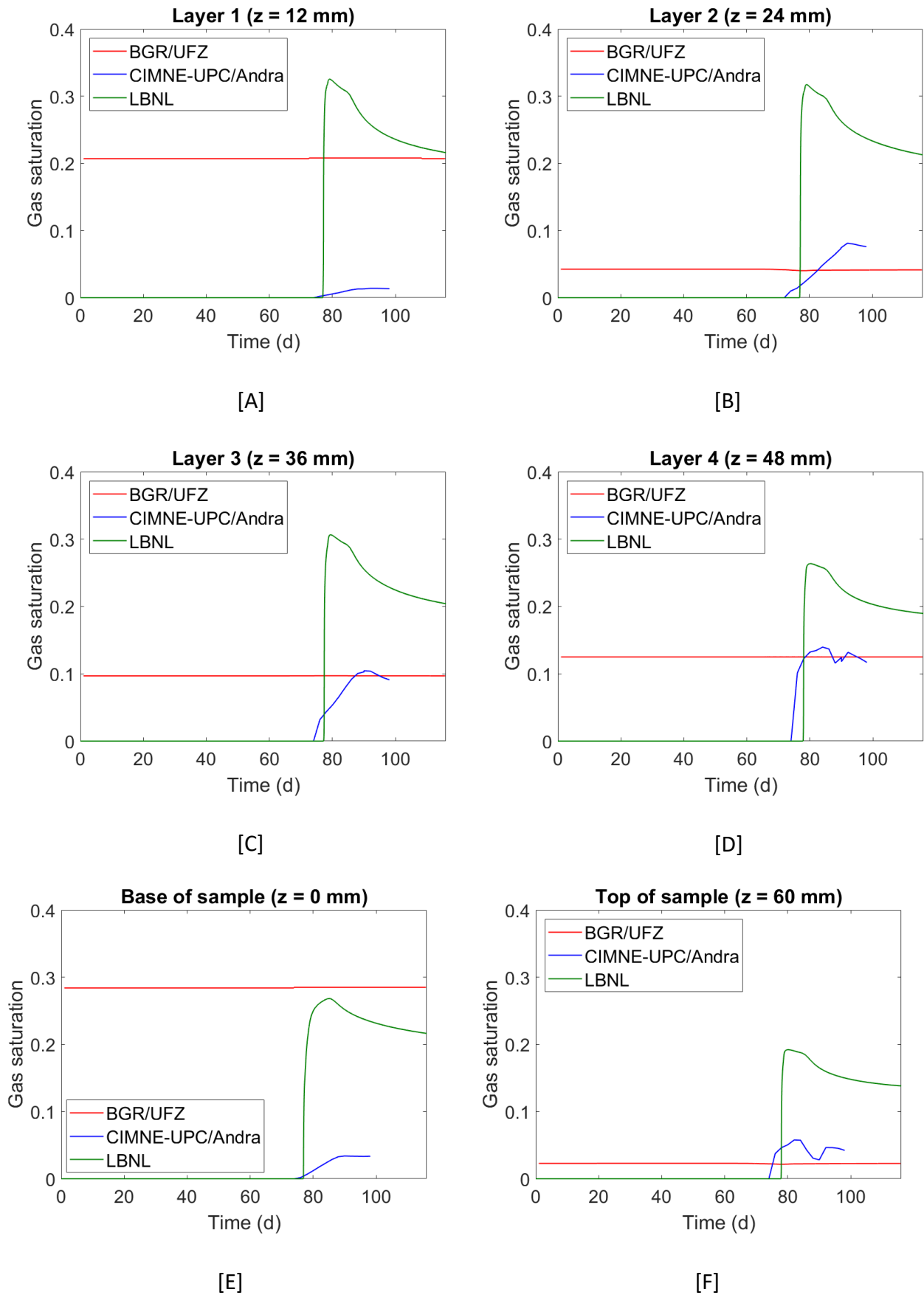
Figure 43. Gas saturation profiles at each layer, at the base and at the top of the sample obtained with the three numerical models.

4.2 Field-scale test

The capabilities of four numerical models (BGR/UFZ, LBNL, CIMNE-UPC/Andra and KAERI) were assessed by comparing the simulated results against the experimental data obtained from the Äspö Hard Rock Laboratory. Teams were asked to provide scientific evidence that the developed models are able to capture the main key aspects of the experimental time series data rather than the exact details of the test stage. In particular, teams were asked to prove that their models are able to capture the following seven features:

1. As gas is being injected into the system (**evolution of the injection pressure**), a
2. **rapid gas breakthrough** is observed.
3. This occurs at a **particular breakthrough time** and at a
4. **very low gas saturation**, which then leads to a
5. **gas peak value**, which is then followed by a
6. a **negative decay** to steady state (and subsequent decays as inflow rate is reduced).

These key features are observed together with

7. **small variations in pore pressures and stresses**.

Here, for the sake of comparison, final numerical outcomes (obtained after different sensitivity analyses) are employed. For a detailed overview of the development process and the sensitivity analysis performed within the DECOVALEX-2023 phase, we refer to the individual contributions of the modelling participants (see for instance contributions by Radeisen 2023 and Sayad Noghretab et al. 2022).

In order to assess key features 1, 2, 3, 5 and 6, the evolution of the injection pressure is shown in Figure 44. As observed, only three models can actually be assessed, as the KAERI model uses the injection pressure as input data (Dirichlet boundary condition). As seen, the three numerical approaches are able to predict the overall experimental response during the first three gas ramps. However,

- At Day 3163.04, when the fourth and final pressure ramp was started, differences are observed in the response predicted by the model developed by CIMNE-UPC/Andra. Indeed, a slower pressurisation response is observed as compared to the experimental behaviour, leading to a later gas peak pressure (at Day 3250, that is 44 days later than in the field). This relates to the way in which gas pressure is coupled to gas permeability within the model. The gas peak

pressure value is well predicted (with less than a 2% error) and the characteristic negative decay of the post-peak behaviour is also well captured.

- At Day 3197.9, an initial gas peak pressure of 5.92 MPa is predicted by the BGR/UFZ model indicating that a first small gas entry occurs. The cause for this initial peak pressure is unclear, but after it, the model predicts the rapid experimental breakthrough response. This is followed by a second pressurisation phase leading to a peak gas pressure of 6.01 MPa (less than a 3% error with respect to the experimental value) at Day 3205.5. Following breakthrough, inflow to the clay spontaneously decreases until day 3207, when gas pressure begins to slowly increase. During this time gas flow into the bentonite continued at a slower rate, Figure 45, while gas pressure slowly increased, peaking at 6.06 MPa at day 3228.18 (i.e., 28 days later than in the field). Thereafter gas pressure exhibited the characteristic negative pressure transient closely matching the data.

- LBNL model is able to correctly capture the evolution of the injection pressure. Indeed, a gas peak pressure of 6.15 MPa (with less than a 0.4% error with respect to the experimental value) is captured at Day 3207.7 (only two days later than experimental response). However, around Day 3246, the post-peak gas pressure shows a positive trend in contrast to the data which continuously to decay in pressure. This model response needs to be better understood.

The fourth key feature (very low gas saturation) is assessed by means of different outputs. First, the average gas saturation profile is analysed. As seen from the gas saturation time-series data (Figure 46), all models capture gas flow with very low gas saturation. As seen, BGR/UFZ model predict tiny variations of saturation (a difference of 3.4×10^{-4} between maximum and minimum values is observed) whereas KAERI model predicts a constant curve. Gas saturation values at three different timings (at initial time of the simulation, at the time where the model predicts the gas pressure peak and at final day 3283) and at three different distances from the centre of the canister (at 575 mm, at 725 mm and at 850 mm) at the level of the injection filter, see the scheme in Figure 47, are shown in Table 8. As reported, saturation values lie within 0 and 0.127. In particular, gas saturation predicted by BGR/UFZ far away from the centre of the canister (i.e., at 725 and 850 mm) is constant during all the simulation (0.003) whereas small variations of gas saturation (from 0.001 to 0.004) are predicted near the centre of the canister (at 575 mm). A similar behaviour is observed by LBNL's model, as gas saturation far away from the centre of the canister vanishes during all the simulation whereas gas saturation at 575 mm from the centre of the canister reaches a final value of 0.054. KAERI's predict tiny variations during all the simulation everywhere, as gas saturation

values lie within 0.010 and 0.014. CIMNE-UPC/Andra also captures small gas variations away from the canister (from 0.002 to 0.090). However, higher gas saturation values are predicted near the centre of the canister once the breakthrough is reached (around 0.12). In general, all models predict that gas flow is very localised within the swollen bentonite and the bentonite interfaces, as expected, see Figure 48. However, in the conceptual model of dilatant gas flow, gas saturation at specific points within the model should be either zero or 100% (i.e., inside a dilatant gas pathway). The presence of low gas saturations probably reflects the averaging of saturation values across the plane of reference, which could be either a 2D surface or a 3D volume. It could also stem from the mismatch in physics between the conceptual model of dilatant pathway creation and the continuous models used by the teams. In the latter, all models link gas pressure to permeability which, through retention functions, result in the displacement of water and gas penetration of the surrounding clay. However, this mode of desaturation is unlikely and is not reflected in the experimental data.

[A]   [B]
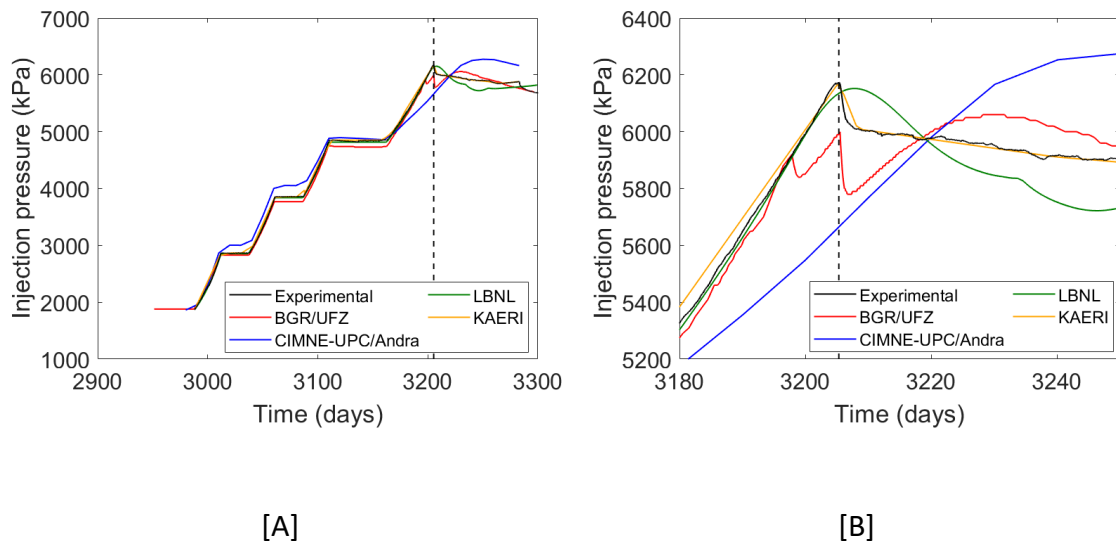
Figure 44. The filter pressure of FL903 during Gas Injection Test 4. [A] Evolution of both the experimental and numerical outputs and [B] detail around the breakthrough time. Black dashed line in this figure and in subsequent figures indicates breakthrough.
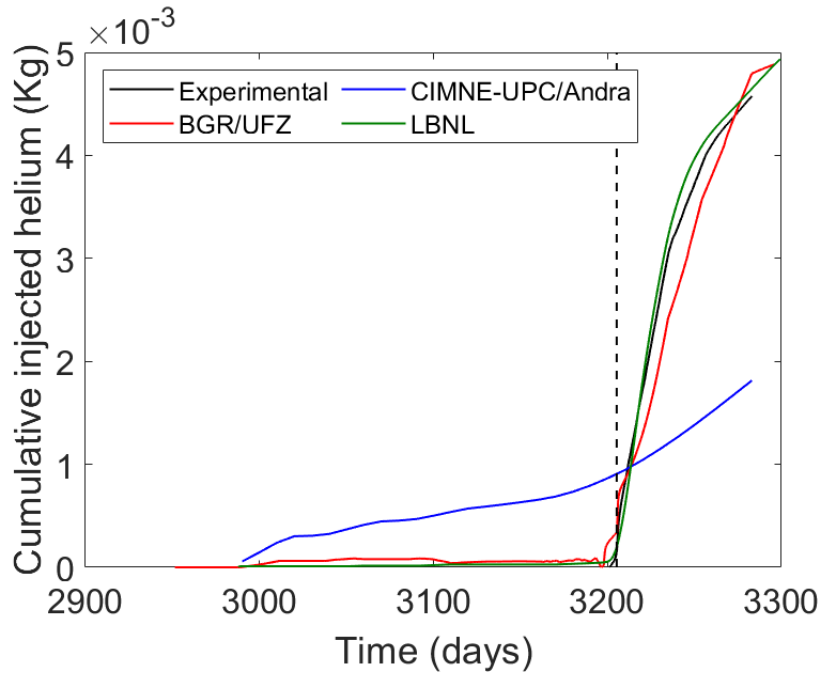
Figure 45. Cumulative injection mass predicted by different teams. Note that KAERI's model prescribe pressure evolution to simulate the gas injection process (see Figure 44) and thus, the amount of injected helium has not been estimated.
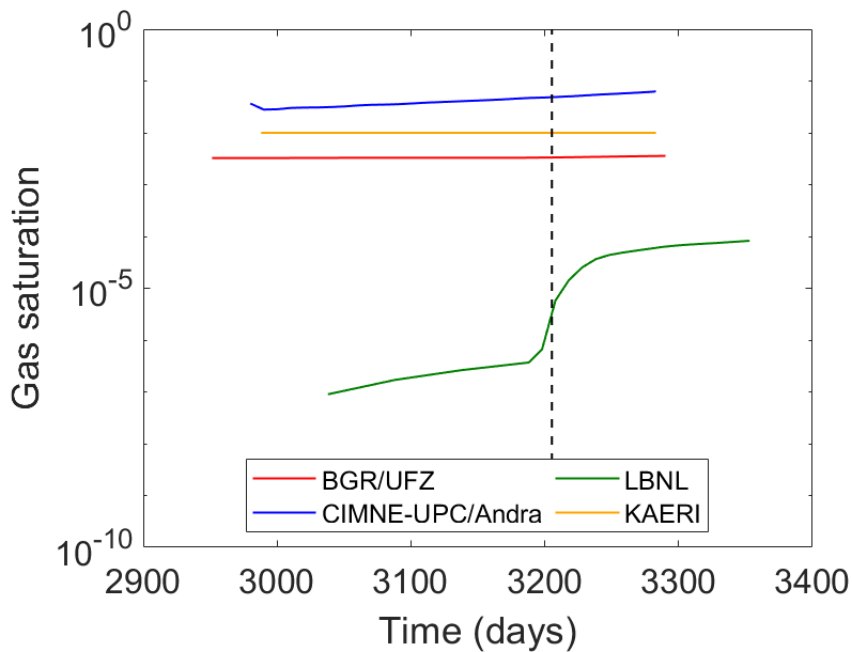
Figure 46. Average gas saturation profiles (y-axis in logarithmic scale). Note that a straight comparison is not easy, as average values depend on the technique for averaging that each team has used.
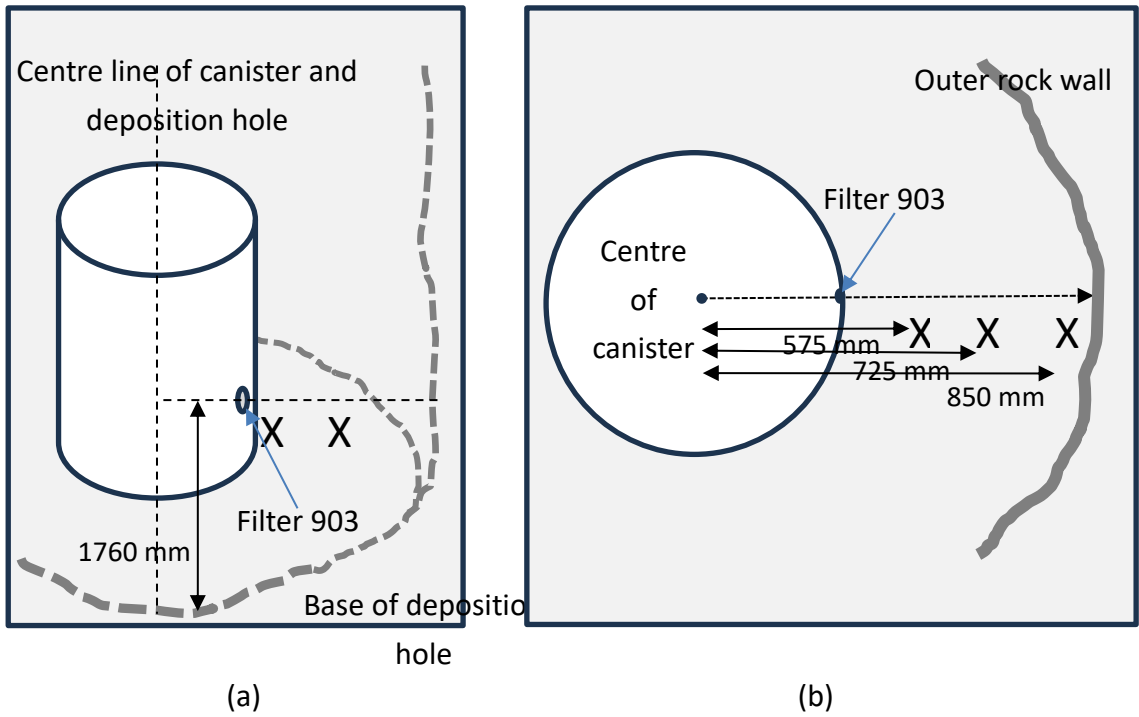
Figure 47. Schematic drawing of the locations where gas saturation is being assessed: (a) side and (b) plan views.
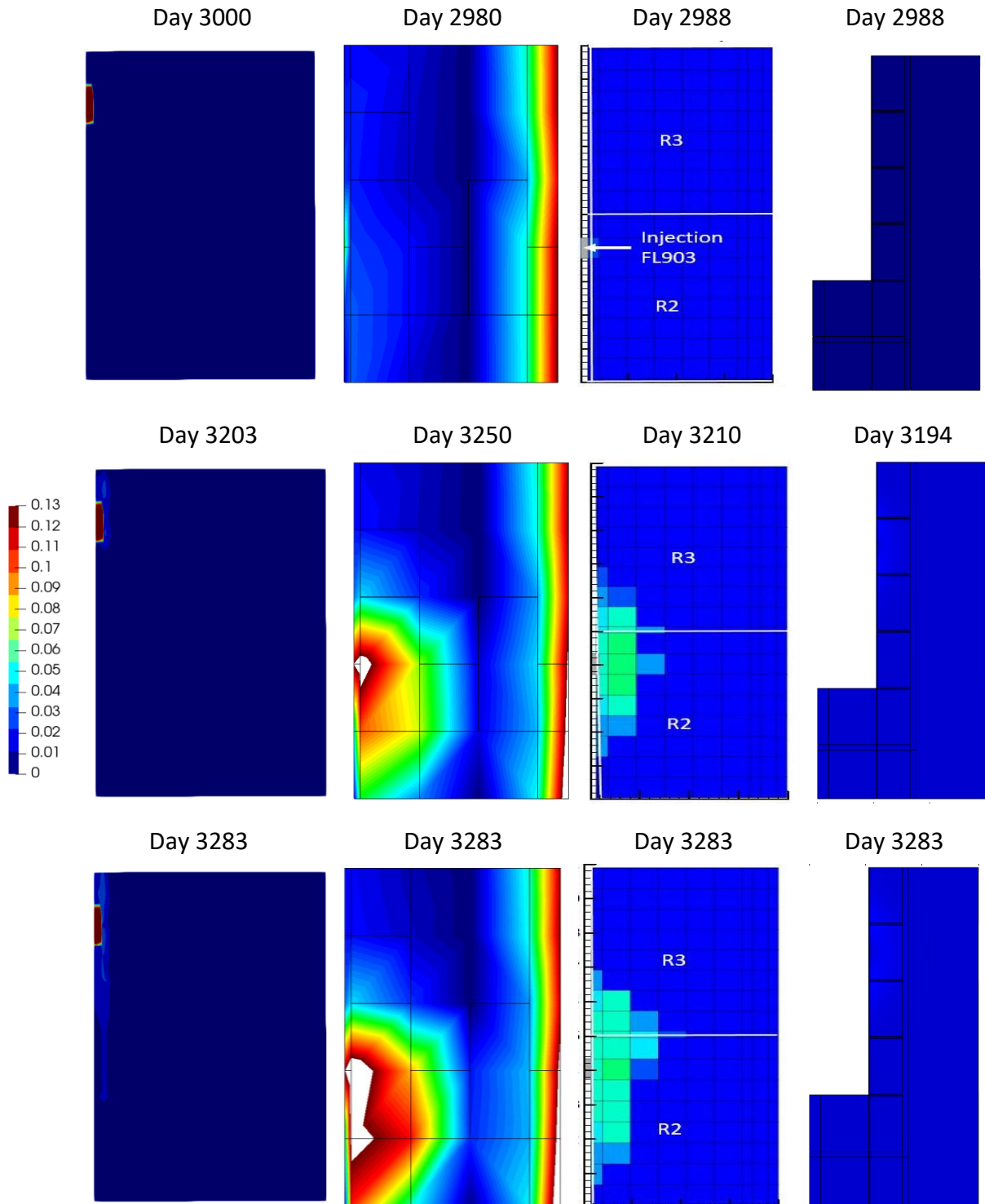
Figure 48. Average gas saturation contour plots (across a two-dimensional surface tangential to filter FL903) predicted by the teams (BGR/UFZ in column 1, CIMNE-UPC/Andra in column 2, LBNL in column 3 and KAERI in column 4). Each row corresponds to a different time of the simulation (at initial time of the simulation, at the time where the model predicts the gas pressure peak and at day 3283).

Table 8. Gas saturation values predicted by the teams at different locations and at different timings.

		Initial time	Time where gas peak is reached	At day 3283
At 575 mm from the centre of the canister	**BGR/UF**	0.001	0.004	0.004
	LBNL	0.000	0.042	0.054
	CIMNE-UPC/Andra	0.019	0.115	0.127
	KAERI	0.010	0.014	0.013
At 725 mm from the centre of the canister	**BGR/UF**	0.003	0.003	0.003
	LBNL	0.000	0.000	0.000
	CIMNE-UPC/Andra	0.002	0.012	0.019
	KAERI	0.010	0.014	0.014
At 850 mm from the centre of the canister	**BGR/UF**	0.003	0.003	0.003
	LBNL	0.000	0.000	0.000
	CIMNE-UPC/Andra	0.090	0.088	0.087
	KAERI	0.010	0.012	0.012

To assess the seventh key feature, a visual inspection of the stress and pore pressure data is required. As shown in Figure 49[A], all the models but KAERI are able to predict radial stresses within the experimental bounds. While BGR/UFZ, LBNL and KAERI models can simulate the experimentally-observed small variations, CIMNE-UPC/Andra values present higher variations. In particular, CIMNE-UPC/Andra's stress values present a piecewise-linear function with a clear turning point at day 3250 (when breakthrough is predicted by their model). This is due to the fact that, as radial stress responds to pore

pressure and effective stress cannot change significantly due to the absence of total volume changes, pore pressure and total stress change jointly. As shown in Figure 49[B], average numerical pore pressures obtained with different models present significant differences. BGR/UFZ and LBNL are able to capture very small variations in terms of pore pressures (in Figure 49[B] some model results seem constant due to the scale). However, BGR/UFZ results are higher than expected and do not lie within the experimental bounds. CIME-UPC/Andra outputs are characterised by small variations until the experimental breakthrough occurs. Beyond this point, the model predicts an increment of pressures reaching a maximum value at day 3280. Finally, it is worth noting that KAERI's pore pressure behaviour is fully coupled to the injection pressure behaviour (see Figure 44). The experimentally-observed small variations are not reproduced and hence, the complexity of the process is not fully described.

[A]   [B]
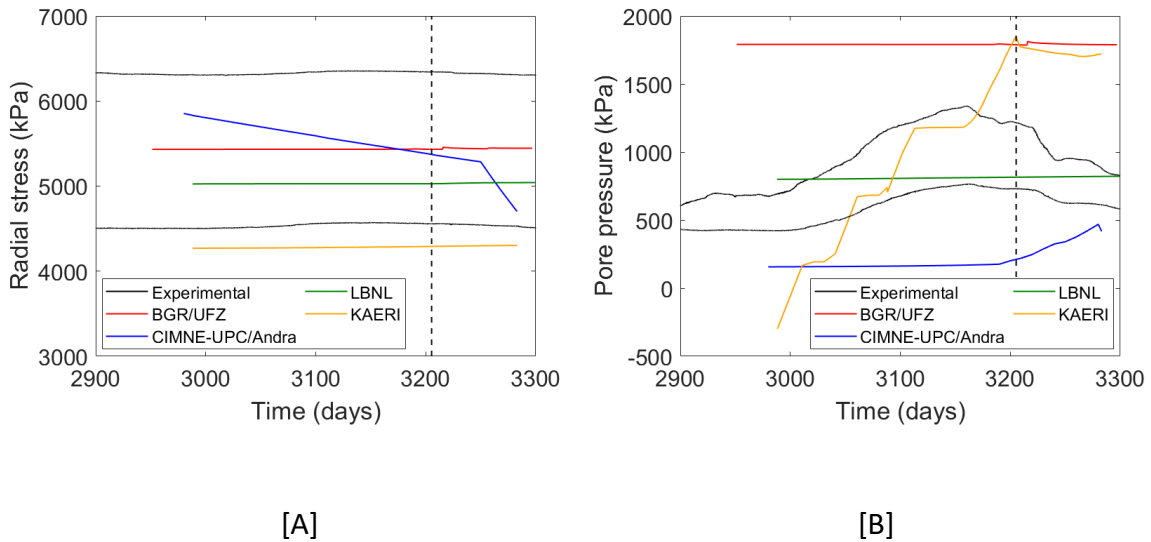
Figure 49. Average [A] radial stresses and [B] pore pressures obtained with the four numerical models plotted against the maximum and minimum experimentally-obtained values.

5 Conclusions

This report presents a summary of work performed in Task B of the current phase of DECOVALEX (DECOVALEX-2023) in which five teams have developed hydro-mechanical approaches for the modelling and representation of dilatant-controlled advective gas flow through very low-permeability materials.

Using a linear stability analysis, one team (SNL) developed a new conceptual model to describe gas percolation in low-permeable deformable media. This theoretical analysis shows that gas channelling can autonomously emerge from the morphological instability of the interface between the injected gas and the compacted bentonite due to local stress concentration, pore dilation, and hydrologic gradient variations. The pattern of channels formed as such possesses a fractal geometry, which poses a challenge for numerical simulations, since the existing numerical algorithms and tools may not be able to directly handle the evolution of fractal structures. However, although this new model has the potential to provide valuable insight into the challenges of modelling gas flow in natural materials, its numerical development is still in a very preliminary phase and it cannot be used to reproduce the experiments. Thus, from a pragmatic perspective, enhanced flow models remain the only viable tool to represent these systems at this time.

This study has allowed four teams (BGR/UFZ, LBNL, CIMNE-UPC/Andra and KAERI) to test their enriched multi-phase flow models and codes and enhance them in order to include the main deterministic features observed in both laboratory- and field-scale gas injection tests. To this end, other high-quality experimental datasets would be useful to help build additional confidence in the understanding of the key processes governing gas flow, the continued development and verification of numerical models, and the representation of these complex processes across different repository scales. In this study, BGR/UFZ developed a hydro-mechanical model that included a pressure-dependent intrinsic permeability and an elasto-plastic heterogeneous porous medium; CIMNE-UPC/Andra developed a coupled hydro-gas-mechanical 3D numerical model that assumes a heterogeneous initial permeability field and embedded fractures; LBNL applied a continuum approach with a direct relation between permeability and least principal effective stress; and KAERI developed a hydro-mechanical model for migration of gas through a low-permeable material that included a damage model to account for the deterioration of the rock after gas breakthrough.

As a first stage, three of these teams (BGR/UFZ, LBNL and CIMNE-UPC/Andra) have enhanced their numerical strategies by means of their comparison against a laboratory-

scale test subjected to a constant volume boundary condition. BGR/UFZ is able to correctly capture initial and peak stress values. However, the rapid transition phase seen at breakthrough is still too smoothly and too early predicted (Figure 39 and Figure 40). In terms of stresses, a similar behaviour is obtained when CIMNE-UPC/Andra's approach is employed. In terms of outflows, an earlier (BGR/UFZ) and a later (CIMNE-UPC/Andra) peak are obtained. LBNL's approach along with a gas entry pressure that is scaled with the permeability can be used to simulate the macroscopic stress behaviour (Figure 39 and Figure 40), although the model is not refined enough to capture microscopic dilatancy and heterogeneous gas channelling. The observed shape of the post-breakthrough flow curve, which shows a shut-in behaviour and is directly linked to the stress state, is poorly reflected by all the models thus suggesting a better representation of the hydro-mechanical processes governing gas flow into models that do not explicitly represent them might be beneficial, dependent on the end use of the models.

As a second stage, four teams (BGR/UFZ, LBNL, CIMNE-UPC/Andra and KAERI) have enhanced their models to simulate a field-scale test. In particular, a highly instrumented test based around a mock canister, encapsulated in bentonite/pellets, and placed within a deposition hole at the Äspö underground research laboratory (Sweden) has been reproduced by the teams. Codes have not been substantially modified: indeed, model parameters calibrated and validated at laboratory-scale have been applied to predict field-scale gas flow at Lasgit, including peak gas pressure and injected cumulative gas volume. The only exception was the introduction of interfaces between blocks to reflect the experimental configuration. Inclusion of these features within the codes necessitated changing of some parameters (e.g., assuming higher permeability), see Appendix A. These adjusted models were then able to represent most of the key features observed in the experimental data. Small differences between the model predictions and the experimental data, such as the timing and stress changes during the transitional phase during gas entry, the evolution in gas flow following breakthrough or the post peak negative transient phase, all stem from the fundamental differences between the modelling approaches (based on the physics of visco capillary flow) and that of the data (indicating dilatant pathway flow). However, in the absence of any model that can represent pathway dilatancy, the enhanced two-phase flow models proposed in this study can effectively used to simulate both controlled-laboratory experiments and field-scale tests. However, such models have yet to be validated against sufficient datasets to be used as a predictive tool, since the discrepancy between the physics of the models and that of the process governing gas flow remains a significant challenge.

6   Planned and Completed Publications

Table 9 gives the planned and completed publications under this task, correct at the time of writing.

Table 9: Planned and completed journal and conference papers for Task B.

Author(s)	Title	Journal/ Conference	Status
Tamayo-Mas E., Harrington J.F., Damians I.P., Olivella S., Radeisen E., Rutqvist J. and Wang Y.	A comparative study of theoretical and numerical approaches for the description of advective gas flow in clay-based repository systems	Geomechanics for Energy and the Environment	Published
Radeisen E., Shao H., Hesser J., Kolditz O., Xu W. and Wang W.	Simulation of dilatancy-controlled gas migration processes in saturated bentonite using a coupled multiphase flow and elastoplastic H2M model	Journal of Rock Mechanics and Geotechnical Engineering (2023)	Published
Radeisen E., Shao H., Pitz M., Hesser, J. and Wang W.	Derivation of heterogeneous material distributions and their sensitivity to HM-coupled two-phase flow models exemplified with the LASGIT experiment.	Environmental Earth Sciences (2023)	Published
Sayad Noghretab B., Damians I.P., Olivella S. and Gens A.	Numerical gas flow simulation through clay materials applying material heterogeneity at large scale scenario	3rd International Conference on Coupled Processes in Fractured Geological Media: Observation, Modeling, and Application (CouFrac2022)	Published
Sayad Noghretab B., Damians I.P., Olivella S. and Gens A.	Exploring material heterogeneity in gas flow simulation through clay materials: a	Workshop Of Code_Bright Users (2023)	Published

	numerical model study		
Damians I.P., Olivella S. and Gens A.	3D simulations of gas injection on Callovo-Oxfordian claystone assuming spatial heterogeneity and anisotropy	International Journal of Rock Mechanics and Mining Sciences (2022)	Published
Rutqvist J., Tamayo-Mas E., Harrington J. and Cuss R.	Modeling gas flow through bentonite backfilled nuclear waste emplacement tunnels considering preferential flow along interfaces	3rd International Conference on Coupled Processes in Fractured Geological Media: Observation, Modeling, and Application (CouFrac2022)	Published

7 Acknowledgements

8 References

Bandis S.C., Lumsden A.C. and Barton N.R. 1983. Fundamentals of rock joint deformation. International Journal of Rock Mechanics and Mining Sciences and Geomechanic Abstracts, 20, 249–68. DOI: 10.1016/0148-9062(83)90595-8

Biot M.A. and Willis D.G. 1957. The elastic coefficients of the theory of consolidation. Journal of Applied Mechanics, 24, 594–601. DOI: 10.1115/1.4011606

Börgesson L., Johannson L.E., Sandén T. and Hernelind, J. 1995. Modelling of the physical behaviour of water saturated clay barriers. Laboratory tests, material models and finite element application. Swedish Nuclear Fuel and Waste Management Co.; Stockholm (Sweden).

Chittenden N., Benbow S., Bond A. and Norris S. 2020. Development of an upscalable HM model for representing advective gas migration through saturated bentonite. International Journal of Rock Mechanics and Mining Sciences, 133: 104415. DOI: 10.1016/j.ijrmms.2020.104415.

COMSOL. 2018. COMSOL Multiphysics version 5.4a. Manual.

Cuss R.J., Harrington J.F. and Noy D.J. 2010. Large scale gas injection test (Lasgit) performed at the Äspö Hard Rock Laboratory. Svensk Kärnbränslehantering AB; Stockholm, Sweden.

Cuss R.J., Harrington J.F., Tamayo-Mas E., Noy D.J., Birchall, D.J, Sellin P. and Nord M. 2022. Large scale gas injection test (Lasgit) performed at the Äspö Hard Rock Laboratory. Final report. SKB TR-22-06.

Dai Z., Samper J., Wolfsberg A. and Levitt D. 2008. Identification of relative conductivity models for water flow and solute transport in unsaturated bentonite. Physics and Chemistry of the Earth, Parts A/B/C, 33, 1, pp. S177-S185. DOI: 10.1016/j.pce.2008.10.012

Damians I.P., Olivella S. and Gens A. 2020. Modelling gas flow in clay materials incorporating material heterogeneity and embedded fractures. International Journal of Rock Mechanics and Mining Sciences, 136, 104524. DOI: 10.1016/j.ijrmms.2020.104524

Daniels K.A. and Harrington J.F. 2017. The response of compact bentonite during a 1D gas flow test. British Geological Survey Open Report. OR/17/067.

Delage P. and Lefebvre G. 1984. Study of the structure of a sensitive clay and of its evolution during consolidation. Canadian Geotechnical Journal, 21, 21–35. DOI: 10.1139/t84-003

Faybishenko B., Wang Y., Harrington J.F., Tamayo-Mas E., Birkholzer J. and Jové-Colón C. 2022. Phenomenological Model of Nonlinear Dynamics and Deterministic Chaotic Gas Migration in Bentonite: Experimental Evidence and Diagnostic Parameters. Transport in Porous Media. 1573-1634. DOI: 10.1007/s11242-021-01733-9

Gray W.G. and Hassanizadeh M. 1991. Unsaturated flow theory including interfacial phenomena. Water Resources Research, 27, 1855-1863. DOI: 10.1029/91WR01260

Guo G. and Fall M. 2018. Modelling of dilatancy-controlled gas flow in saturated bentonite with double porosity and double effective stress concepts. Engineering Geology, 243: 253-271. DOI: 10.1016/j.enggeo.2018.07.002

Harrington J.F. and Horseman S.T. 2003. Gas migration in KBS-3 buffer bentonite. Sensitivity of test parameters to experimental boundary conditions. Technical Report TR-03-02. Svensk Kärbränslehantering AB (SKB), Stockholm, Sweden.

Harrington J.F., Milodowski A.E., Graham C.C., Rushton J.C. and Cuss R.J. 2012. Evidence for gas-induced pathways in clay using a nanoparticle injection technique. *Mineralogical Magazine*, 76(8): 3327-3336. DOI: 10.1180/minmag.2012.076.8.45

Harrington J.F., Graham C.C., Cuss R.J. and Norris S. 2017. Gas network development in a precompacted bentonite experiment: Evidence of generation and evolution. Applied Clay Science, 147: 80-89. DOI: 10.1016/j.clay.2017.07.005

Harrington J.F., Graham C.C., Cuss R.J. and Norris S. 2019. Gas Network Development in Compact Bentonite: Key Controls on the Stability of Flow Pathways. Geofluids, 2019: 1-19. DOI: 10.1155/2019/3815095

Hoch A.R., Cliffe K.A., Swift B.T. and Rodwell W.R. 2004. Modelling Gas Migration in Compacted Bentonite: GAMBIT Club Phase 3 Final Report. POSIVA Report 2004-2. Posiva Oy, Olkiluoto.

Horseman S.T., Harrington J.F. and Sellin P. 1996. Gas Migration in MX80 Buffer Bentonite. MRS Online Proceedings Library 465: 1003-1010. DOI: 10.1557/PROC-465-1003

Itasca, Flac3d Version 6.0. 2018. Fast Lagrangian Analysis of Continua in 3 Dimensions. ITASCA Consulting Group Inc. https://www.itascacg.com/software/flac3d

Kim K., Rutqvist J., Harrington J.F., Tamayo-Mas E. and Birkholzer J.T. 2021. Discrete Dilatant Pathway Modeling of Gas Migration Through Compacted Bentonite Clay.

International Journal of Rock Mechanics and Mining Sciences, 137, 104569. DOI: 10.1016/j.ijrmms.2020.104569

Kolditz O., Bauer S., Bilke L., Böttcher N., Delfs J.O., Fischer T., Görke U.J., Kalbacher T., Kosakowski G., Mcdermott C.I., Park C.H., Radu F., Rink K., Shao H., Shao H.B., Sun F., Sun Y.Y., Singh A.K., Taron J., Walther M., Wang W., Watanabe N., Wu N., Xie M., Xu W. and Zehner B. 2012. OpenGeoSys: An open-source initiative for numerical simulation of thermo-hydro-mechanical/chemical (THM/C) processes in porous media. Environmental Earth Sciences, 67, 589-599. DOI: DOI:10.1007/s12665-012-1546-x

Lee J., Lee C. and Kim G.Y. 2019. Task A Stage 1A Numerical Modelling of One Dimensional Gas Injection Experiment using Mechanical Damage Model: DECOVALEX-2019 Task A Stage 1A. *Tunnel and Underground Space*, 29(4), 262-279. DOI: 10.7474/TUS.2019.29.4.262.

Lee J., Lee C. and Kim G.Y. 2020. Numerical Modelling for the Dilation Flow of Gas in a Bentonite Buffer Material: DECOVALEX-2019 Task A. *Tunnel and Underground Space*, 30(4), 382-393. DOI: 10.7474/TUS.2020.30.4.382.

Manai T. 1995. EVEGAS: European validation exercise of GAS migration models through geological media: Phase 1 - Final Report. European Commission Report EUR 16639 EN. European Commission, Nuclear Science and Technology Series, Directorate-General, Science, Research and Development, Luxembourg.

Manai T. 1997a. EVEGAS: European validation exercise of gas migration models through geological media: Phase 2 - Final Report. European Commission Report EUR 17556 EN. European Commission, Nuclear Science and Technology Series, Directorate-General, Science, Research and Development, Luxembourg.

Manai T. 1997b. EVEGAS: European validation exercise of gas migration models through geological media: Phase 3 - Final Report. European Commission Report EUR 17557 EN. European Commission, Nuclear Science and Technology Series Directorate-General, Science, Research and Development, Luxembourg.

Nash P.J., Swift B.T., Goodfield M. and Rodwell W. R. 1998. Modelling Gas Migration in Compacted Bentonite: A report produced for the GAMBIT Club. POSIVA Report 98-08. Posiva Oy, Helsinki.

Nittmann J., Daccord G. and Stanley H. 1985. Fractal growth viscous fingers: quantitative characterization of a fluid instability phenomenon. Nature 314, 141–144. DOI: 10.1038/314141a0

Olivella S., Gens A., Carrera J. and Alonso E.E. 1996, Numerical formulation for a simulator (CODE_BRIGHT) for the coupled analysis of saline media, Engineering Computations, 13(7), 87-112. DOI: 10.1108/02644409610151575

Olivella S. and Alonso E.E. 2008. Gas flow through clay barriers. Geotechnique, 58, 157-168. DOI: 10.1680/geot.2008.58.3.157

Pruess K, Oldenburg C.M. and Moridis G. 2012. TOUGH2 User's Guide, Version 2.1, LBNL-43134 (revised). Berkeley, California: Lawrence Berkeley National Laboratory.

Radeisen E., Shao H., Hesser J., Kolditz O., Xu W. and Wang W. 2023. Simulation of dilatancy-controlled gas migration processes in saturated bentonite using a coupled multiphase flow and elastoplastic H2M model. Journal of Rock Mechanics and Geotechnical Engineering, 15(4): 803-813. DOI: 10.1016/j.jrmge.2022.05.011.

Radeisen E., Shao H., Pitz M., Hesser J. and Wang W. 2023. Derivation of heterogeneous material distributions and their sensitivity to HM-coupled two-phase flow models exemplified with the LASGIT experiment. Environmental Earth Sciences, 347. DOI: 10.1007/s12665-023-11004-z

Rutqvist J., 2011. Status of the TOUGH-FLAC simulator and recent applications related to coupled fluid flow and crustal deformations. Computer & Geosciences, Volume 37, Issue 6 (June 2011), pp. 739-750.

Rutqvist J., 2017. An overview of TOUGH-based geomechanics models. Computers & Geosciences, 108, 56–63 (2017). DOI: 10.1016/j.cageo.2016.09.007.

Rutqvist J., Wu Y.-S., Tsang C.-F. and Bodvarsson G. A., 2002. Modeling approach for analysis of coupled multiphase fluid flow, heat transfer, and deformation in fractured porous rock. International Journal of Rock Mechanics and Mining Sciences, 39, 429-442. DOI: 10.1016/S1365-1609(02)00022-9.

Rutqvist J., Ijiri Y. and Yamamoto H. 2011. Implementation of the Barcelona Basic Model into TOUGH–FLAC for simulations of the geomechanical behavior of unsaturated soils. Computers & Geosciences, 37, 6: 751-762. DOI: 10.1016/j.cageo.2010.10.011

Sayad Noghretab B., Damians I.P., Olivella S. and Gens A. 2022. Numerical gas flow simulation through clay materials applying material heterogeneity at large scale scenario. 3rd CouFrac - International Conference on Coupled Processes in Fractured Geological Media: Observation, Modeling, and Application, p. 1-4

Sayad Noghretab B., Damians I.P., Olivella S. and Gens A. Exploring material heterogeneity in gas flow simulation through clay materials: a numerical model study. Workshop Of Code_Bright Users (2023).

Seiphoori A. (2015): Thermo-Hydro-Mechanical Characterisation and Modelling of Wyoming Granular Bentonite. Nagra. Nagra Technical Report 15-05; Wettingen, Switzerland.

Senger R. and Marschall P. 2008. Task Force on EBS / Gas Transport in Buffer Material, Nagra Arbeitsbericht NAB 08–24.

Senger R., Romero E., Ferrari A. and Marschall P. 2014. Characterization of gas flow through low-permeability claystone: laboratory experiments and two-phase flow analyses. Geological Society, London, Special Publications, 400, 1, pp. 531-543. DOI: 10.1144/SP400.15

Senger R., Romero E. and Marschall P. 2018. Modeling of Gas Migration Through Low-Permeability Clay Rock Using Information on Pressure and Deformation from Fast Air Injection Tests. Transport in Porous Media, 123:563–579. DOI: 10.1007/s11242-017-0962-5

Swift B.T., Hoch A.R. and Rodwell W.R. 2001. Modelling Gas Migration in Compacted Bentonite: GAMBIT Club Phase 2 Final Report. POSIVA Report 2001-02. Posiva Oy, Olkiluoto.

Tamayo-Mas E., Harrington J.F., Brüning T, Shao H., Dagher E.E., Lee J., Kim K, Rutqvist J., Kolditz O., Lai S.H., Chittenden N., Wang Y., Damians I.P. and Olivella S. 2021. Modelling advective gas flow in compact bentonite: Lessons learnt from different numerical approaches. International Journal of Rock Mechanics and Mining Sciences, 139. DOI: 10.1016/j.ijrmms.2020.104580

Tamayo-Mas E., Harrington J.F., Damians I.P., Olivella S., Radeisen E., Rutqvist J., Wang Y. 2024. A comparative study of theoretical and numerical approaches for the description of advective gas flow in clay-based repository systems. Geomechanics for Energy and the Environment, 37, 100528. DOI: 10.1016/j.gete.2023.100528

Tang C.A., Tham L.G, Lee P.K.K, Yang T.H and Li L.C. 2002. Coupled analysis of flow, stress and damage (FSD) in rock failure in International Journal of Rock Mechanics and Mining Sciences, 39(4): 477-489. DOI: 10.1016/S1365-1609(02)00023-0.

van Genuchten M.T. 1980. A closed-form equation for predicting the hydraulic conductivity of unsaturated soils. Soil Science Society of America Journal, 44, 892–898. DOI: 10.2136/sssaj1980.03615995004400050002x

Villar M.V. 2005. MX-80 Bentonite. Thermo-Hydro-Mechanical Characterisation Performed at CIEMAT in the Context of the Prototype Project. Departamento de Impacto Ambiental de la Energía, Vol. 1053. Informes Técnicos CIEMAT: 45; Madrid, Spain.

Villar M.V., Iglesias R.J. and García-Siñeriz J.L. 2020. State of the in situ Febex test (GTS, Switzerland) after 18 years: a heterogeneous bentonite barrier. Environmental Geotechnics, 7, 2: 147-159. DOI: 10.1680/jenge.17.00093

Wang Y. 2014. Nanogeochemistry: Nanostructures, emergent properties and their control on geochemical reactions and mass transfers. Chemical Geology, 378-379, 1-23. DOI: 10.1016/j.chemgeo.2014.04.007

Wang Y. and Budd D.A. 2012 Stress-induced chemical waves in sediment burial diagenesis, Nature Communications, 3:685. DOI: 10.1038/ncomms1684.

Wang Y., Bryan B., Dewers T., Heath J.E. and Jove-Colon C. 2013. Ganglion dynamics and its implications to geologic carbon dioxide storage. Environmental Science and Technology, 47, 219–226. DOI: 10.1021/es301208k

Xu W., Shao H., Hesser J., Wang W., Kolditz O. and Popp T. 2011. Simulation of dilatancy-controlled gas migration process in saturated argillaceous rock. Computational Geomechanics, COMGEO II - Proceedings of the 2nd International Symposium on Computational Geomechanics. 693-703.

Yang J. and Fall M. 2021. Coupled hydro-mechanical modelling of dilatancy controlled gas flow and gas induced fracturing in saturated claystone. International Journal of Rock Mechanics and Mining Sciences, 138: 104584. DOI: 10.1016/j.ijrmms.2020.104584.

Appendix A: Model comparison

Differences between the proposed numerical strategies lie in conceptual features, the software used by the teams, in the assumed geometry to represent the saturated bentonite, in the initial/boundary conditions prescribed for the tests and in the material parameters. Here, these differences are reported.

A.1 Conceptual differences

Table 10. Brief description of the four numerical models developed by the participating teams.

	BGR/UFZ	LBNL	CIMNE-UPC/Andra	KAERI
Hydro-mechanical (HM) coupling	Fully coupled (via the Biot's effective stress)	Sequentially coupled (via the Biot's effective stress)	Fully coupled (via the Biot's effective stress)	Fully coupled (via the Biot's effective stress)
Key hydraulic features	Van Genuchten-Mualem model	Van Genuchten-Corey model	Fracture-dependent van Genuchten model/relative permeabilities	Van Genuchten-Mualem model
Mechanical deformation	Elasto-plasticity (Drucker-Prager with a tension cut-off parameter)	Linear elasticity (with swelling stress)	Elasticity (with a dilatancy term in the deviatoric component of the volumetric strains)	Elasto-damage model (damage factor from volumetric strain, only tension considered)

	BGR/UFZ	LBNL	CIMNE-UPC/Andra	KAERI
Dilatant pathways description	Strain-dependent intrinsic permeability triggered by a heterogeneous Young's modulus	Permeability is assumed to depend on pressure and the effective minimum compressive stress	Intrinsic and relative permeabilities are assumed to be decomposed into matrix and fracture terms	Intrinsic permeability is decomposed into undamaged and damaged terms

A.2 Codes

Table 11. Software employed by the participating teams.

	BGR/UFZ	LBNL	CIMNE-UPC/Andra	KAERI
Software	OpenGeoSys	TOUGH2 + FLAC3D	CODE_BRIGHT	COMSOL Multiphysics®
Version	5.8	TOUGH2 V2.1 FLAC3D V5	8.6	5.4
Reference	Kolditz et al. (2012)	Pruess et al. (2012) + Itasca (2018)	Olivella et al. (1996)	Comsol 2018

A.3 Test geometries

A.3.1   Laboratory-scale test

	BGR/UFZ	LBNL	CIMNE-UPC/Andra
Discretisation method	Finite element	Integral finite difference	Finite element
Geometry	2D triangular axisymmetric mesh	3D quadrilateral axisymmetric mesh	3D hexahedral mesh
Number of elements	2716	857	3430
Number of nodes	1448	1846	3909
Explicit description of the injector	Via a source term	Via a representative volume of the injection chamber	With all the relevant components (i.e., injection rod and injection filter tip)
Element order	2nd order (quadratic triangular)	Linear	Linear

A.3.2 Field-scale test

	BGR/UFZ	LBNL	CIMNE-UPC/Andra	KAERI
Discretisation method	Finite element	Integral finite difference	Finite element	Finite element
Geometry	3D hexahedral mesh (1/4 model)	3D quadrilateral mesh (1/2 model)	3D hexahedral mesh (1/4 model)	3D hexahedral mesh (1/4 model)
Number of elements	21840	37107	66948	9635
Number of nodes	24354	Not provided	13170	Not provided by the software
Material groups	7 (bentonite blocks, swollen bentonite, bentonite interfaces, solid rock, injection filter, copper cylinder and fractured rock)	4 (bentonite blocks, interfaces, injection filter, rock)	7 (bentonite blocks, pellets, interfaces, gap bentonite-copper, injection filter, host rock and copper cylinder)	5 (bentonite blocks, bentonite-bentonite interfaces, canister-bentonite interface(void), rock, pellet)

A.4 Prescribed initial conditions

A.4.1   Laboratory-scale test

Table 12. Initial conditions prescribed by teams.

	BGR/UFZ	LBNL	CIMNE-UPC/Andra
Pore-water pressure (MPa)	1.00	1.00	0.25
Pore-gas pressure (MPa)	3.00	1.00	0.10
Water saturation	97%	100%	100%
Swelling pressure	Compressive stress: no real swelling	8.0	-
Capillary pressure (MPa)	2.0	0.0	0.0
Displacements along x axis	-	0.0	0.0
Displacement along y axis	-	0.0	0.0
Displacements along z axis (if appropriate)	-	0.0	0.0
Stress (MPa)	-7.0 (effective compressive stress)	8.0	8.0
Temperature	20°	20°	20°

A.4.2   Field-scale test

Models differ on the assumed material groups considered and thus, we refer to conditions specified in specific subsections (in Section 3.1).

A.5 Prescribed boundary conditions

A.5.1   Laboratory-scale test

Table 13. Boundary conditions prescribed by teams.

	BGR/UFZ	LBNL	CIMNE-UPC/Andra
Pore-water pressure	-	1 (at outlet)	Variable (as per given test specifications)
Pore-gas pressure (MPa)	1 (top of sample, outflow)	1 (at outlet)	Variable (as per given test specifications)
Flowrate injector	$\dot{m}(t) = \dfrac{nV_0}{\Delta V_{In,t}}$	Prescribed until 85 days to match injection pressure rise	Prescribed from 22 to 85 days as per test Flow rate at STP plot given
Capillary pressure	-	0 at outlet/inlet	Variable (as per given test specifications)

	BGR/UFZ	LBNL	CIMNE-UPC/Andra
Displacements along x axis	Right boundary = 0 Left boundary = symmetry axis	0 normal to outer surface	0 at all outer surfaces
Displacement along y axis	Top and bottom boundary = 0	0 normal to outer surface	0 at all outer surfaces
Displacements along z axis (if appropriate)	-	0 normal to outer surface	0 at all outer surfaces
Temperature	20°	20°	20°

A.5.2   Field-scale test

Models differ on the assumed material groups considered and thus, we refer to conditions specified in specific subsections (in Section 3.1).

A.6 Parameter values

A.6.1   Laboratory-scale test

The basic material parameters employed by the teams are listed and compared in Table 14. Specific model parameters that need to be calibrated (or that are considered known) are reported in following sections.

Table 14. Basic parameters used by the teams (* indicates values beyond specified parameters)

	BGR/UFZ	LBNL	CIMNE-UPC/Andra
Elastic modulus (MPa)	Heterogeneous*	307	307
Poisson's ratio (-)	0.4	0.4	0.4
Porosity (-)	0.43*	0.44	0.4327 (initial porosity)
Biot's coefficient (-)	0.9	1	0.5
Intrinsic permeability of water (m²)	3.0×10^{-20} *	3.4×10^{-21}	Heterogeneous*

A.6.1.1 Parameters employed by BGR/UFZ

Table 15. Calibrated parameters employed by BGR/UFZ

Parameter	Symbol	Units	Calibrated value	Sensitivity analysis		Effect with respect to the global response
				Minimum value	Maximum value	
Plastic strain multiplier	b_1	-	4000	1000	4000	Impacts the intrinsic permeability

Parameter	Symbol	Units	Calibrated value	Sensitivity analysis		Effect with respect to the global response
				Minimum value	Maximum value	
Volumetric strain multiplier	b_3	-	250	50	250	Impacts the intrinsic permeability
Intrinsic permeability	k_{in}	m²	7.0 x 10⁻²¹	3.0 x 10⁻²¹	6.0 x 10⁻²⁰	Impacts the breakthrough time and the total flow
Mean of the Young's modulus distribution	$\bar{E}$	Pa	3.5 x 10⁹	4.5 x 10⁸	3.5 x 10⁹	Impacts the breakthrough time
Minimum value of the Young's modulus distribution	E_{min}	Pa	5.0 x 10⁸	-	-	Impacts the breakthrough time

Table 16. Other parameters (assumed known) employed by BGR/UFZ to characterise the bentonite.

Parameter	Symbol	Units	Calibrated value	Taken from
Density of solid grains	ρ_s	kg/m³	1570	Tamayo-Mas et al. (2021)

Friction angle	φ	°	32	-
Dilatancy angle	ψ	°	20	-
Cohesion	c	MPa	3	-
Tortuosity	τ	-	1	-
Apparent gas entry pressure (van Genuchten model)	P_0	MPa	10	Senger et al. (2014)
Measure of the pore size distribution (van Genuchten model)	n	-	1.49	Dai et al. (2008)
Residual degree of saturation (van Genuchten model)	S_{res}	-	0.01	Senger et al. (2014)
Maximum degree of saturation (van Genuchten model)	S_{max}	-	0.99	Senger et al. (2014)

A.6.1.2 Parameters employed by LBNL

Table 17. Calibrated parameters employed by LBNL

Parameter	Symbol	Units	Calibrated value	Sensitivity analysis		Effect with respect to the global response
				Minimum value	Maximum value	
Swelling coefficient	β_{sw}	-	0.015	0.01	0.03	Impacts the total stress level
Max aperture for stress-permeability	b_{h0}	m	4.9×10^{-6}	1.0×10^{-7}	1.0×10^{-5}	Impacts gas flow rate after break through
Reference stress normal to the fracture	$\sigma_{n,\,ref}$	Pa	0.1	0.05	1.0	Impacts gas flow rate after break through
Residual saturation of gas (Corey model)	S_{gr}	-	0.13	0.05	0.2	Impacts gas entry (pressure)
Multiplying factor for the enhanced gas permeability (Corey model)	m_g	-	375	100	1000	Impacts gas flow rate

Table 18. Other parameters (assumed fixed) employed by LBNL

Parameter	Symbol	Units	Calibrated value	Taken from
Apparent gas entry pressure (van Genuchten model)	P_0	MPa	18	Senger and Marschall (2008)
Shape factor (van Genuchten model)	λ	-	0.45	Senger and Marschall (2008)
Residual liquid saturation (van Genuchten model)	S_{lr}	-	0.01	Senger and Marschall (2008)

A.6.1.3 Parameters employed by CIMNE-UPC/Andra

Table 19. Other parameters (assumed fixed) employed by CIMNE-UPC/Andra.

Parameter	Symbol	Units	Calibrated value	Taken from
Homogeneous part (same parameter value for the entire sample modelled)				
Dilatancy angle	ψ	°	24	Tamayo-Mas et al. (2021)
Tortuosity for dissolved gas (Fick's law)	τ	-	0.5	

Parameter	Symbol	Units	Calibrated value	Taken from
Transverse dispersion coefficient (Fick's law)	D_T	-	0.001	
Longitudinal dispersion coefficient (Fick's law)	D_L	-	0.01	
Power for liquid state for both matrix and fractures (Relative permeability)	$n_{liquid}^{matrix/fractures}$	-	3	
Maximum liquid saturation (Relative permeability)	S_{liquid}^{max}	-	1	
Minimum liquid saturation (Relative permeability)	S_{liquid}^{min}	-	0	
Power for gas state for matrix (Relative permeability)	n_{gas}^{matrix}	-	2	
Power for gas state for fractures (Relative permeability)	$n_{gas}^{fractures}$	-	1	
Maximum gas saturation (Relative permeability)	S_{gas}^{max}	-	0.3	
Minimum gas saturation (Relative permeability)	S_{gas}^{min}	-	0	
Shape function (van Genuchten model	λ_{VG}	-	0.45	
Initial porosity	ϕ_0	-	0.44	
Dry density	ρ_{dry}	kg/m^3	1512	

Parameter	Symbol	Units	Calibrated value	Taken from
Molar mass of Helium	M	kg/mol	0.004	
Henry's constant	H	MPa	10000	
Heterogeneous part (three different sample zones randomly distributed). M1 (2/3) - M2 (1/6) - M3 (1/6), see Figure 26				
Initial capillary pressure (van Genuchten model)	P_0	MPa	M1: 48.6 M2: 22.5 M3: 10.8	Tamayo-Mas et al. (2021)
Finite air entry value	P_{00}	MPa	M1: 5.4 M2: 2.5 M3: 1.2	
Reference permeability (matrix intrinsic permeability)	k_0	m^2	M1: 1.0 x 10-21 M2: 1.0 x 10-20 M3: 1.0 x 10-19	
Internal associated width for each fracture	a	m	M1: 5.0 x 10-6 M2: 5.0 x 10-5 M3: 5.0 x 10-4	
Initial aperture of the fractures	b_0	m	M1: 1.5 x 10-9 M2: 5.0 x 10-9 M3: 9.5 x 10-9	
Maximum aperture of the fractures	b_{max}	m	M1: 1.5 x 10-7 M2: 3.5 x 10-7 M3: 7.5 x 10-7	
Initial strain	ε_0	%	M1: 0.05 M2: 0.03 M3: 0.01	

A.6.2   Field-scale test

Basic parameters used for the bentonite blocks are the same as the ones used in the modelling of the laboratory-scale experiment. Main differences are thus in parameters used to describe the interfaces.

A.6.2.1 Parameters employed by BGR/UFZ

Table 20. Parameters employed by BGR/UFZ

Parameter	Symbol [units]	Pre-compacted bentonite		Swelled bentonite	
		Value	Reference	Value	Reference
Cohesive strength	C [MPa]	0.05	(Börgesson et al. 1995)	0.05	-
Dry density	P_s [kg/m³]	1670	(Cuss et al. 2010)	1503	-
Friction angle	Φ [°]	10	(Börgesson et al. 1995)	10	-
Initial saturation	S_0 [-]	0.92	(Cuss et al. 2010)	0.92	(Cuss et al. 2010)
Initial void ratio	e_0 [-]	0.66	(Cuss et al. 2010)	0.8	-
Intrinsic permeability	k_{int} [m²]	3.4×10^{-21}	(Tamayo-Mas et al. 2021)	3.4×10^{-21}	(Tamayo-Mas et al. 2021)
Maximum swelling pressure	$\sigma_{sw,max}$ [MPa]	6.2	(Seiphoori 2015)	6.2	(Seiphoori 2015)
Mean gas entry	$\bar{p}_{entry}$ [MPa]	10.6	(Seiphoori 2015)	4.8	(Seiphoori 2015)
Mean Young's modulus	$\bar{E}$ [MPa]	307	(Tamayo-Mas et al. 2021)	276	-
Poisson ratio	v [-]	0.4	(Tamayo-Mas et al. 2021)	0.4	(Tamayo-Mas et al. 2021)

Parameter	Symbol [units]	Pre-compacted bentonite		Swelled bentonite	
		Value	Reference	Value	Reference
Porosity	ϕ [-]	0.44	(Tamayo-Mas et al. 2021)	0.44	(Tamayo-Mas et al. 2021)
Tensile strength	f_t [MPa]	1	-	0.001	-
Strain dependent permeability parameter	b_1 [-]	10000	-	10000	-
	b_2 [-]	250	-	250	-
	b_3 [-]	250	-	250	-
vG parameter	m [-]	0.5	(Villar 2005)	0.5	(Villar 2005)
vG parameter	n [-]	2.0	(Villar 2005)	2.0	(Villar 2005)

A.6.2.2 Parameters employed by LBNL

Table 21. Parameters employed by LBNL/UFZ

Parameter	Symbol [units]	Value Bentonite blocks	Value Interfaces	Reference
Elastic modulus	E [MPa]	307		(Tamayo-Mas et al. 2021)
Poisson's ratio	ν [-]	0.4		(Tamayo-Mas et al. 2021)
Porosity	ϕ [-]	0.44		(Tamayo-Mas et al. 2021)
Biot's coefficient	α [-]	1		Fixed
Swelling coefficient	β_{sw} [-]	0.015		Calibrated
Max aperture for stress-k	b_{ho} [m]	4.9×10^{-6}		Calibrated
Reference stress for stress-k	$\sigma_{n,ref}$ [MPa]	0.1		Calibrated
Intrinsic permeability	[m^2]	3.4×10^{-21}	3.4×10^{-20}	
Capillary scaling (capillary pressure)	P_0 [MPa]	18		Senger and Marschall (2008)
Shape factor (capillary pressure)	λ [-]	0.45		Senger and Marschall (2008)
Residual liquid saturation (capillary pressure)	S_{lr} [-]	0.01		Senger and Marschall (2008)
Residual liquid saturation (relative permeability)	S_{lr} [-]	0.1		Fixed
Residual gas saturation Srg (relative permeability)	S_{rg} [-]	0.13	0.05	Calibrated

Parameter	Symbol [units]	Value		Reference
		Bentonite blocks	**Interfaces**	
Gas permeability enhancement (relative permeability)	m_g [-]	3750		Calibrated

A.6.2.3 Parameters employed by CIMNE-UPC/Andra

Parameter	Symbol [units]	Value									Reference
		Rock	Bentonite cylinders and rings	Pellets	Gap	Canister	Injection filters	Internal pipework	Coping (concrete plug)	Coping (steel lid)	
Elastic modulus	E [MPa]	69000	307			210000			307		
Poisson's ratio	ν [-]	0.25	0.4			0.3			0.4		
Initial porosity	ϕ_0 [-]	0.003	0.366	0.706	variable	0.001	-	0.0001	0.145	0.001	
Reference porosity	ϕ [-]	-	-	0.425	0.3976	0.425	variable	-	-	0.425	
Biot's coefficient	α [-]	0.0	0.5			0.5			0.5		
Dilatancy angle	Ψ [°]	-	24			-			24		

Parameter	Symbol [units]	Value									Reference
		Rock	Bentonite cylinders and rings	Pellets	Gap	Canister	Injection filters	Internal pipework	Coping (concrete plug)	Coping (steel lid)	
Intrinsic reference permeability	k_0 [m^2]	$1x10^{-18}$	$1x10^{-19}$ $1x10^{-20}$ $1x10^{-21}$ (Heterogeneity) In the horizontal and vertical interfaces: $1x10^{-17}, 1x10^{-18}, 1x10^{-19}, 1x10^{-20}$			$1x10^{-27}$	$1x10^{-20}$	$1x10^{-27}$	$1x10^{-18}$	$1x10^{-19}$	
Capillary scaling (capillary pressure)	P_0 [MPa]	0.5	20 In the horizontal and vertical interfaces: 1.95, 4.2, 9.2, 20	0.5	20	5.0	0.1	5.0	1.5	5	
Shape factor (capillary pressure)	Λ [-]	0.3	0.3			0.36	0.25	0.36	0.3		

Parameter	Symbol [units]	Value									Reference
		Rock	Bentonite cylinders and rings	Pellets	Gap	Canister	Injection filters	Internal pipework	Coping (concrete plug)	Coping (steel lid)	
Liquid (relative + intrinsic permeability)	n_l [-]	3	3			3			3		
Max./min. liquid saturation (relative permeability)	S_l [-]	1.0/0.0	1.0/0.0			1.0/0.0	0.5/0.0	-	1.0/0.0		
Gas (relative permeability)	n_g [-]	3	2			2			2		
Max./min. gas saturation (relative permeability)	S_g [-]	0.3/0.0	0.3/0.0			0.3/0.0			1.0/0.0		

Parameter	Symbol [units]	Value									Reference
		Rock	Bentonite cylinders and rings	Pellets	Gap	Canister	Injection filters	Internal pipework	Coping (concrete plug)	Coping (steel lid)	
Max./min. gas saturation (intrinsic permeability)	S_g [-]	1.0/0.0	1.0/0.0			0.3/0.0					
Tortuosity for dissolved gas (Fick's law)		0.5	0.5			-			-		
Dispersivity for dissolved gas Longitudinal (Fick's law)		0.5	0.5			0.5	1..0	-	0.5		
Dispersivity for dissolved gas Transversal (Fick's law)		0.05	0.05			0.05	0.1	-	0.05		

Parameter	Symbol [units]	Value									Reference
		Rock	Bentonite cylinders and rings	Pellets	Gap	Canister	Injection filters	Internal pipework	Coping (concrete plug)	Coping (steel lid)	
Saturated unit weight	γ_{sat} [kN/m³]	25.0	20.2 (cyl.) 20.7 (ring)	19.0	variable	75	25	75	2580	3186	
Specific heat	c_α [J·kg⁻¹·K⁻¹]	750	1091		variable	460	700	1091	550	1091	
Molar mass of helium	M [kg/mol]		0.004								
Henry's constant	H [MPa]		1000								